Electron and Ion Beam Imaging of Human Bone Structure Across the Nano- and Mesoscale

By DAKOTA M. BINKLEY, B.Sc. (Hons)

A Thesis Submitted to the School of Graduate Studies in Partial Fulfilment of the Requirements for the Degree of Master of Applied Science

MASTER OF APPLIED SCIENCE (2019), Materials Science and Engineering

McMaster University, Hamilton, Ontario, Canada

TITLE: Electron and Ion Beam Imaging of Human Bone Across the Nano- and Mesoscale

AUTHOR: Dakota M. Binkley, B. Sc. (Hons) (McMaster University, Hamilton Ontario)

SUPERVISOR: Dr. Kathryn Grandfield

NUMBER OF PAGES: xviii, 73

Lay Abstract

Bone tissue has a unique structure that perplexes both biologists and materials scientists. The hierarchical structure of bone has garnered the interest of materials scientists since the body's skeletal strength and toughness are governed by the nanoscale (millionth of centimetres) to macroscale (centimeters) organization of bone. In this work, the intricate organization of bone is investigated using advanced electron and ion beam microscopy techniques, which achieve high-resolution imaging of bone structure. Firstly, this work developed a sample preparation workflow to correlate electron and X-ray imaging of the same bone tissue. Secondly, this work was the first to apply serial-sectioning plasma focused ion beam tomography to human bone tissue to investigate its structure at high resolution across micron-sized volumes. Here, previously unexplored methodologies to image bone are demonstrated with the hopes of applying such techniques to investigate healthy and pathological bone tissue in the future.

Abstract

Human bone tissue has an inherent hierarchical structure, which is integral to its material properties. It is primarily composed of a collagen fiber matrix that is mineralized with hydroxyapatite. A comprehensive understanding of bone and the linkages between structural and cellular organization is imperative to developing fundamental knowledge that can be applied to better our understanding of bone disease manifestations and its interaction with implant devices. Herein, this thesis investigated non-traditional methods for evaluating bone structure across the nano- and meso-length scales.

Firstly, due to the inhomogeneous organization of collagen fibrils and mineral platelets of bone ultrastructure, a suitable methodology for the investigation of both phases needed to be generated. In this work, focused ion beam (FIB) microscopy was employed to create site-specific scanning transmission electron microscopy (STEM) lift-outs of human osteonal bone that could be visualized with correlatively with STEM and small angle X-ray scattering (SAXS). Samples were successfully characterized using both techniques, and minimal visual damage was induced during data acquisition. This work is the first to demonstrate the potential for bone to be investigated correlatively using both STEM and SAXS.

Secondly, this work is the first to employ a dual-beam plasma FIB (PFIB) equipped with a scanning electron microscope (SEM), to investigate bone tissue across the mesoscale. This equipment enables large volume three-dimensional (3D) imaging at nanoscale resolution across larger mesoscale volumes. This thesis aimed to reduce ion beam-based artifacts, which presents as curtain-like features by adjusting the composition of protective capping layers. Subsequently, large volume tomograms of bone tissue were acquired, demonstrating the effectiveness of the PFIB to reveal mesoscale features including the cellular network of bone tissue.

Overall, this thesis has developed methods that allow for the application of advanced microscopy techniques to enhance the understanding of bone tissue across the nanoscale and mesoscale.

Acknowledgements

current members: Ivan Strakhov, Andrew D'Elia, and Griffin McLean for their continual support.

My Master's experience would not have been nearly as influential without the support and friendships made in JHE A406, or in the unofficial MSE Run Club. Although geographical distance has come between us, I would not have made it this far in my education without: Lucia Krivankova-Smal, Meena Al Saigh, Supryia Singh, Eva Clark-Lepard, and Miriam Krzyzewska. Finally, I would like to thank the student members of LiPhy who made my international exchange experience blissful. Special thanks to Vanni Petrolli, Luica Stein-Montalvo, and Saranath Seshadri for welcoming me with open arms and making my stay in Grenoble blissful.

Table of Contents

List of Figures

List of Tables

List of Abbreviations

BSE: back scattered electron

C: Carbon

Ca: Calcium

CBS: circular backscatter detector

CPD: critical point drying

EELS: electron energy loss spectroscopy

ESRF: European Synchrotron Radiation Facility

ETD: Everhart-Thornley detector

FEG: field emission gun

FIB: focused ion beam

Ga: Gallium

GIS: gas injection system

HA: hydroxyapatite

HAADF: high-angle annular dark-field

HIREB: Hamilton Integrated Ethics Research Board

ICP: inductively coupled plasma

LMIS: liquid metal ion source

Nano-CT: nano-computer tomography

O: osmium tetroxide

P: Phosphorous

PED: precession electron diffraction

PFIB: Plasma Focused Ion Beam

Pt: Platinum

ROI: region of interest

SAXS: small angle X-ray scattering

SEM: scanning electron microscopy

STEM: scanning transmission electron microscopy

T: thiocarbohydrazide

TEM: transmission electron microscopy

TLD: through lens detector

μ-CT: micro-computer tomography

W: Tungsten

Wt%: weight percent

Xe: Xenon

Z: atomic number

2D: two-dimensional

3D: three-dimensional

Declaration of Academic Achievement

I hereby declare to be the sole author of this document. The research work presented in this thesis was in the most part completed by myself, with the contribution of people and institutions listed below.

- Bone tissue staining assistance was provided by Xiaoyue Wang
- Scanning electron microscopy and focused ion beam microscopy coating was completed by Andy Duft, Chris Bucher, and Jhoynner Martinez at the Canadian Center for Electron Microscopy (Hamilton, ON, Canada)
- Focused ion beam lift-outs were prepared using a NVision 40 by Travis Casagrande at the Canadian Center for Electron Microscopy (Hamilton, ON, Canada)
- Scanning transmission electron microscopy was partially completed by both Carmen Andrei and Natalie Hamada at the Canadian Center for Electron Microscopy (Hamilton, ON, Canada)
- Small angle X-ray scatting was completed by Aurélien Gourrier and his research team at the European Synchrotron Radiation Facility
- Plasma focused ion beam data acquisition completed by Hui Yuan
- Data segmentation was aided by Natalie Reznikov (ORS, Montreal, Quebec)

In addition to the work and publications presented in this thesis, I have also contributed to the following published works and industry reports listed below:

Micheletti C., Deering, J., Lee B.E.J, **Binkley D.M.,** Coulson, S., Hussanain, A., Zurob H., and Gradnfield K. (2019) "Electrochemical Anodization of 3D-Printed Titanium Alloys for Bone Implants with Dual-Scale Topography: Ti-5Al-5Mo-5V-3Cr and Ti-6Al-4V" *Additive Manufacturing*. Submission No. ADDMA_2019_662.

Binkley, D.M., Lee B.E.J, Saem, S., Moran-Mirabal, J., and Grandfield K. (2019) "Fabrication of polycaprolactone electrospun nanofibers doped with silver nanoparticles formed by air plasma treatment" *Nanotechnology*. DOI: https://doi.org/10.1088/1361-6528/ab0444

Binkley, D.M., Liu, Z-M., Davies, J.E. and Grandfield K. (2018) "Electron microscopy report of bone-implant interfaces" Prepared for: Zimmer BioMet.

1. Introduction

1.1 Research motivation

Bone is a naturally occurring biological material comprised of an organic collagen phase and a calcium (Ca) and phosphorous (P) rich mineral phase [1]. The inherent hierarchical structure of bone spans from the atomic to millimeter scale and provides it with unique functional properties [2]. It is imperative to gain a better understanding of the complex interplay between the organic and inorganic components of bone, as well as their higher order organization into functional structures, as it influences many of its essential materials properties [3]. A more advanced understanding of the organization of bone also remains necessary for the design of improved bone implants for both dental and orthopedic applications. Moreover, the structure of healthy bone tissue must be evaluated to gain a better understanding of structural differences between healthy and diseased bone. Therefore, the research presented in this thesis addresses the characterization of healthy bone tissue with sophisticated characterization tools to aid in the comprehensive understanding of the complexity of bone tissue.

Bone structure has been investigated across its length scales through the use of advanced microscopy techniques [4], [5], however linking its structural and biological entities across length scales that span 10s of microns, remains a challenge. This apparent challenge is in part due to the lack and complexity of correlative microscopy approaches [6], and the natural biological variations in bone tissue. In addition, inherent instrument constraints dictate sample shape and size, making some samples suitable for one approach and not suitable for another. Finally, bone is a highly organic material, which can be easily damaged by some of the more sophisticated probes, such as electron or X-ray beams [7], [8]. Correlative imaging of the same sample using multiple techniques therefore becomes difficult.

The mesoscale (spanning 100 nm to 100 μm) organization of bone provides linkages between structural and biological units, connecting nano- and microscale information, which are imperative to understanding mineralization and other biological processes [9]. Imaging the entire mesoscale organization of bone in three-dimensions (3D) remains a challenge in part because of current instrumentation limitations with respect to volume size and resolution. Micro-computed tomography (μ-CT) can image larger volumes (50 μm^3) at a lower resolution, making the intricacies of the cellular network, mineral layers, and collagen components

unresolvable simultaneously [10]. Meanwhile, more advanced techniques such as electron tomography with TEM yield small volumes ($1\mu m^3$) with nanoscale resolution [11]. Thus, high-resolution information remains restricted to small volumes meaning that the meso- or microscale organization of bone cannot be definitively resolved. To better understand the unique hierarchical structure of bone, this thesis will focus on the development of a correlative nanoscale characterization strategy and development of a mesoscale imaging approach.

1.2 Research objectives

The main objective of this thesis is to develop strategies to visualize the unique hierarchical structure of bone from the nano- to mesoscale. This thesis is divided into two main projects with the following research objectives:

Nanoscale Bone Imaging:

Part one of this thesis reports the development of a correlative workflow that allowed for site-specific analysis of bone in both real and reciprocal space using transmission electron microscopy (TEM) and small angle X-ray scattering (SAXS). This platform also qualitatively assesses radiation damage from SAXS. The specific objectives were:

- To create a correlative workflow to allow for the characterization of structurally similar bone tissue by TEM and SAXS using site-specific sample preparation techniques, such as focused ion beam (FIB) microscopy.
- To qualitatively assess SAXS beam damage of bone material using TEM.

Mesoscale Bone Imaging:

Part two of this thesis aims to apply plasma focused ion beam (PFIB) tomography as a method to image the mesoscale structure of bone for the first time. In order to advance this area of imaging, preliminary development of the process were the objectives of this thesis, in particular:

- To link the structural and biological aspects of bone from nano- to mesoscale by investigating sample preparation methods and minimizing artifacts during PFIB tomography acquisitions.

2. Background

2.1 Bone tissue

Bone is a naturally occurring mineralized tissue that makes the skeletal framework for all vertebrates and provides the body with strength, toughness, and stability. From a biological perspective, bone houses reservoirs of both Ca and P, which are required for many biochemical reactions within the body [12]. In addition, bone stores marrow, which dictates the adaptive immune response and governs blood cell production [12]. Bone is commonly researched from a multitude of perspectives, including physiology and health [13], [14], and from non-traditional views such as materials science due to its unique hierarchical structure [2]. The studies presented in this thesis focus on investigating bone structure from a materials science perspective.

2.1.1.1 Bone composition

Bone is a hierarchical composite material that is widely accepted to consist of a mineral phase (60 wt%), an organic phase (30 wt%) and water (10 wt%) [15]. The mineral phase of bone, hydroxyapatite (HA; $Ca_{10}(PO_4,CO_3)_6(OH)_2$), exists as elongated plates, with dimensions of 2 − 6 nm thick, 25 − 50 nm wide, and 50 − 100 nm in length [3]. The organic phase consists of primarily Type I collagen and fewer non-collagenous proteins. The collagen assembles into fibers which are 1.5 nm in diameter and 300 nm long [16], these make up larger fibrils that are approximately 50 nm in diameter [17].

2.1.1.2 Bone as a hierarchical structure

Bone tissue has garnered the interest of materials scientists due to its unique heterogeneity across all length scales [1], [2], and has been divided into nine levels of hierarchy (Figure 2.1). On the macro-scale, bone can be divided into two main types: cortical (compact) and trabecular (cancellous) bone. Cortical bone makes up 80% of the bone found in the skeleton, meanwhile, the other 20% is a more porous bone structure referred to as trabecular bone [12]. Both cortical and trabecular bone are comprised of smaller units, or bone structural units (BSUs), termed osteons and trabeculae, respectively. Osteons are concentric features with lamellar layers that twist around the structure [18], and trabeculae are composed of packets of lamellae with various orientations [19]. The lamellae in these structural units are made of mineralized collagen fibrils. At the nanoscale, collagen triple helixes make up collagen fibrils and assemble into a

periodic structure, giving rise to a traditional collagen banding pattern in TEM [20].

FIB tomography has revealed heterogeneity in nanoscale collagen organization [9], [21]. The collagen fibrils are organized either rigidly, where the traditional collagen banding patterns can be observed, or in a disordered phase where this pattern is not apparent [9]. These phases alternate throughout the bone structure, and the bone cellular network resides within these disordered collagen organizations [9]. The periodic nanostructure of bone consists of collagen fibrils with 40 nm gap zones and 27 nm overlap zones, which gives rise to the characteristic 67 nm banding pattern observed in TEM [20]. This network is mineralized with HA nanocrystals both within the gap zone (intrafibrillar mineralization) and, more recently, confirmed to also exist in a large proportion along the exterior of the fibrils (interfibrillar or extrafibrillar mineralization) [20], sometimes referred to as mineral lamellae (ML) [15], [22]. Thus, the exact ultrastructural organization of bone mineral remains controversial within the scientific community.
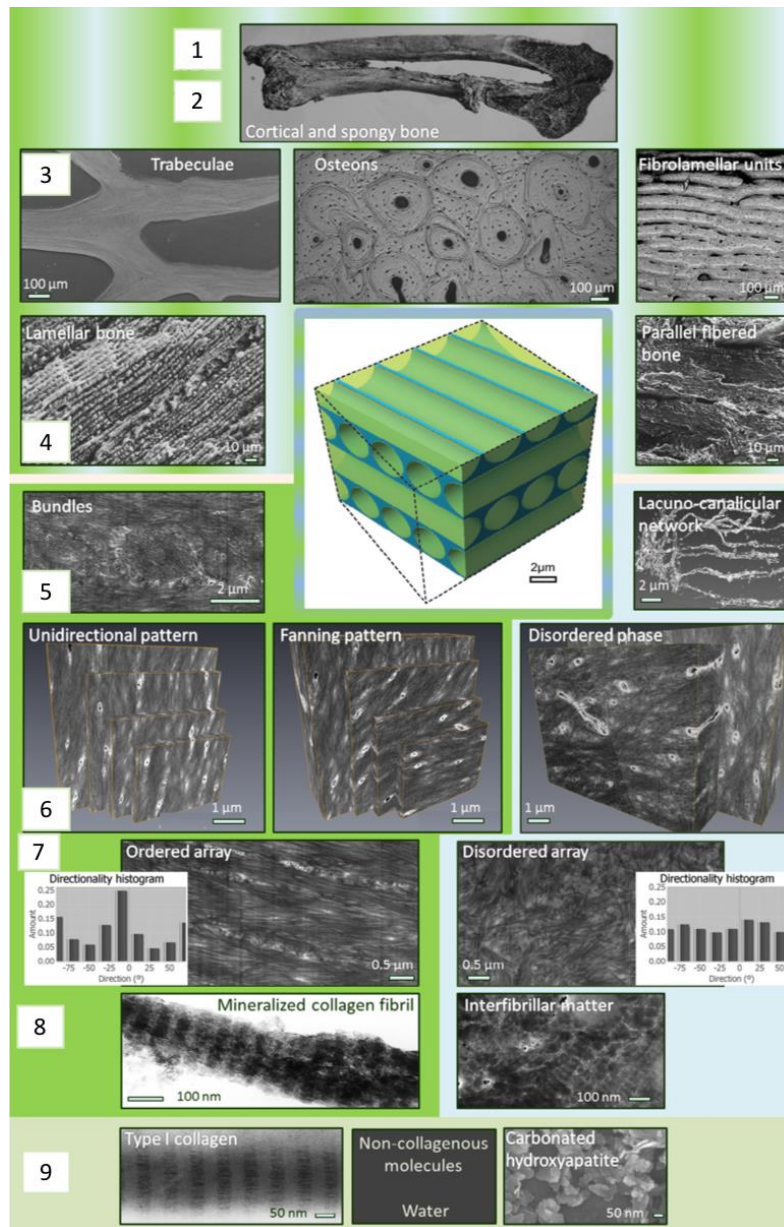
Figure 2.1. The nine hierarchical levels of bone organization. The schematic represents the organization of ordered and discorded bone in 3D, where the osteons and trabecular features are highlighted in row three. On the subsequent level of hierarchy, collagen fibrils are organized as either an disordered or ordered phase, seen in rows five and size. Finally, the nanoscale organization of bone, including the traditional banding pattern of bone is exemplified in row 8. Adapted from [4] with kind permission from Elsevier.

2.1.1.3   Osteonal lamellae

From the nanoscale to the mesoscale, most structural elements of bone are wrapped or twisted around one another in a rope-like fashion [4]. At the micron scale, this helps maintain structural integrity and allows bone to withstand crack propagation after fracture [23]. Osteons are composed of concentric structures, known as osteonal lamellae. The collagen fibers that make

up these lamellae are suggested to be oriented in one of two ways: (1) such that they twist around the osteon in a circular fashion, or (2) such that the collagen in each layer is orthogonal to the successive layer [18]. More sophisticated theories were derived, which suggested that osteonal lamellae are divided into five different regions that all have collagen fibrils arranged with a consecutive 30° degree rotation [24], [25]. This debate of collagen orientation in osteonal lamellae and other mineralized tissues remains ongoing, partially due to the inability to visualize fine details such as collagen fibrils over microscale features such as osteons [26].

Scanning TEM (STEM) imaging has demonstrated a change of collagen fibrils across osteonal lamellae from parallel to orthogonal (Figure 2.2) [27]. SAXS experiments have also demonstrated that the nano-crystalline organization in these lamellar layers plays a key role in the strength of osteons [28].
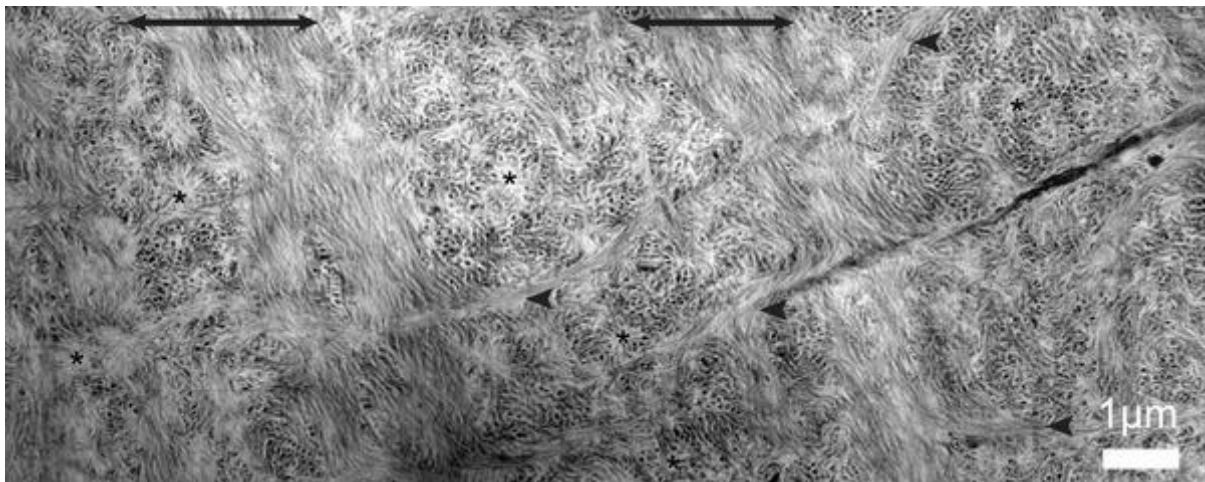
Figure 2.2. STEM imaging of multiple osteonal layers, where layers alternate between parallel and orthogonal orientation. Layers with parallel organization are below the double headed arrows, and fibril-like structures that seem to connect the osteonal layers are denoted by single headed arrows. Figure reprinted from [27] with kind permission from Springer Nature.

2.1.2 Bone remodeling

Bone is dynamic, as it continuously remodels throughout life allowing for both growth and wound healing [12]. The cyclic biological process of remodeling is governed by coordinated cellular events, which consist of the removal of damaged bone material followed by the deposition and mineralization of new bone tissue (see Figure 2.3). Remodeling is responsible for maintaining the integrity of the mineralized matrix and the ionic reservoirs throughout one's lifetime.

Bone has three basic cells that are responsible for bone remodeling: osteoclasts, osteoblasts, and osteocytes [12], [14]. During the cyclic remodeling process, the signaling sequence initiates when damaged tissue is detected by resident osteocyte cells, trapped within the bone mineral matrix, in spaces referred to as the osteocyte lacunae [29]. Both osteoclasts and osteoblasts are recruited to the site. Osteoclasts resorb bone by digesting the mineral component of the bone tissue into their cell membrane and degrading it under acidic conditions [12], [14]. To replace the resorbed bone mineral matrix, osteoblasts attach to the bone surface and initiate the coupling of bone absorption and formation. Bone formation initiates once pre-osteoblasts are recruited to the resorbed area, differentiate, and secrete the new bone matrix [14]. After secretion, osteoblasts become embedded in the bone matrix and terminally differentiate into osteocytes.
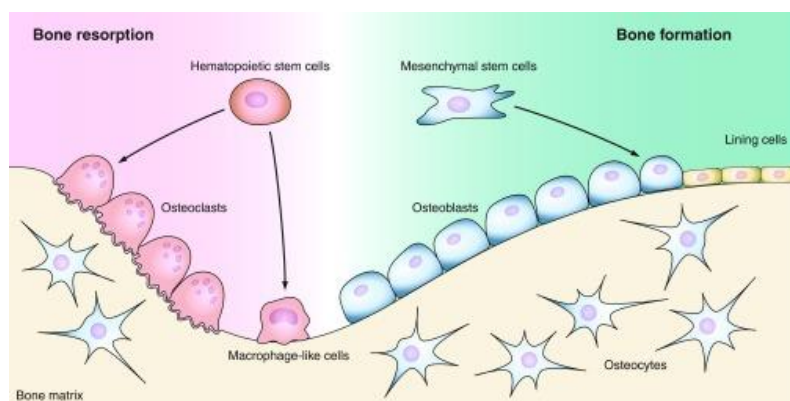
Figure 2.3. A schematic of the cellular bone remodeling process, reprinted from [30] with kind permissions from The American Physiological Society.

2.2 Microscopy techniques for imaging bone

Materials scientists have attempted to characterize bone structure using advanced microscopical techniques, and sophisticated correlative and multi-scale imaging platforms [31], however scientific questions regarding mineralization, cellular connectivity, and other structural arrangements still remain. A detailed review of imaging techniques for bone is reported elsewhere [5] and reviewed partially by our publication in ACS Biomaterials Science & Engineering [32] (Appendix I of this thesis). This thesis employed scanning transmission electron microscopy (STEM) and plasma focused ion beam (PFIB) scanning electron microscopy (SEM) serial sectioning techniques to characterize these structural aspects of bone tissue.

7

2.2.1 TEM

TEM has been employed in the biological community to investigate organelle structure [33] and to evaluate the nanoscale organization of both soft and mineralized tissues [5], [34]. Most cellular studies have used cryogenic-TEM, where the sample is maintained at cryogenic conditions prior to and during the imaging process, allowing for hydrated state-visualization [35]. Meanwhile, the investigation of mineralized tissues, including bone, have relied primarily on traditional TEM imaging modalities [11]. Herein, TEM visualization techniques for mineralized tissues will be discussed.

2.2.1.1 Imaging modes

TEM and STEM have been employed to image the ultrastructure of bone [27], [36], [37], and in the investigation of other biological materials [38]. In TEM, the sample is imaged by a high voltage parallel beam and inelastically scattered electrons are collected after they pass through the specimen [39]; whereas in STEM mode, the sample is probed by a focused beam that rasters across the surface [39], and inelastically scattered electrons at high angles are detected by a high-angle annular dark-field (HAADF) detector for biological materials [11] (Figure 2.4). HAADF STEM imaging provides superior contrast in biologicals, as the HAADF detector suppresses diffraction contrast while enhancing atomic number (Z)-contrast, where elements of heavier Z appear brighter than lower Z elements [39].
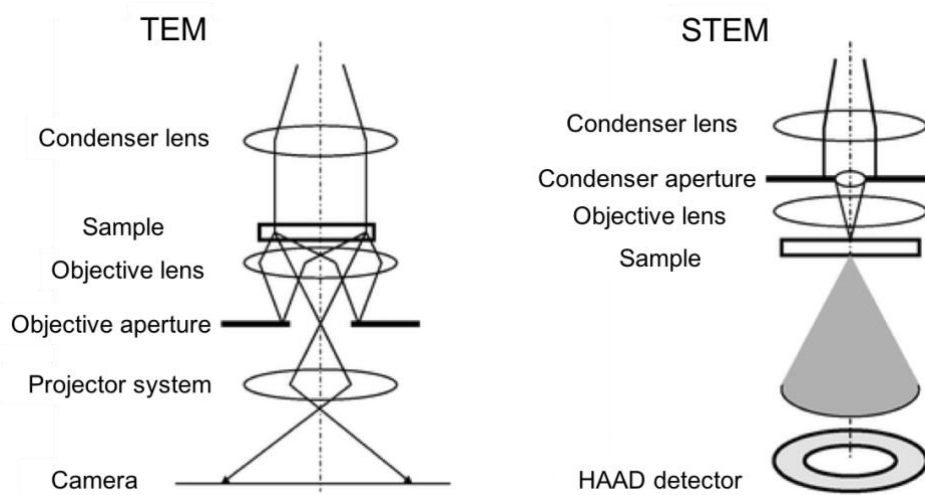
Figure 2.4. Electron beam ray diagrams for both traditional TEM mode and STEM mode. Adapted from [40] with kind permission from the Royal Society of Chemistry.

Soft materials are susceptible to beam damage due to their weak atomic bonds, which can be altered or destroyed by the influx of energy. TEM imaging in any mode can induce beam damage to biological samples through two main mechanisms: (1) radiolysis, which is the beam-induced breakage of chemical bonds that can result in structure disruption and ultimately mass loss [41], (2) heating, where the lost energy from inelastically scattered electrons dissipates as heat within the sample causing bond breakage or melting [7] and (3) knock-on damage, where an atom of the sample is sputtered by the electron beam, which is most common in polymeric materials [7], [42]. Beam damage in biological samples is suggested to be reduced in STEM mode, as the beam rasters across the sample, allowing for a smaller area of local heating, and improved heat dissipation. In this thesis, HAADF STEM was employed exclusively for all TEM imaging due to its preferred contrast mechanism, and reduced beam damage.

2.2.1.2   TEM sample preparation

Analyzing mineralized tissues or soft tissues remains challenging due to the organic nature of these materials and their complicated interactions with the electron beam. Preliminary material-specific sample preparation methods have been developed to both increase image contrast and minimize structural damage in electron microscopy (EM; including TEM) and ion beam microscopy investigations. Samples are typically fixed, dehydrated, and either embedded or freeze dried such that the microscope vacuum does not distort the tissue [43]. Additionally, heavy element staining through successive treatments of osmium tetroxide (O) and thiocarbohydrazide (T) (OTOTO) are often employed to increase contrast [44].

Due to inherent instrumentation restraints, TEM samples must be thinned until electron transparency, and thus the overall sample area is relatively small (microns squared) to minimize bending. For mineralized tissues such as bone and teeth, one of three primary TEM preparation methods are typically employed: (1) ultramicrotomy, (2) ion milling, or (3) focused ion beam (FIB) lift-out technique, which is the most favorable TEM preparation method due to its site-specificity and overall sample thickness uniformity [45].

The application of FIB microscopy for TEM sample preparation has also been employed by material scientists due to its ability to target specific regions of interest (ROIs) while maintaining sample integrity and uniform thickness. The dual-beam FIB-SEM is a sophisticated instrument which relies on generating and detecting both ion and electron beam interactions with the sample, in which the sample is concurrently visualized by the electron

beam and milled by the gallium (Ga) ion beam (Figure 2.5) [45]. The most predominant use of this system is for the creation of TEM samples, also referred to as TEM lift-outs. During this process, the sample is visualized using SEM where an ROI is selected, and a gas injection system (GIS) is used to deposit a protective capping layer on the sample surface. The ion beam then mills trenches around the ROI, and a micromanipulator is used to remove the exposed cross-section and place it on a TEM grid, where it is thinned to electron transparency using the ion beam [45]. Critical limitations of the FIB lift-out process include high operation costs and ion implantation, by which ions from the FIB can contaminate the sample surface [46] or result in surface amorphization [47], however, these artifacts are mitigated by the use of low energy ion currents during polishing [48]. All TEM samples in this thesis were prepared using the FIB lift-out techniques due to its site-specificity.
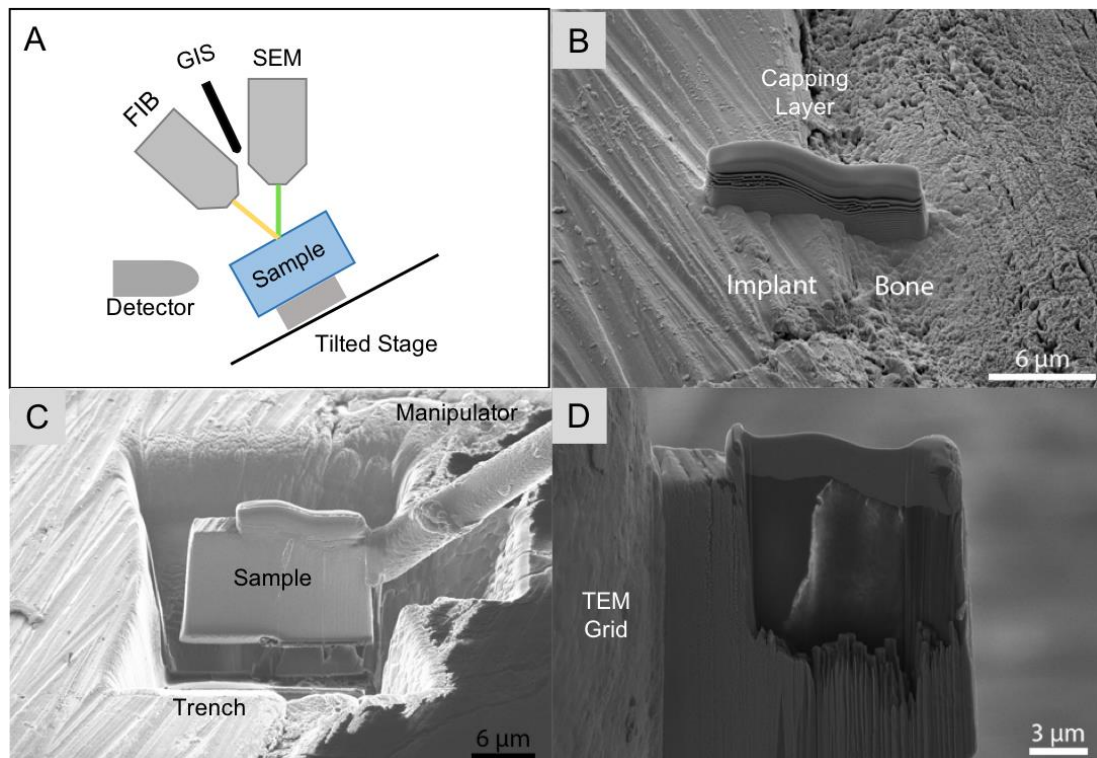
Figure 2.5. The FIB lift-out method. (A) FIB schematic for the preparation of TEM lift-outs, note the sample is tilted such that the FIB beam interacts with it from a 90° angle (B) Deposition of protective capping layer on ROI (C) trench milling exposing the cross-sectional sample and removal via micromanipulator and (D) thinning on TEM grid until electron transparent. Figure B – D were adapted from [49] under the Creative Commons Attributions Licence.

2.2.2 FIB tomography

The conventional FIB-SEM system (described in section 2.2.1.2 above) employs a focused

beam of Ga ions to remove material, which is often applied to prepare TEM lift-outs. Another application of FIB-SEM is FIB-SEM tomography, also known as FIB-serial sectioning, which relies on a destructive line-of-site process to accumulate multiple two-dimensional (2D) images of a sample. The sample surface is repeatedly milled by ions and the cross-section is simultaneously imaged by electron optics (Figure 2.6). After data acquisition, images are post-processed via alignment tools and reconstruction algorithms to produce three dimensional (3D) volumes, referred to as tomograms (Figure 2.6C and D) [50]. Ga sourced FIB-serial sectioning of demineralized bone tissue has been applied to visualize singular osteocyte lacunae [51] and reveal collagen organizations, or motifs, to further our understanding of the rope-like collagen fibrils within bone tissue at the sub-micron scale [9]. However, these studies are limited since Ga FIB-serial sectioning can only yield final 3D reconstructions of approximately 10 μm^3, which is not large enough to fully understand the collagen network orientation with respect to the osteocyte lacunae network.
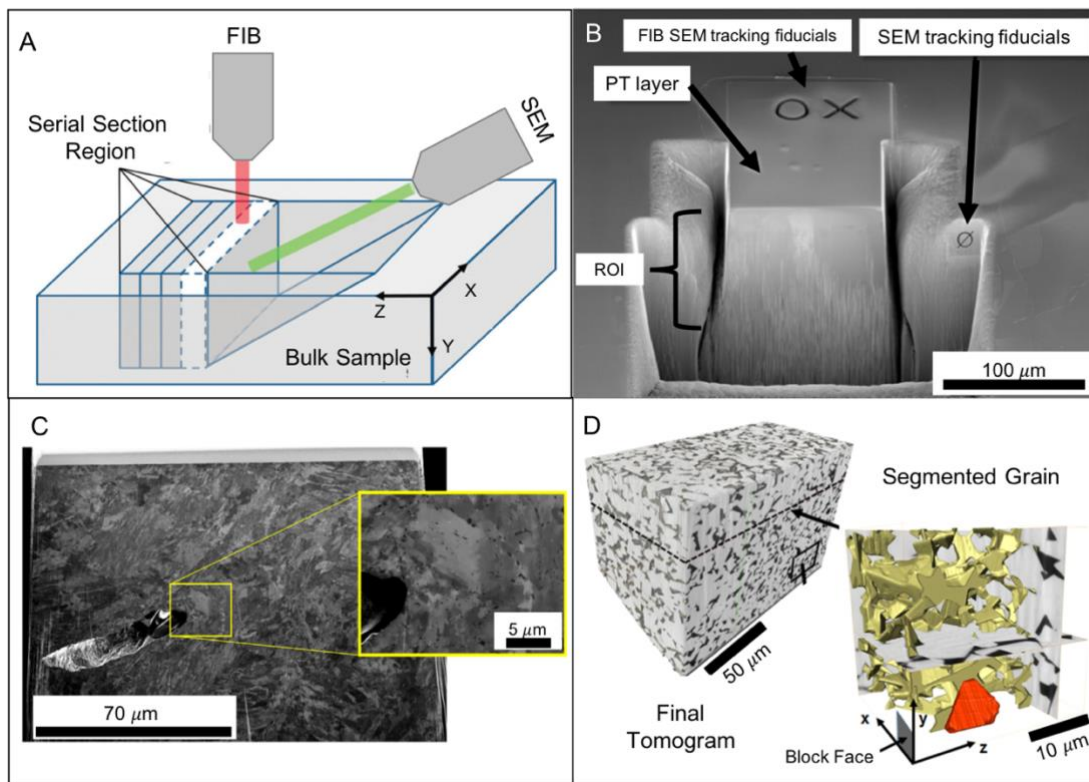
Figure 2.6. The FIB-seral sectioning process. (A) A schematic of the FIB serial sectioning process, where the cross-section is visualized by the SEM beam during simultaneous FIB milling. (B) An SEM image of the milled cross-section of a WC-Co metal, where SEM and FIB fiducials are required for tracking. (C) An example of an SEM image of one slice of the WC-Co, where high resolution features can be seen in the insert. (D) The final 3D tomogram of the collected slices, with a segmented grain feature. Figure A was adapted from [52] with kind permission from the American Chemical Society,

and Figures B and D were adapted from [53] under the Creative Commons Attributions Licence, respectively.

The amount of material that can be milled by the ion beam is primarily dependent on beam current [54], as physical ion size has minimal effect on milling rates [53]. Ga beams are generated by a liquid metal ion source (LMIS), where Xenon (Xe) ion beams are produced by inductively coupled plasma (ICP) sources, which achieve higher beam currents [54]. Serial sectioning using a PFIB equipped with a Xe ion source and SEM is an emerging microscopy technique that has characterized traditional materials (e.g. metal alloys [50]) in 3D over larger microscale volumes, up to 100s of um^3 (Figure 2.7), and is believed to have the potential to image biological materials over similar length scales [53]. The inherent hierarchical structure of bone necessitates investigation across nano- to micron length scales in 3D, such that the overlap between the various hierarchical levels can be revealed. PFIB serial sectioning offers the potential to investigate such interconnectedness of the tissue but has yet to be applied to characterize bone.
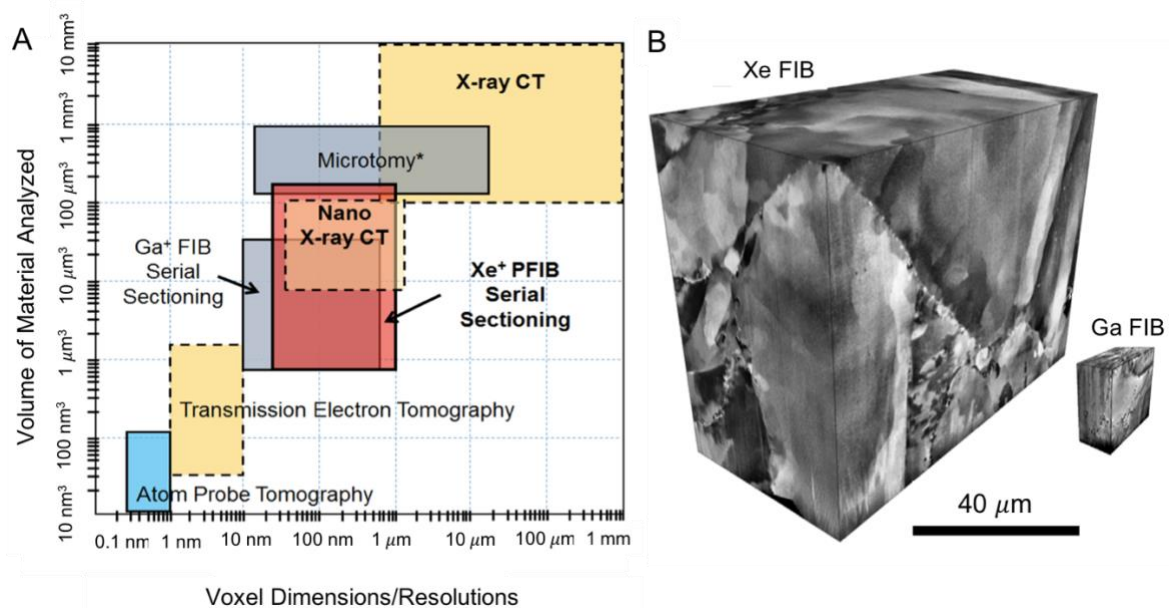
Figure 2.7. (A) A graphical representation of the volume size and voxel resolution of multiple tomography techniques, where the grey box represents Ga FIB serial sectioning and the red represented PFIB serial sectioning. (B) Tomogram volumes achieved by Ga and Xe sourced FIBs. Adapted from [53] under the Creative Commons Attributions Licence.

2.2.2.1 Curtaining

A critical artifact in FIB-SEM tomography is 'curtaining', which is named after the theatre curtain-like appearance left on the milled material, either in cross-section (Figure 2.8), or TEM lift-outs. These artifacts arise from preferential milling and are attributed to surface roughness

in the direction of milling, changes in material composition, or differences in crystalline orientation [55], [56]. Curtaining and other ion beam damage can be reduced with decreased ion currents, however smaller currents equate to longer milling times.
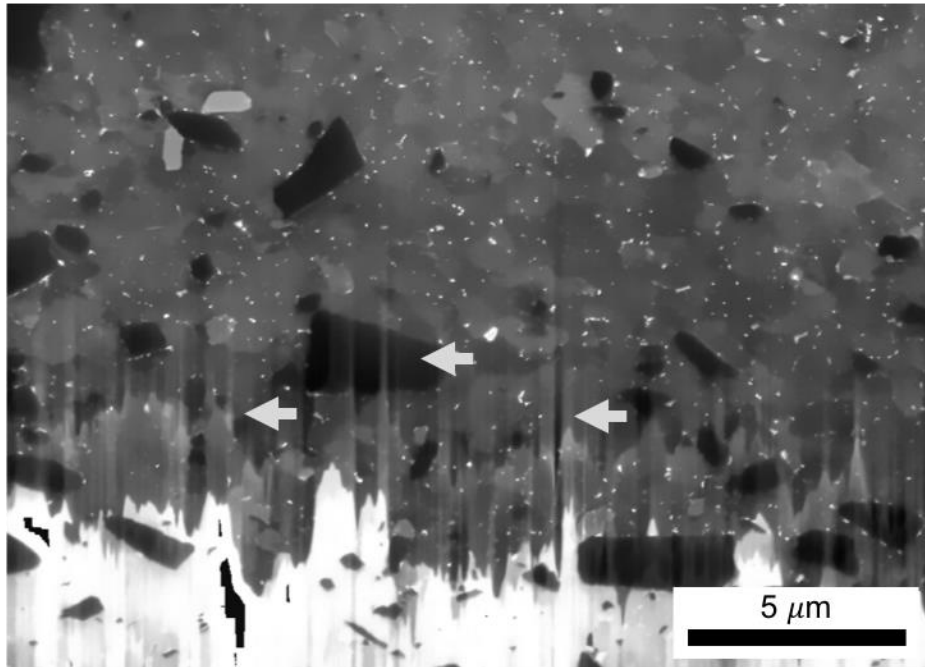
Figure 2.8. An SEM image of a FIB milled cross-section of an aluminum alloy, where arrows point to curtain-like features near the bottom of the image. Adapted from [57] under the Creative Commons Attributions Licence.

Advances in hardware have led to decreases in curtaining during dataset acquisition for most materials. For example, the development of a rocking stage, where the stage of the microscope is tilted a few degrees after each cross-section is milled has shown to effectively reduce the preferential milling in one direction by changing the incident angle of the beam [57]. Curtaining can also be corrected for using various post-processing image analysis algorithms, which are commonly employed to artificially filter out artifacts prior to tomogram reconstruction (e.g. [58]).

A reduction in curtains can be achieved by adding a protective capping layer, also referred to as a sacrificial mask, onto the ROI surface. This layer is milled through first allowing for ion sputtering to primarily affect the capping layer, resulting in some surface smoothening during milling [56], [59]. This has been effective in semiconductor applications during high-current probes with a Xe sourced FIB [59]. While in biological studies, the addition of a protective Platinum (Pt) layer has minimized curtaining effects, these materials were investigated using

Ga beams [9], [51]. Precise sample preparation methods regarding capping layers for most materials have yet to be outlined, due to the complex nature of ion-material interactions. Bone has yet to be investigated using a Xe source FIB, therefore, this thesis first focused on reducing curtaining artifacts during tomography of human bone tissue.

3. Chapter 3: Materials and Methods

3.1 TEM/SAXS experiments

3.1.1 Tissue preparation

Two human femora samples were obtained with ethical approval of the Hamilton Integrated Ethics Research Board (HIREB; No. 12-085-T). In this work, we prepared a section of human femur from a 61-year-old male donor that was known to not have any bone diseases. The second human femora sample was used in the PFIB project (see section 3.2). The bone was sectioned in cross-section using a slow speed saw (Buehler Isomet, Illinois, US) under hydrated conditions to approximately 5 mm thick. The sample was then further cut such that only the cortical shell of the femur was present in the final sample, eliminating the presence of trabecular bone. The top surface of the bone section was then hand polished with 400, 800, 1200, and 2400 grit emery paper, and a 50 nm diamond suspension on a polishing cloth (Buehler, Illinois, US). The sample was slowly dehydrated in the following graded series of ethanol: 50%, 70%, 80%, 90%, 95%, 95%, 100%, and 100% mixtures for 24 hours each, in attempts to maintain the nanostructure of collagen. The sample was preserved in 100% ethanol solution for 72 hours, with solvent exchanged every 24 hours, prior to critical point drying (CPD) using a Leica EM CPD3000 (Vienna, Austria).

3.1.2 SEM for osteon selection

SEM was employed to evaluate osteonal features of the bone such that a minerally mature osteon could be selected for multiple TEM samples using FIB. The bone tissue was mounted on a stub with nickel paint and coated with 5 nm of Pt to reduce charging effects. BSE images were acquired with an accelerating voltage of 2 keV using a JSM-6610LV (JEOL Ltd., Tokyo, Japan).

In order to develop methods to investigate structurally similar tissue, all FIB lift-outs were taken from the same layers of the same osteon. Therefore, osteons were evaluated using low magnification SEM to determine their suitability for multiple FIB lift-outs. A circular osteon was desired, as round osteons are oriented normal to the imaging plane. BSE imaging was employed to determine minerally mature osteons, where osteons with a higher mineral density

appear brighter. **Figure 3.1** shows a low magnification overview representative of the sample surface and a higher magnification of the osteon selected for FIB lift-outs.
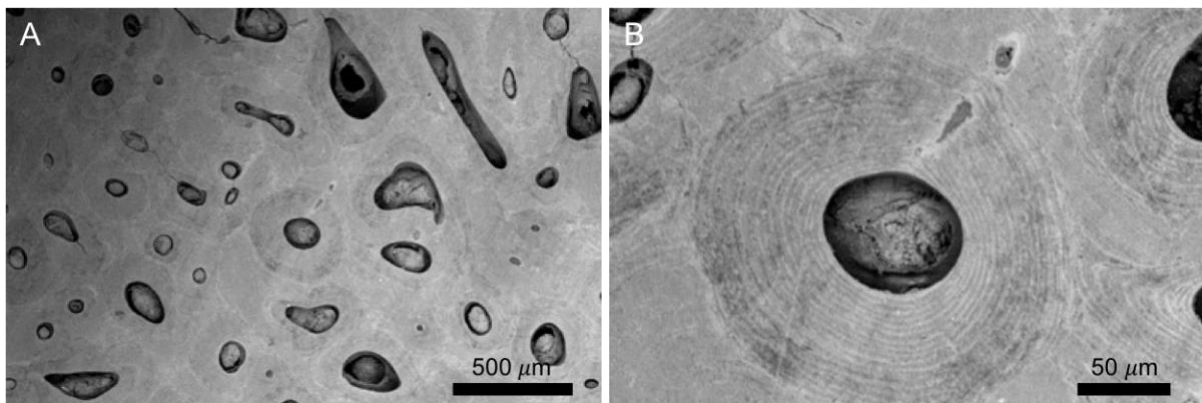
Figure 3.1. SEM micrographs of prepared osteonal bone where (A) low magnification images were used to evaluate osteon circularity and mineral maturity and one osteon (B) was selected for FIB lift-outs.

3.1.3 FIB Lift-out Preparation

The FIB lifts outs were prepared an NVision 40 (Carl Zeiss GmbH, Germany), a dual-beam instrument comprising Ga sourced FIB milling instrument, a Schottky field emission gun (FEG) sourced SEM, and a Kleindiek micromanipulator (Kleindiek Nanotechnik).

 Initially, two lift-outs were made following standard lift-out procedures, as outlined in Figure 3.2. Tungsten (W) protective capping layers of 9 μm x 2 μm and approximately 2 μm in thickness were deposited using the GIS onto the interface of the two adjacent osteonal layers beside the 8th concentric lamella. Trenches were then milled around the ROI using a decreasing beam current gradient, such that material further from the ROI could be removed faster than the material closer to the ROI to reduce damage. The cross-section was then removed using the manipulator and placed onto a TEM grid (OmniProbe), where it was milled to approximately 200 nm in thickness with an over tilt angle of 54.4 and decreasing ion current on alternating sides, followed by an electron beam cleaning polish.
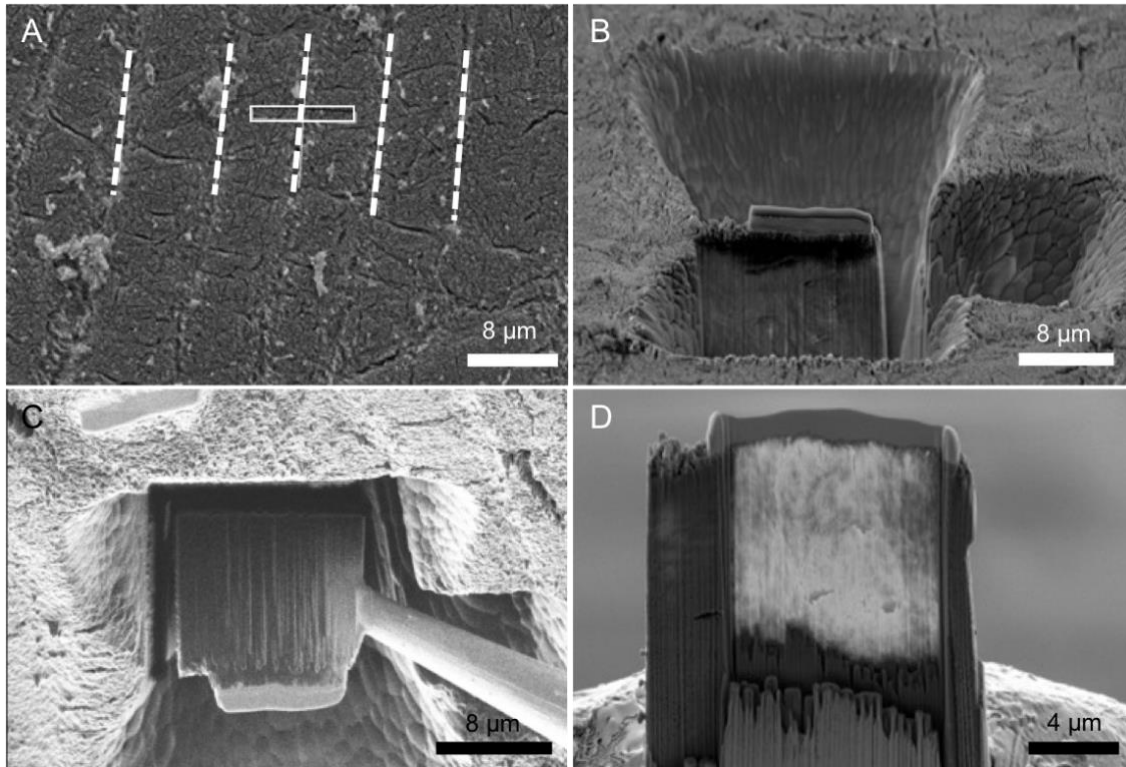
Figure 3.2. The standard FIB lift-out procedure applied in this study where (A) a ROI indicated by the white box, was selected on the 8th innermost lamella, where dotted lines indicate the individual lamella (B) A trench is milled around the ROI (C) The cross section is removed with a micro manipulator and (D) placed on a TEM grid where it is thinned until electron transparency.

After successful lift-out preparation of the first two samples, the osteon was revisited for further lift-out preparation. Surface damage was noted on the osteonal surface (Figure 3.3) and thus additional protective layers of Carbon (C) were deposited onto all future ROIs prior to milling in order to protect ROI surfaces from Ga ion damage and the re-deposition of sputtered material. After deposition, subsequent lift-outs were milled using the conditions outlined above.
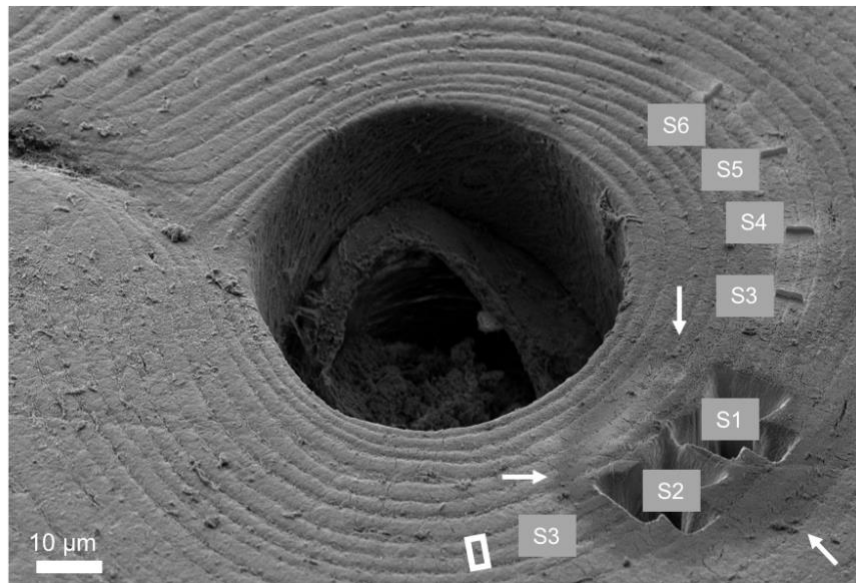
Figure 3.3. (A) The selected osteon with protective capping layers deposited on all ROIs study except sample 3, arrows indicate the region of the visible ion beam damage and the re-deposition of sputtered material from the first two lift-outs. The ROI for S3 is outlined with a box.

3.1.4 Evaluation of SAXS damage

Prior to milling FIB lift-outs, ROIs were selected for subsequent characterization, as outlined in Table 3.1. In order to increase the structural similarity between samples, adjacent samples from the osteon were selected to be imaged by one (or more) of the three techniques employed in this study: STEM, SAXS, and precession electron diffraction (PED) (not discussed in this thesis). S7 was selected as a back-up sample in case complications arose during FIB milling.

Table 3.1. A description of the characterization techniques applied to the FIB lift-outs shown in Figure 3.3.

Sample #	Characterization Technique One	Characterization Technique Two	Characterization Technique Three
1	STEM	SAXS	STEM
2	SAXS	STEM	N/A
3	PED	N/A	N/A
4	STEM	SAXS	STEM
5	SAXS	STEM	N/A
6	PED	N/A	N/A
7	N/A	N/A	N/A

To evaluate sample damage from SAXS experiments, two of the samples were first imaged using STEM, then characterized by SAXS. In the future, these samples will be re-imaged after

SAXS experiments with STEM. The other two samples were characterized by SAXS, then imaged using STEM. This was in part to ensure that the FIB lift-outs prepared were properly thinned for STEM imaging and to ensure that some samples were not exposed to the electron beam prior to SAXS. Two samples were also prepared for precession electron diffraction, which can give rise to a more detailed electron diffraction patterns than in traditional TEM electron diffraction collection [60]. The PED characterization of the samples prepared in this thesis is currently underway by collaborators at the Université de Grenoble Alpes, and therefore will not be discussed in this thesis. Detailed characterization methodologies for STEM are described below, with a small summary of the SAXS work, which is not reported in this thesis.

3.1.5 TEM imaging

A Titan $80 - 300$ microscope (FEI Company, The Netherlands) was operated at 300 keV in high-angle annular dark-field scanning transmission electron microscopy (HAADF STEM) mode for imaging. Multiple STEM images were taken of the entire FIB lift-outs at 14 000 x magnification to provide an overview. Mosaics of the STEM images were created using the MosaicJ plugin for ImageJ (National Institutes of Health) to provide stitched images of the FIB sections designated for STEM imaging. These mosaics covered the entirety of the thinned area of the FIB sample that was not heavily damaged from the ion beam, which was typically a 2 µm x 3 µm area. Select higher magnification images (115 000 x) were also obtained to visualize the collagen structure.

3.1.6 SAXS characterization

SAXS characterization was completed at the European Synchrotron Radiation Facility (ESRF) in Grenoble, France, by project collaborator Dr. Aurélien Gourier and his research team. Experiments were held at beamline ID 13, a microfocus beamline that has a 100 nm X-ray probe with an energy of $7 - 30$ keV. All four samples were characterized using SAXS methods developed by our collaborator [28], [61]. The experimental operation and analysis of SAXS data is not a part of this thesis.

3.2 PFIB experiments

3.2.1 Tissue preparation

Human femora were obtained with ethical approval of HIREB (No. 12-085-T). In this work, we prepared a section of human femur from a 68-year-old male donor that was known to not have any bone diseases. The large section of tissue was fixed in a 4% glutaraldehyde (Sigma Aldrich, Missouri, US) solution in a 0.1 M cacodylate buffer for 1 week prior to any further sample preparation. Glutaraldehyde fixation enabled cross-linking between proteins, allowing for preservation and maintenance of cellular structures within the tissue [62].

The bone was sectioned into two cross-sectional samples using a slow-speed saw (Buehler Isomet, Illinois, US) under hydrated conditions to approximately 2 – 5 mm thick. The samples were then further sectioned such that only the cortical shell of the femur was present in the final sample, eliminating the presence of trabecular bone. The samples were then treated separately, as one was subjected to demineralization, and the other was directly dehydrated and embedded. These samples are referred to as demineralized and mineralized bone, respectively. The detailed procedures for preparing the tissue are outlined in Appendix II of this thesis.

3.2.2 Sample coating and mounting

Prior to mounting on an SEM stub, the samples were both sputter coated with 5 nm of Au on the polished surfaces in two steps (Figure 3.4). The cross-sections of both samples were mounted face up onto different stubs using carbon tape for easy removal, and sputter coated with 5 nm of Au. They were then removed from the stub using tweezers and mounted onto a new stub using Ni paint such that the top surface of the sample was face up. Each sample was then sputter coated with 5 nm of Au on the top surface. This dual-side coating allowed for the reduction of image artifacts while visualizing both the top-face and cross-section of the sample with SEM during the initialization of FIB serial sectioning.
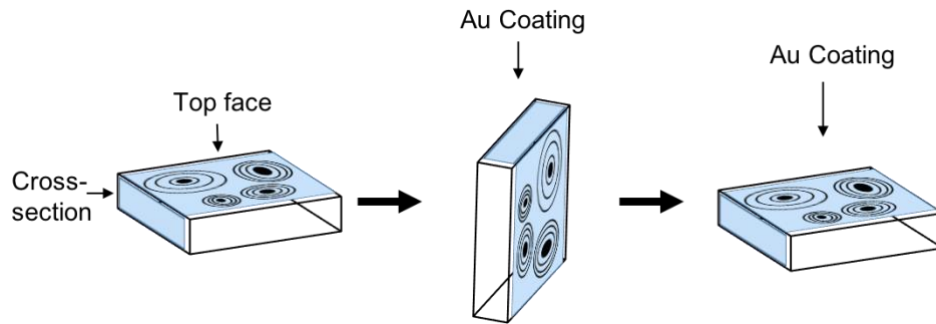
Figure 3.4. A schematic of the sample orientation during the Au coating procedure, using the mineralized tissue as an example. (A) Both the top face and the cross-section (noted in blue) are polished using procedures outlined above. (B) The cross-section that is to be imaged after serial sectioning with the FIB gun on the SEM stub and coated and (C) the top surface where the ROI is selected using the SEM is faced up on the SEM stub and coated.

3.2.3 Protective capping layer deposition

A Xe sourced PFIB (Helios G4 UXe, Thermo Scientific) equipped with a Schottky FEG sourced SEM was employed to investigate both the demineralized and mineralized bone tissue, and to optimize the protective capping layer. The GIS system was used to deposit 5 µm thick capping layers across one randomly selected area of tissue. The composition of these capping layers was varied by adding increasing amounts of C to Pt by increasing the ratio of precursor gas flux within the GIS, and vice versa. The experimental procedures and coating compositions for both demineralized and mineralized bone are outlined in the table below (Table 3.2). It is important to note, that the pure Pt and W deposits are still approximately 20% C due to the gas mixture in the GIS [63], however, it is referred to as 'pure' or 100% Pt during the rest of this thesis to avoid confusion. W was not investigated as a capping layer on mineralized tissue due to hardware issues at the time of the experiment.

Table 3.2. The composition of the protective capping layers deposited onto the top face of the bone for each experiment in this thesis, where "Exp" refers to experiment number.

	Capping Layer Composition					Deposition voltage (kV)	Deposition beam current (nA)
Demineralized Bone							
Exp. 1	Pure C	Pure W	Pure Pt	50% C to 100% Pt	80% C to 100% Pt	12	7.5
Exp. 2	Pure C	Pure W	Pure Pt			12	1
Mineralized Bone							
Exp. 3	Pure C	Pure Pt	80% C to 100% Pt	90% C to 100% Pt		12	65

3.2.3.1 Imaging and milling conditions for investigating capping layers

The investigation of the capping layer composition was completed by performing three small-scale tomography acquisitions outlined in Table 3.3. Two studies were completed on the demineralized dataset due to ion damage during the capping layer deposition in the first experiment.

Table 3.3. Capping layer optimization imaging and milling conditions, where SEM detectors are: through lens detector (TLD), circular backscatter detector (CBS), and Everhart-Thornley detector (ETD).

Conditions	Experiment 1	Experiment 2	Experiment 3
Tissue	Demineralized	Demineralized	Mineralized
Capping layer dimensions	10 x 20 x 5 μm	10 x 20 x 5 μm	20 x 40 x 5 μm
Ion milling trench conditions	1.5 μA, 30 keV	1 μA, 30 keV	1.5 μA, 30 keV
Slice thickness	15 nm	15 nm	100 nm
Number of slices	69	30	5
Rocking angle	4°	4°	0
SEM detector	TLD, CBS	TLD, CBS	EDT
Electron imaging conditions	1 keV, 2 keV	1 keV, 2 keV	1 keV
Ion milling serial section conditions	4 nA, 12 keV	4 nA, 12 keV	2.5 μA and 30 kV
Acquisition software	Slice and View™	Slice and View™	N/A, manual

3.3 PFIB tomography

PFIB serial sectioning or tomography data was acquired with capping layers of pure C and Pt for demineralized and mineralized tissues using the automated Slice and View™ (FEI Company) software, respectively, based on initial results. Tomograms were acquired with the following conditions described in Table 3.4. ROIs were selected distant from the regions were previous capping layer experiments were completed.

Table 3.4. Demineralized and mineralized bone tomogram acquisition conditions, where SEM detectors are: through lens detector (TLD) and circular backscatter detector (CBS).

Conditions	Demineralized	Mineralized
Capping layer dimensions	63 μm x 47 μm x 5 μm	150 μm x 200 μm x 5 μm
Capping layer material	Pt	C
Ion milling trench conditions	1 μA, 30 keV	1.5 μA, 30 keV
Slice thickness	20	200
Number of slices	450	300
Rocking angle	4 °	5 °
SEM Detector	CBS	TLD
Electron imaging conditions	2 keV	1 keV
Ion milling serial section conditions	4 nA, 30 keV	2.5 nA, 30 keV

3.4 Data processing

All cross-sectional images were tilt corrected using ImageJ (National Institutes of Health). Dataset alignment, reconstruction, and segmentation were completed using Dragonfly (Object Research Systems, Quebec, Canada). The demineralized tomographic dataset was aligned using the alignment function, which uses an iterative cross-correlation technique to align subsequent images to the next, accounting for stage rocking. The tomogram was reconstructed using the 3D visualization tool. Finally, the tomogram was segmented using a neural network-based function, where small-scale features were identified on a few slices, and algorithms were applied to all subsequent slices.

4. Chapter 4: Results

4.1 TEM/SAXS experiments

4.1.1 Correlative workflow

Six lift-outs were made from one osteon, such that each sample interfaced the 7th and 8th osteonal lamella layer Figure 4.1. The four lift-outs used for the STEM/SAXS correlative study are shown in Figure 4.2. For simplicity, samples will be referred to by the assigned sample number in Figure 4.1, e.g. the first sample prepared was S1, which was employed for STEM/SAXS/STEM experiments (see Table 3.1).
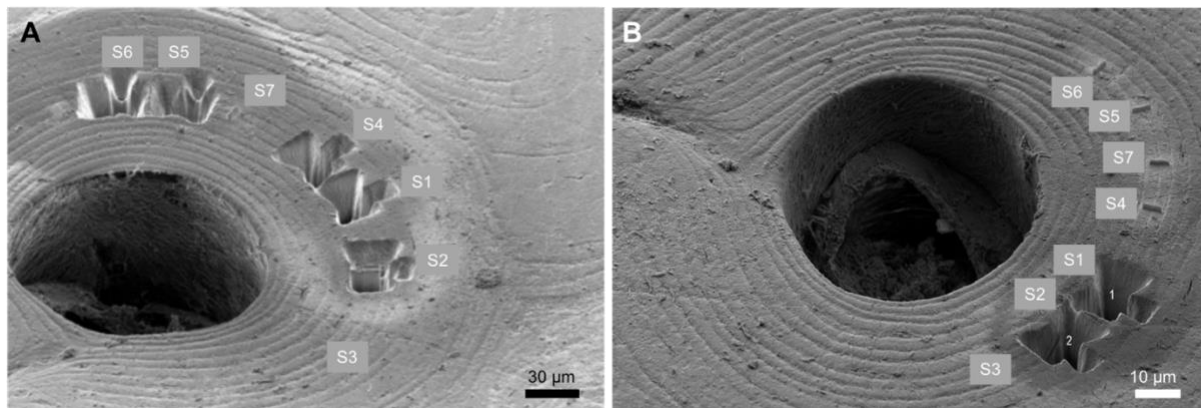
Figure 4.1. (A) SEM image of the six residual trenches from milling five samples (S1, S2, and S4 – S6) for this study, and S7 protected for future work. The ROI for S3 is outlined with a box. (B) an SEM image of the osteon at lower magnification prior to lift-out milling S3 onwards. Note the available room for at least size additional lift-outs from the same osteonal interface.
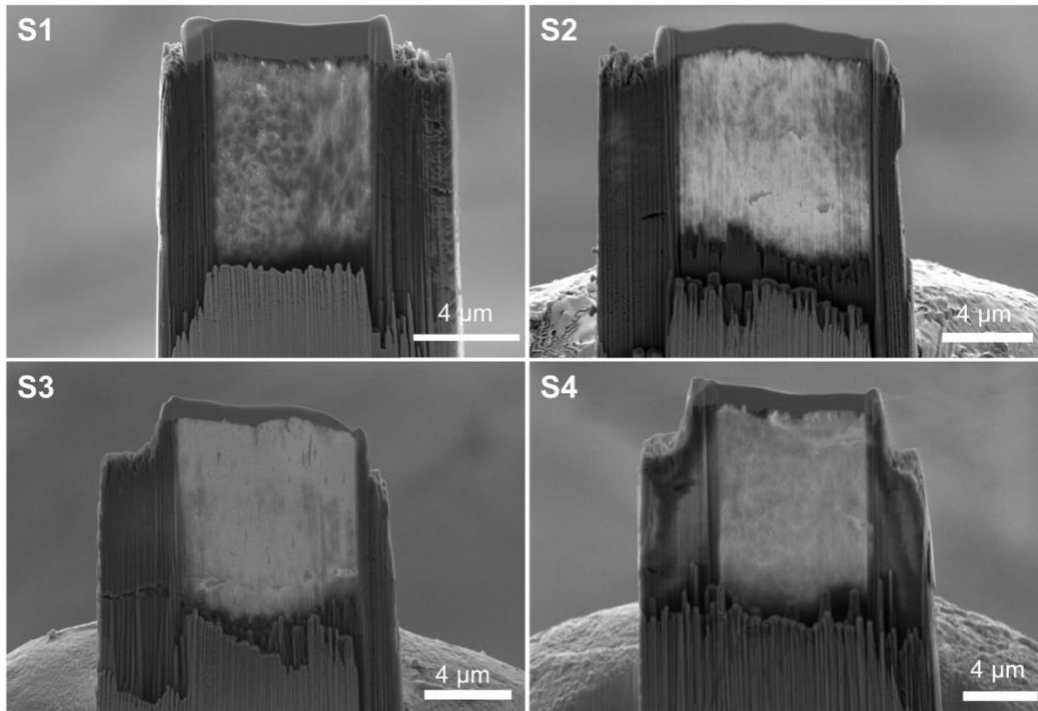
Figure 4.2. SEM images of final FIB-lift-outs used for the STEM/SAXS correlative imaging workflow of S1 – S4. All lift-outs were intact prior to evaluation with STEM and SAXS experiments.

The integrity of the lift-outs was maintained and their strong attachment to the TEM grid to enabled transfer to other labs and correlative techniques.

4.1.2 STEM evaluation of samples prior to SAXS

Mosaics of the entire lift-outs spanning approximately 9 µm x 7 µm were created from high magnification STEM images (Figure 4.3). The lift-outs span across one osteonal lamella to another, however, the directionality of the collagen fibers do not appear to abruptly change orientation. In both S1 and S4, it is clear the collagen is organized in three ways from left to right: parallel → orthogonal → parallel. Holes from the osteocyte lacunae are present in these mosaic images, as indicated in Figure 4.3.
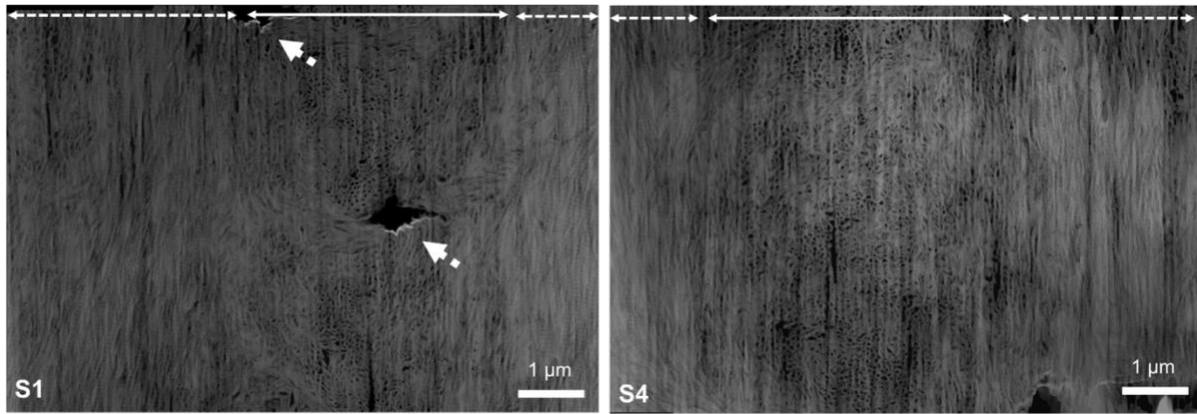
Figure 4.3. Mosaics of S1 and S4, where arrows indicate suspected osteocyte lacunae, and regions where the collagen is organized parallel and orthogonally are below the dashed and solid lines, respectively.

In both lift-outs, the bottom of the TEM window the bone material was either non-existent or extremely thin due to the FIB preparation procedure. Additionally, curtaining artifacts were present in both FIB lift-outs, however curtaining is more apparent in S4. These artifacts include the tear-drop like features at the bottom of the osteocyte lacunae and the traditional theatre curtain or waterfall-like features (Figure 4.4).
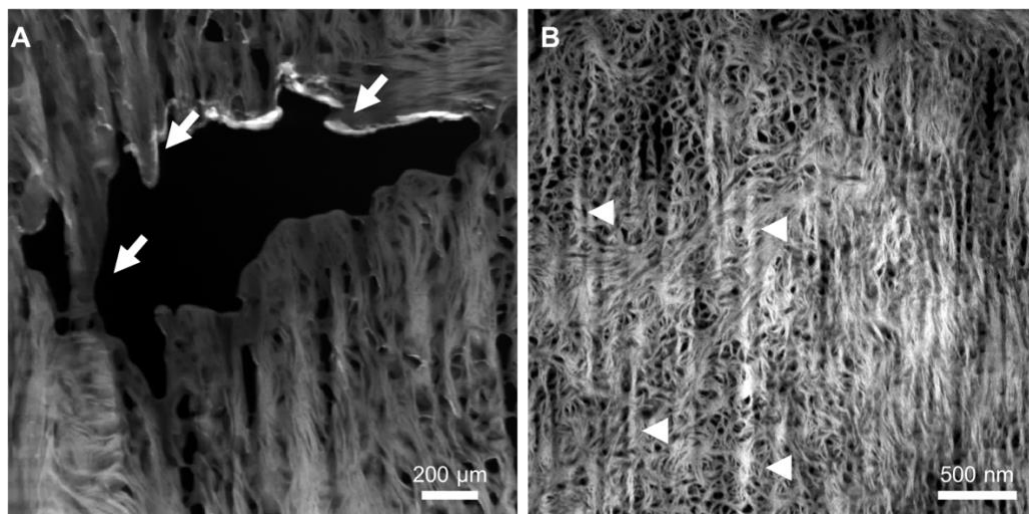
Figure 4.4. Higher magnification images of regions in the mosaics presented in Figure 4.2, identifying (A) curtaining features near the osteocyte lacune marked by arrows and (B) characteristic curtaining artifacts.

Higher magnification STEM imaging was employed to visualize the structural organization of the collagen fibrils and mineral plates prior to SAXS characterization. Figure 4.5A shows a region of the lift-out where the collagen fibrils are perpendicular to the viewing plane. Here, the black circular features are the fibrils, and the bright curved material is the mineralized plates

surrounding them. Figure 4.5B highlights collagen organized parallel to the viewing plane, such that the traditional banding pattern is observed. The crystals and fibrils remained intact in both orientations during the FIB milling process and initial STEM imaging.
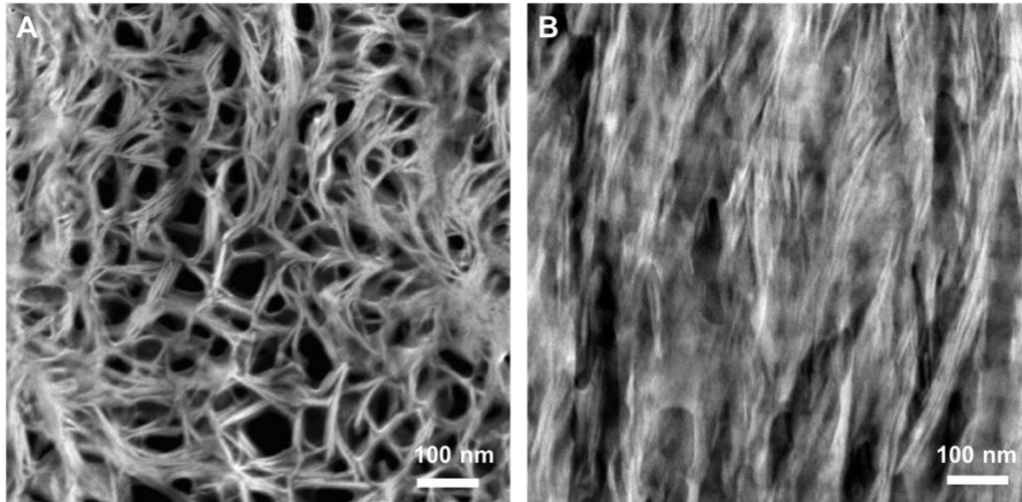
Figure 4.5. High magnification STEM images of curtain-free areas in S1. (A) collagen fibrils organized perpendicular, displayed as dark round circular features encased by curved mineral plates. (B) Collagen fibrils are organized parallel to the viewing plane, such that the characteristic banding pattern can be seen.

4.1.3 STEM evaluation of samples after SAXS characterization

Samples that were initially characterized with SAXS (S2 and S5) were subsequently imaged using STEM (Figure 4.6). Evaluation of the entire lift-out reveals that the bone structure was maintained during and after SAXS characterization, as there are no obvious regions of melting or loss of structural integrity. Near the top of the lift-outs however, the bone tissue appears to be blended with the W capping layer, which is not traditionally observed. In addition, the collagen organization was similar to S1 and S4, as it is organized in three ways from left to right: parallel → orthogonal → parallel. At higher magnifications, the majority of the collagen and mineral components remained intact (Figure 4.7), showing structures similar to those observed in the STEM mosaics of S1 and S4 prior to SAXS imaging (Figure 4.3).
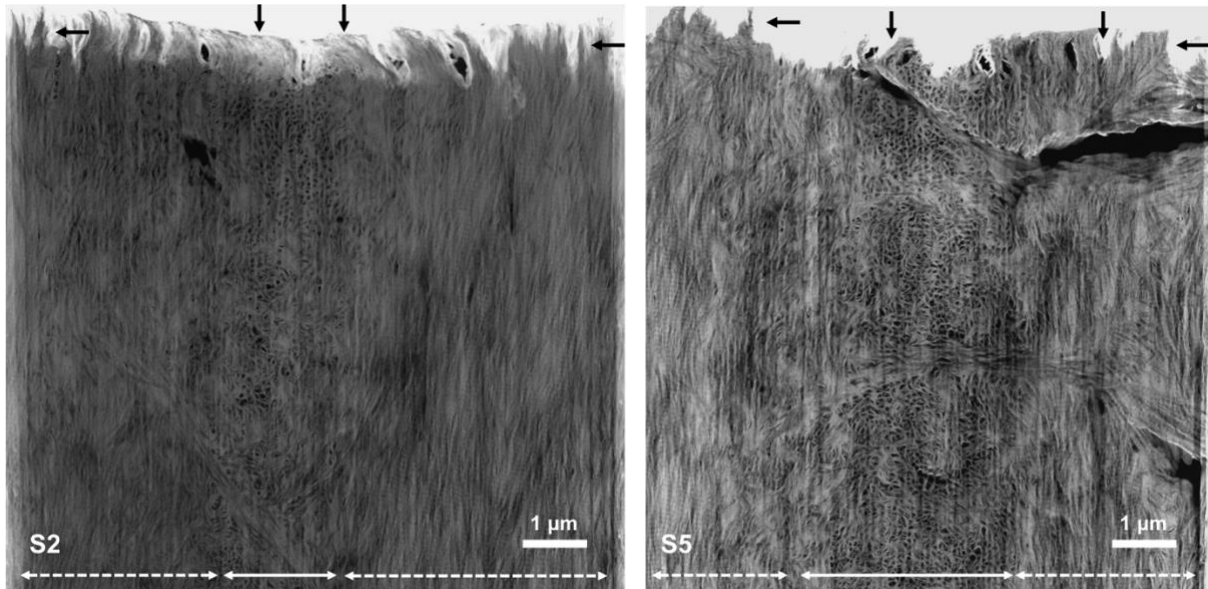
Figure 4.6. STEM mosaics of S2 and S5 after SAXS data, where solid black arrows indicate regions capping layer and bone distortion. Regions where the collagen is organized parallel and orthogonally are above the dashed and solid lines, respectively.
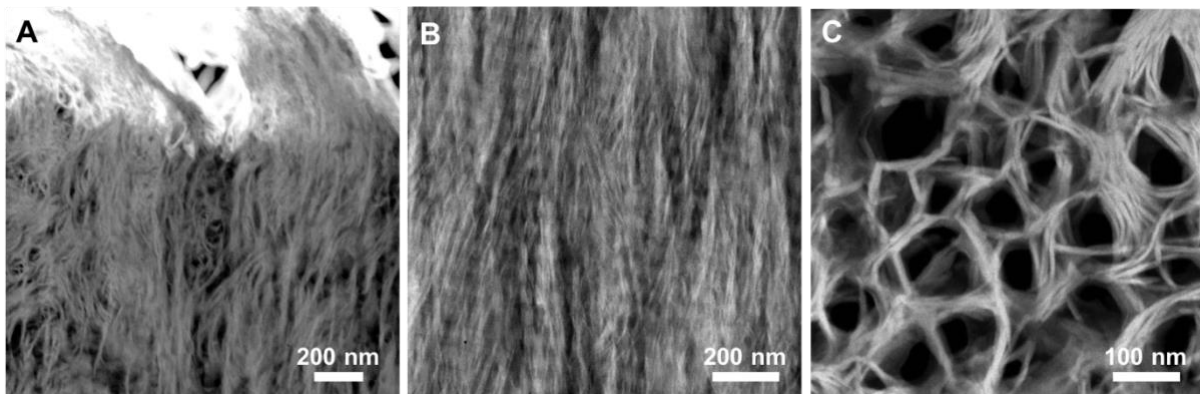
Figure 4.7. High magnification STEM images of S2 and S5 after initial SAXS characterization. (A) Blending of bone with W capping layer, where the bone appears to be curved, but maintains its periodic banding pattern. (B) Collagen fibrils with parallel orientation with intact surrounding mineral.(C) Collagen fibrils with perpendicular orientation where the periodic banding structure remains apparent.

4.2 PFIB tomography of bone

4.2.1 Capping layer investigation

4.2.1.1 Experiment 1: Demineralized bone

The results of the capping layer optimization are shown in Figure 4.8 and Figure 4.9. Deposition of the capping layers onto the surface caused the resin to bubble and the capping layer to be separated from the sample surface (Figure 4.8A). This similar damage was observed throughout the entire tomogram. Figure 4.9 shows that the region under the Pt coating is qualitatively the smoothest and has the smallest amount of curtaining artifacts. There was little to no difference observed when comparing the compound-fluxed coatings to the pure W and C coatings, as curtains were noticeable under all capping layers. Pure C appeared to have the highest density of curtaining artifacts.
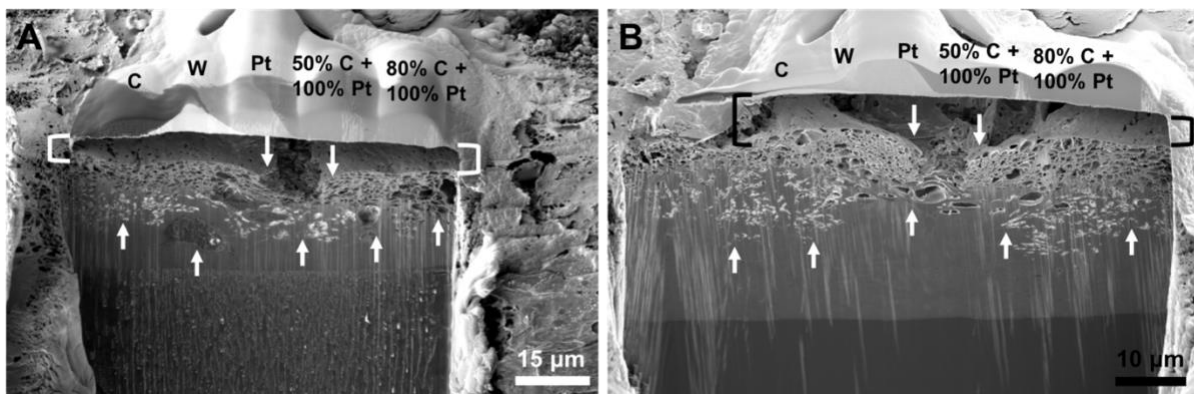
Figure 4.8. Cross-sectional SEM images of the demineralized bone (A) before and (B) after a small PFIB serial sectioning experiment to determine the effectiveness of capping layers of pure C, W, Pt, 50% C flux + 100% Pt flux, and 80% C flux + 100% Pt flux, from left to right in each image. The distance between the capping layer and sample is indicated by the square brackets and the arrows indicate obvious bubbling and sample damage.
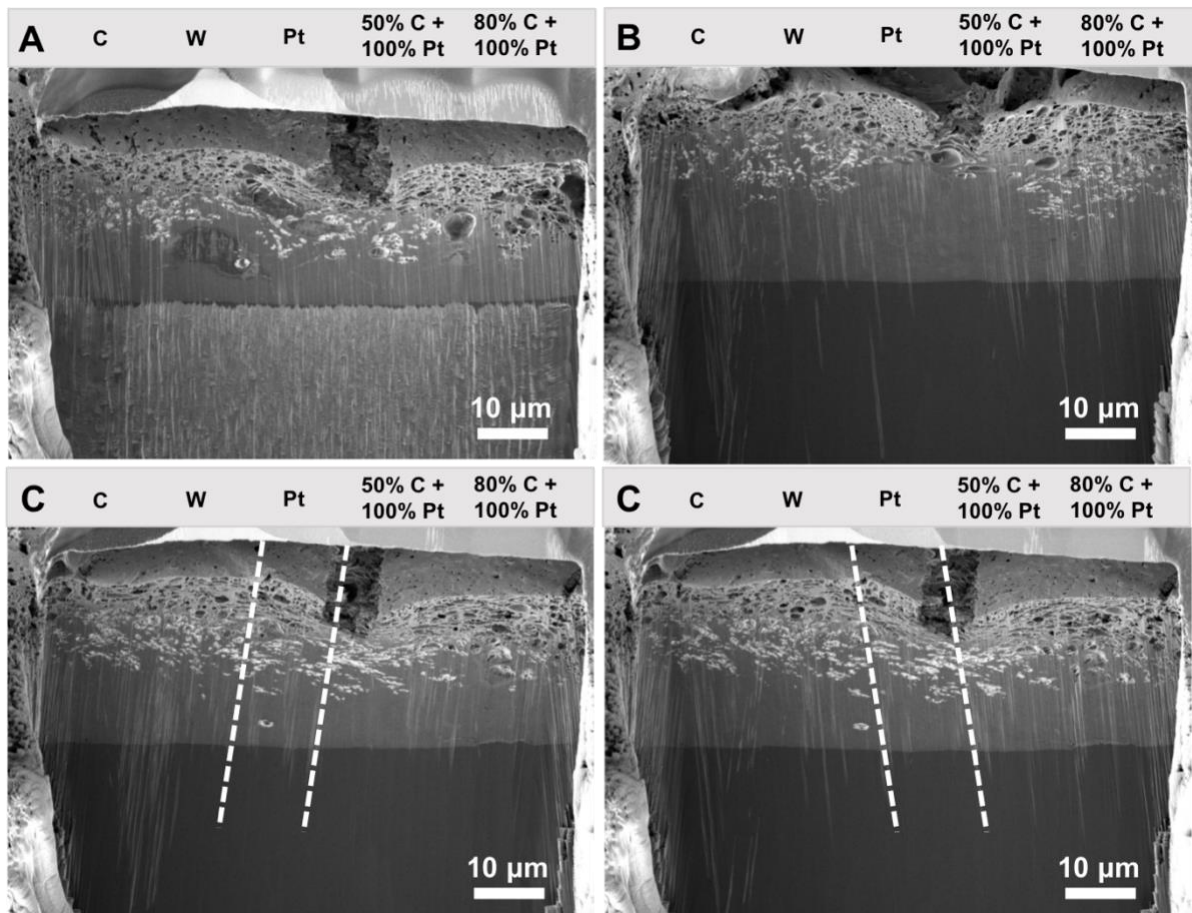
Figure 4.9. Cross-sectional SEM images of the demineralized bone obtained during a small PFIB serial sectioning experiment to determine the effectiveness of capping layers of pure C, W, Pt, 50% C flux + 100% Pt flux, and 80% C flux + 100% Pt flux, from left to right in each image. (A) The first image of the serial sectioning series, where ion beam damage and capping layer removal can be seen (B) the last image of the series and images from the middle of the series, (C) the 30th and (D) the 31st images, where the dotted lines represent the boundaries of the region affected by the Pt coating.

4.2.1.2   Experiment 2: Demineralized bone

Figure 4.10 shows the cross-sectional images after data acquisition using both a TLD and a BSE detector. The TLD provides SEI images, which reveals surface morphology and therefore curtaining artifacts. Curtains are most evident under the C capping layer and appear to be mitigated by both the Pt and W layers. BSE imaging modes reveal compositional changes, which makes the presence of curtaining features less apparent. Furthermore, structural information is lost in both images below the annotated lines in Figure 4.10. Curtains can still be visualized in this region beneath the C layer. A slightly increased number of curtains is observed under the W coating in this region compared to the Pt coating.
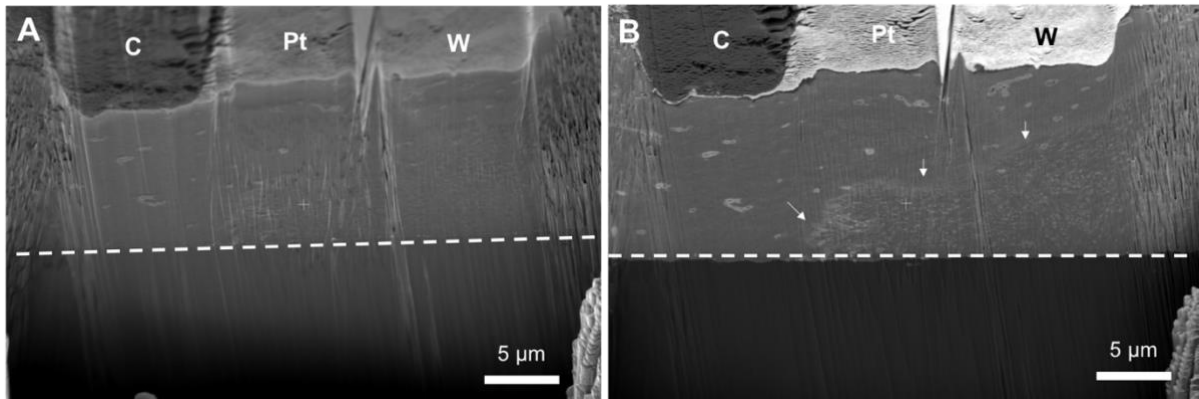
Figure 4.10. Cross-sectional SEM images obtained after a small PFIB serial sectioning acquisition to determine the effectiveness of capping layers of pure C, W, and Pt on demineralized bone. (A) TLD image, where curtaining artifacts are more visible and (B) BSE imaging where curtaining artifacts are less visible. Arrows point to the interface of suspected collagen motif orientation changes and the dotted line demonstrates the interface were sample features are no longer observed potentially due to shadowing.

This experiment also revealed what appears to be a biological interface beneath the Pt and W coating. Structures which are believed to be collagen fibrils in low magnification are present across the bottom of the image (indicated by the arrows in Figure 4.10) in two potential orientations. The images however, were collected at too low of a magnification to determine the exact orientation of the apparent fibrils. In addition, SEM images were taken after a serial sectioning experiment was acquired, meaning that the images in Figure 4.10 are the very last images in the dataset. Software issues surrounding the autofocus function in the Slice and View™ (FEI) software at the time prohibited the study of further slices, and many images throughout the serial sectioning dataset were also out of focus. Due to these complications, the dataset could not be reconstructed despite the noticeable collagen orientations present in the sample.

4.2.1.3   Experiment 3: Mineralized bone

By employing a similar method as described above, the optimal capping layer was also investigated for mineralized bone tissue. Figure 4.11 shows a clear reduction of curtains under the pure C capping layer compared to the other compositions. Curtaining artifacts appear to be more defined beneath the Pt capping layer, but in a higher density below the compound-flux layers. Due to high current milling in this experiment, the capping layer ripped from the sample surface shortly after imaging.
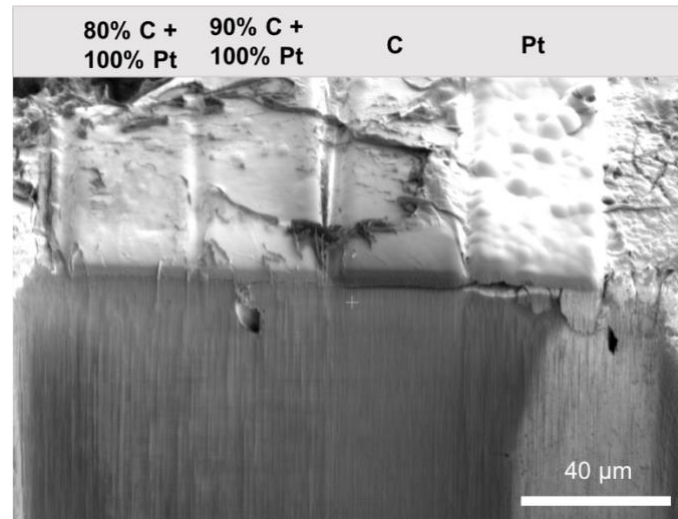
Figure 4.11. Cross-sectional SEI image obtained during a small PFIB serial sectioning experiment to determine the effectiveness of capping layers of 80% C flux + 100% Pt flux, and 90% C flux + 100% Pt flux, pure C and pure Pt from left to right. The least number of artifacts are apparent below the pure C coating.

4.2.2 PFIB tomography

4.2.2.1 Demineralized bone

Single slices of the demineralized tissue showed two very distinct features: a cell embedded in the collagen matrix and what appears to be canaliculi (Figure 4.12). Within the cell, some organelles are also resolved, including the nucleus, and the mitochondria, which is identified by its multi-envelope structure. Other membranous organelles that are less identifiable are also present throughout the cell. What is suspected to be the canaliculi are present throughout the sample as holes (Figure 4.12C). In some images, the collagen fibrils could also be resolved.
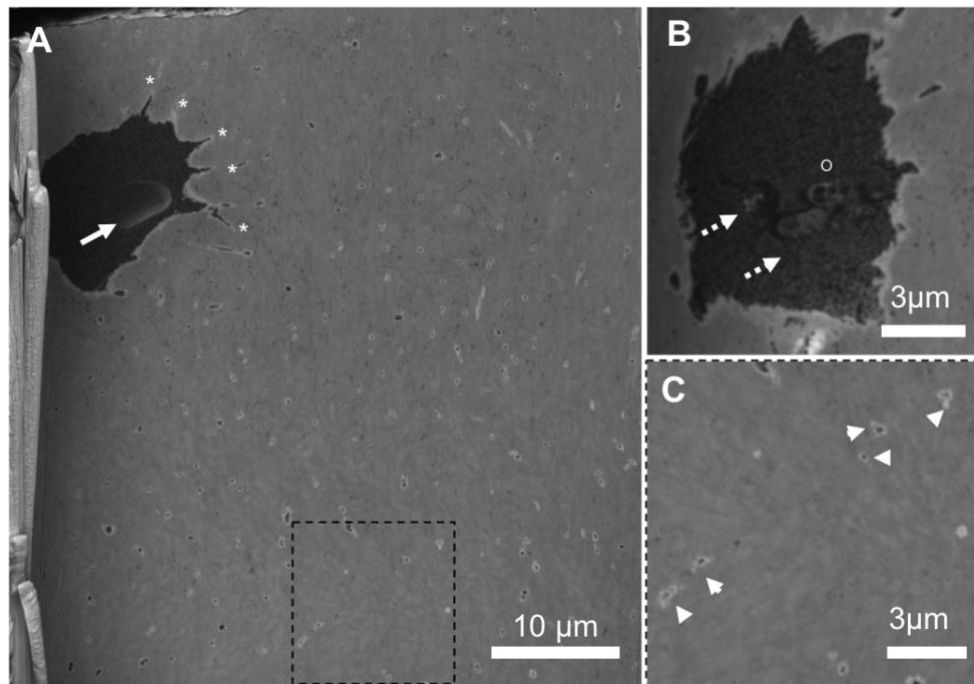
Figure 4.12. SEM cross-section images throughout the demineralized bone tomography dataset that demonstrate (A) an overview of the cross-sections obtained for the tomogram. In the top left corner, a cell is present, where the solid arrow indicates the nucleolus, and the filipodia of the cell are indicated by asterisks (*). In other slices (B) the other cellular organelles are present, and indicated by dashed arrows, the mitochondria is distinguishable and indicated by the circle. Throughout the entirety of the dataset, canaliculi are present, where the inset (C) shows an array of them in higher magnification indicated by arrowheads. It is important to note that the collagen fibrils are nearly resolved in the inset example by examining the apparent surface texture.

Reconstruction and segmentation tools have allowed for the 3D visualization of the cell and the suspected canaliculi network (Figure 4.13). After reconstruction, it was evident that the cell was, in fact, an osteocyte cell, due to the prevalent canaliculi network extending from the cell. The reconstruction shows the increased density of canaliculi proximate from the cell in the top left corner, and another region of increased density in the bottom right corner, where a small portion of another cell was present elsewhere in the data set. The final volume of this tomogram is 61.4 μm x 40.95 μm x 9 μm, which is approximately 22,000 μm^3. This is the first PFIB dataset on bone, as well as the largest bone volume from FIB tomography, and therefore the largest reconstruction with nanometer-scale resolution.
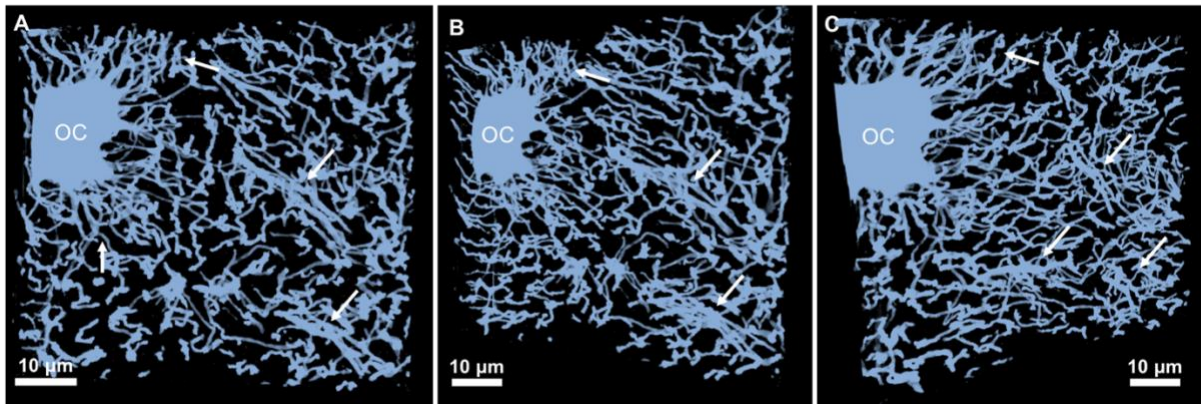
Figure 4.13. Final segmented reconstruction of the embedded cell and surrounding canaliculi in two orientations. (A) straight on view, showing the cell in the top left, and areas of dense canaliculi are indicated by the arrows, (B and C) Tilted views which better demonstrates the 3D nature of the canaliculi structures.

4.2.2.2 Mineralized bone

A pure C capping layer was deposited onto the sample surface, which included an osteonal feature, that could be milled in cross-section in hopes of visualizing osteonal lamellae using PFIB-SEM. After tomography acquisition, curtaining was still present as outlined by dashed arrows in Figure 4.14. Despite the apparent curtaining artifacts, some biological features can still be observed throughout the data set. The large dark oblong feature is the Haversian canal of the osteon, which is surrounded by osteonal lamellae, however, the orientation of collagen fibrils in each lamella cannot be resolved clearly. Osteocyte lacunae can be easily visualized, as the lack of material within these spaces provide a darker contrast compared to the bone tissue. Charging effects or brighter regions can be observed inside of the Haversian canal, which is most likely deposition from the sputter-coated Au prior to PFIB serial sectioning.
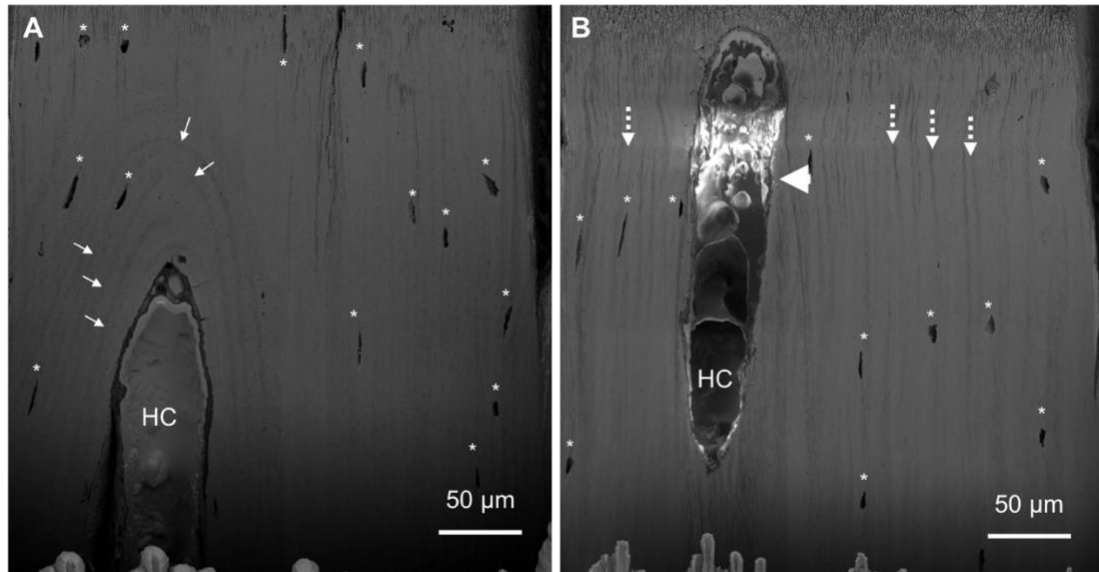
Figure 4.14. SEM cross-sectional images from the mineralized dataset that highlight the remaining curtaining artifacts (indicated by dashed arrows), the Haversian canal (labelled HC), the Au inside of the Haversian canal (indicated by the arrowhead), osteonal layers (indicated by white arrows), and osteocyte lacunae (indicated by asterisks).

Due to unforeseen challenges during image acquisition and incorrect detector setup, the tomography dataset acquired was not suitable for reconstruction. Therefore, the tomogram was not reconstructed and the only information regarding the sample could be visualized in separate 2D slices, as noted above.

5. Chapter 5: Discussion

5.1 Correlative workflow

FIB was selected for sample preparation in this work for its superior site-specificity and minimal effect on the integrity of the mineral and collagen in the ultrastructure of mineralized tissues [64]. The previous standard for the preparation of mineralized tissues for TEM characterization was ultramicrotomy and polishing [28], [65], [66], however, this technique has been demonstrated to shear the collagen fibrils and mineral plates of the bone ultrastructure [67]. As our study anticipates correlative results between STEM and SAXS, the collagen and mineral structures should remain intact prior to characterization. After FIB preparation, some regions of the lift-outs were uneven. Although the collagen constituents remained intact, curtaining features were visible on the surface or near osteocyte lacunae (Figure 4.3Figure **4.4**Figure 4.5).

Although this is one of the first correlative approaches between STEM and SAXS, these techniques have been applied for other correlative workflows to investigate mineralized tissues. SAXS is typically used in conjunction with wide angle X-ray scattering (WAXS) [68] and light microscopy [69], as WAXS can provide insight to the collagen and HA crystal orientation on the sub-nanometer scale and light microscopy can provide micro- and macro-structure organizational information. SAXS traditionally characterizes the collagen and HA crystal orientation at smaller length scales, typically ranging from 1 nm − 100 nm [5]. Meanwhile, STEM is employed to visualize the collagen and mineral components of bone ultrastructure from 10 − 100 nm and is typically coupled with electron energy loss spectroscopy (EELS) or STEM tomography [70]. More advanced correlative research between STEM and SAXS could include the addition of spectra from STEM-EELS or information from TEM diffraction.

5.1.1 Osteonal lamellae layers

All lift-outs were prepared along the interface of the 7th and 8th osteonal lamellae, which yielded four different sites for the investigation of collagen organization at the lamellar interface. Similar to work presented by Grandfield et al. (2018) [27], mosaic images (Figure 4.3 Figure **4.6**) demonstrate that there is an orientation shift observed in all samples of the collagen: parallel → orthogonal → parallel. This suggests that the collagen that comprises the osteonal

layers is orthogonal to the subsequent layer, however the width of the parallel and perpendicular regions vary, as in some lift-outs the perpendicular orientation spans more than three microns (e.g. Figure 4.3, S5), where in other lift-outs, this region is much smaller (e.g.
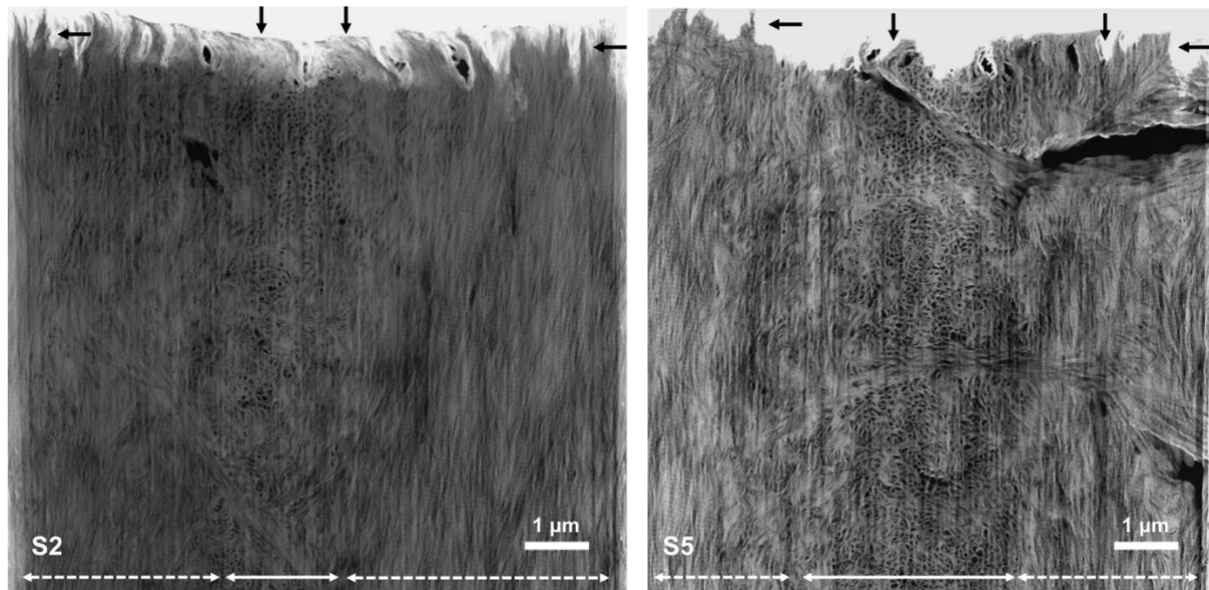
Figure **4.6**, S4). A better understanding of this organization could be achieved by completing 3D STEM tomography.

5.1.2 SAXS damage assessment

This study revealed that SAXS damage was not present when visualized with STEM. The only distortion was visualized near the top of the lift-out, which is likely attributed to alignments being completed near the top of the sample during SAXS experiment set up. Although we initially anticipated to visualize some form of damage to the collagen structure due to its relatively weak organic bonds, no visual changes were observed (an overview of SAXS damage mechanisms can be found here [71]). Other studies have observed X-ray artifacts in final SAXS reconstructions, including beam damage on macro-scale bone structures [72]. Meanwhile, smaller biological macromolecules have been investigated using atomic force microscopy (AFM) post-radiation, which revealed changes in molecule chemistry induced by SAXS radiation [73]. Our results suggest that STEM is not an adequate tool to visualize SAXS damage, and perhaps more advanced chemical spectroscopy or surface analysis techniques should be employed to investigate the changes in the collagen structure after synchrotron radiation exposure such as STEM-EELS. However, these findings do point to the conclusion

that the as-viewed in STEM structural organization of collagen fibrils and hydroxyapatite mineral is not affected by SAXS, and correlative SAXS then STEM is possible.

5.1.3 Study limitations

A critical limitation of this work was sample size, which was limited due to the complexity of each sample preparation technique. Additionally, synchrotron availability is limited, making future work and larger-scale projects challenging to fund and achieve. Therefore, this work focused on a proof-of-principal approach by using as few samples as possible.

A thorough understanding of the lift-outs prepared for this study was required, resulting in STEM imaging of two of the prepared samples prior to SAXS imaging. The samples that were initially imaged using STEM, followed by SAXS characterization were not reimaged after being subjected to the X-ray beam. Therefore, we cannot comment on the difference in sample integrity for those that were subjected to the X-ray beam first or second within the workflow. However, it is apparent that the electron beam exposure to the samples likely induced knock-on damage [42], which has the potential to influence SAXS results. Furthermore, STEM damage weakens the organic bonds of the bone material, potentially causing the tissue to be more susceptible to SAXS. Future work should focus on creating more samples for SAXS without prior STEM imaging to determine if the STEM damage contributes to visible SAXS damage. However, this comes with the drawback of foregoing prior knowledge of the sample structure for comparison after SAXS.

5.1.4 Future work

This study aimed to assess X-ray damage qualitatively, however no dramatic differences were observed. Future work should focus on developing a quantitative method to analyze the collagen and mineral components of the bone ultrastructure by analyzing collagen fibril size and mineral thickness using the STEM images acquired before and after SAXS analysis. With the study design employed in this thesis, both ion and electron damage to the FIB lift-outs could not be fully assessed. Ion damage was only noted visually in two samples prior to synchrotron characterization, meanwhile, electron damage from the initial STEM imaging was not assessed at all in SAXS. Future work should focus on assessing the ion and electron beam damage induced during both sample preparation and STEM characterization of bone, prior to SAXS

experiments. Both scanning transmission X-ray microscopy and X-ray absorption have been demonstrated to successfully identify electron and ion damage, respectively [74], [75]. Future works should also focus on determining a method to successfully evaluate the mode of damage most prevalent, by exploring spectroscopy-based techniques such as STEM-EELS despite its high radiation dose.

5.2 PFIB serial sectioning of human bone tissue

5.2.1 Curtaining reduction

For the demineralized and mineralized bone, the most effective capping layer compositions were found to be Pt and C, respectively. This is likely attributed to the similar hardness of the tissue the respective capping layer. A harder capping layer (C) for the mineralized tissue, and a softer capping layer (Pt) for the demineralized tissue. Capping layers are critical for both the protection of the ROI surface and for the reduction of curtaining, which arises from preferential milling [56]. The capping layer should, therefore, be uniform and have a low hardness mismatch relative to the sample, as changes in hardness and material composition can increase curtaining effects, as observed in this thesis. This is exemplified in metallic substrates, as inclusions and grain orientation can increase curtaining artifacts [55], [56].

Our results suggest that the relative hardness of the capping layer with respect to the sample hardness plays a critical role in the capping layer-based reduction in curtaining artifacts. The relative hardness of the FIB-deposited material is currently only understood empirically. The relative hardness of capping layer materials are best described by their respective placement on the Mohs hardness scale. The hardness of the capping layer materials in their bulk form are: 10, 3.5, and 7.5 for C, Pt, and W respectively [76], [77]. It is important to note that the C deposited in the FIB is diamond-like amorphous C which is known for its increased hardness due to its mixture between sp^2 and sp^3 bonds [78], and therefore the Vickers hardness for diamond-like C was noted. The increasing order of hardness of the materials investigated in this thesis is: Pt, W, and C.

The demineralized tissues is the collagen network of bone, which has a hardness of $0.1 - 0.15$ GPa [79] and was embedded in Embed 812, which is suspected to have a similar hardness. Pt was most effective in reducing curtaining on the sample. The mineralized bone was initially

suspected to be fully infiltrated by the resin. Charging effects or brighter regions, can be observed inside of the Haversian canal (Figure 4.14), which is most likely sputtered material from the Au coating prior to PFIB serial sectioning, suggesting that the bone material was not fully infiltrated by the embedding resin, and thus, that hardness of cortical bone must also contribute to the hardness of the bulk sample. The nanohardness of native cortical bone ranges from 0.234 to 0.760 GPa [80], which is harder than the demineralized bone. The C capping layer, which was the hardest capping layer investigated in this study, was most effective at reducing the curtains in the mineralized bone.

Somewhat similar observations have been made in the Xe milling of semiconductor materials, as a thin crystalline Si wafer has been used to protect devices from curtaining with success when compared to standard capping materials [59] like those investigated in this thesis. It is suggested that the uniformity of the Si wafer allows for curtaining mitigation, however this has yet to be attempted on other materials [59].

5.2.2 Biological structures in 3D

This thesis presents the first PFIB serial sectioning of the osteocyte network of both demineralized and mineralized bone (2D: Figure 4.12Figure 4.14 3D: Figure 4.13), which provides visualization of this network at nanoscale resolution. The notion of visualizing the osteocyte lacuna-canalicular network in healthy bone tissue will help better understand disease onset in bone tissue within the biomedical community. µ-CT has been employed to obtain a 3D visualization of the osteocyte lacuna-canalicular network with micron-scale resolution, however the many connections of the canalicular network are barely resolvable [81]. Previous research has also employed µ-CT using synchrotron radiation sources to investigate these structures to reveal the interconnectedness of the network at nanoscale resolution. These datasets, however, have limited volumes and usually suffer from a low signal-to-noise ratio, meaning that more complex image processing algorithms are required for segmentation [10], [82]. Traditional Ga FIB has also been employed to quantify and differentiate the transition between the osteocyte and canaliculi at 30 nm resolution, however only the lacunae were imaged instead of the cellular network [51]. PFIB tomography bridges these methods, allowing for the potential of nano-scale quantification of the canaliculi in 3D across large volumes at a similar resolution to nano-CT.

Prior to 3D reconstruction of the demineralized bone, it was unclear if the cell observed in the dataset was an osteoblast or osteocyte, as both are mononuclear cells that can reside in demineralized bone tissue. The reconstruction however, made it evident that this dataset is in fact of the osteocyte lacuna-canalicular network. A higher density of the canaliculi was observed near the osteocyte cell and a lower density of the canaliculi were noted adjacent to the cell, in the region where the two cellular networks connect. This has yet to be noted in 3D images obtained by more traditional cellular imaging techniques such as confocal microscopy [83]. This further demonstrates the need for 3D imaging of the complex mesoscale features of bone.

Furthermore, FIB has been employed in the biological community to investigate cellular structures including organelles and conformational membrane changes. For example, the investigation of human immunodeficiency virus-infected cells has revealed elements of the viral pathway [84]. However, most FIB tomography of biologicals is completed under cryogenic conditions, as the cellular structure is maintained in a hydrated state (advances in cryo-FIB in cellular applications reviewed here: [85]). In the demineralized PFIB tomogram obtained in this thesis, some organelles were revealed within the embedded cell under standard FIB operating conditions. The cell and organelles were maintained because the bone was initially fixed prior to sample preparation, which cross-links cell and organelle membranes [62]. PFIB is not predicted to be the preferred method for investigating cellular organelles, as the large beam currents can be more destructive and high resolution of the cellular components may not be achievable. In addition, there are many sophisticated optical techniques that can image cellular organelles in 3D [85] without the complex sample preparation and operation required for electron microscopy.

PFIB serial sectioning has the potential to reveal the collagen network in 3D in demineralized bone tissue as well, however this was not pursued in this thesis. Although apparent collagen networks could be seen in 2D serial sections (Figure 4.10 and Figure **4.12**), 3D reconstructions of the networks were unachievable due to microscope instability and dataset inhomogeneity. During the tomography acquisitions, the focus controlled by the automated software was unsuccessful, leaving images periodically out of focus. Approximately one-third of the demineralized tomography data is insufficient focus to visualize the collagen network meaning that the network cannot be properly segmented. Additionally, in Figure 4.10 we have a limited view of the collagen fibril organization, further limiting our understanding of the collagen

organization at this interface. The lack of proper visualization could be attributed to either (1) an extreme reduction in sample thickness in this area or (2) shadowing within the bottom portion of the ROI. At the time of the experimental acquisitions, automated focusing scripts were still under development on this new piece of infrastructure. The successful implementation of them in the future would enable simultaneous resolution of the collagen and osteocyte lacunae networks. This thesis demonstrates that the PFIB has the potential to observe these features across volumes at least 100 times greater than those already achieved with Ga FIB [9].

PFIB investigation of mineralized tissue was less fruitful than the investigation of demineralized tissue, however, some features were still resolvable in 2D. The resolvable biological features included microscale constituents such as the Haversian canal of the osteon and the borders of osteonal lamellae. The collagen structure of the lamellae cannot be clearly resolved, likely due to the contrast contribution by the relatively high-Z Ca and P elements present in the bone mineral. This suggests that mineralized bone specimens cannot be used to investigate osteonal layering with PFIB serial sectioning despite previous success investigating on the microscale with 2D using polarized light microscopy [86] and on the nanoscale using STEM [27], which have contributed to the understanding of the circularity of osteons and the concentric orientation of the lamellae.

Finally, PFIB serial sectioning may have the capacity to image the bone-implant interface at high resolution across a large volume regardless if the bone tissue is mineralized or demineralized. Typically, a correlative approach including micro-CT, 2D SEM imaging, and TEM imaging or 3D TEM tomography is used to visualize the bone-implant interface [49], [87]. PFIB tomography will provide insight to bone-implant anchoring across the mesoscale, something that has yet to be achieved with conventional methods. Other optical methods, such as confocal microscopy, cannot be employed in these instances due to the opacity of the implant material, making electron microscopy a required characterization tool.

5.2.3 Study limitations

This study was initiated during the installation of a new microscope, and therefore presented several instrumental limitations such as minimal availability and reoccurring instrument stability and hardware downtime issues. This thesis focused on investigating the capping layer

composition, however both imaging and milling conditions also need to be optimized to ensure successful tomograms.

Although interesting biological information was obtained from this study, the ROIs were not selected based on biological significance, but instead based on minimizing complications during operation. This thesis acted as a proof-of-concept study to demonstrate that PFIB can be applied in the biological community, specifically for the investigation of bone tissue. Additionally, samples were selected based on availability and the two bone sections investigated were therefore sectioned along opposite axes, making direct biological comparisons difficult. For instance, if this thesis investigated a cross-section of mineralized and demineralized bone, it would be clear if PFIB could be employed to image the directionality of collagen in these layers in demineralized bone.

5.2.4 Future work

5.2.4.1 Capping layer composition

Future studies should work on determining the hardness of bone material and deposited capping layers, such that a more thorough understanding of the capping layer hardness mismatch and curtaining reduction can be achieved. Additionally, alternative capping layers including the Si wafer mask suggested by Subramaniam (2017) [59] could be investigated.

5.2.4.2 Sample preparation suggestions

Complete resin infiltration will be necessary for the investigation of bone-implant interfaces using PFIB serial sectioning, as voids can lead to curtaining artifacts and ambiguity during segmentation. Full resin infiltration of mineralized tissue should not affect the capping layer composition, as the hardness of Embed 812 can be increased significantly by increasing the volume percent of the hardener component to better match the hardness of bone tissue [88]. In addition, infiltration could be completed under vacuum, to help reduce voids and resin bubbling at the resin-bone interface. Moreover, to increase imaging contrast in the mineralized bone tissue, immunostaining could be used, as it has been demonstrated successful at staining egg shells, another mineralized tissue, for light-based imaging techniques [89]. In the future, with the appropriate instrumentation, cryo-FIB milling, which has been demonstrated to be successful for smaller scale bone tomography [31] could also be investigated.

5.2.4.3 Biological relevance

More comprehensive comparisons between demineralized and mineralized bone material should be completed, such that the same mesoscale features are being investigated in both samples. This would provide further insight into the potential for PFIB applications on these biological structures, and the effect of demineralization on the understanding of bone structure. In addition, larger tomography datasets should be obtained. In both the tomograms presented in this work, the z dimension is much smaller than the x and y, which can easily be increased with longer acquisition times.

6. Chapter 6: Conclusions

6.1 Summary of major findings

6.1.1 Correlative STEM and SAXS

This research aimed to fulfilled its initial objectives, to: (1) develop a correlative workflow to allow for the characterization of osteonal bone using STEM and SAXS, and (2) assess the damage induced by SAXS of bone tissue at the nanoscale. The presented research fulfilled one of its initial objectives, which was to develop a correlative workflow to allow for the characterization of osteonal bone using STEM and SAXS. This thesis also demonstrated that according to STEM evaluation, SAXS did cause damage to the structural units of bone at the nanoscale.

It is imperative to develop correlative microscopy techniques to characterize the intricacies of bone ultrastructure. Our results demonstrate the potential of using traditional FIB TEM lift-out methods to create functional samples for both TEM and SAXS analysis The workflow presented in this thesis allows for visualization of the identical areas of bone tissue using both sophisticated techniques, which has yet to be achieved prior to this work. Here, we demonstrated that STEM is a valid method to visualized SAXS damage of mineralized bone tissue, which has yet to be validated in the literature. Here, we demonstrated that STEM did not detect any visual signs of SAXS induced damage to mineralized bone tissue. While it may be possible that the SAXS experimental conditions and sample thickness limited damage, it may also be possible that STEM is insufficient to measure the damage mechanism that is taking place. Further research needs to be employed to determine how to better characterize the

radiation damage of bone tissue after SAXS irradiation. However, we can confidently say that the structural units as observed by STEM, are not visually altered by the SAXS technique.

6.1.2 PFIB of bone tissue

The research outlined in this thesis achieved another major objective, which was to test PFIB tomography sample preparation methods to investigate mesoscale bone structures with nanoscale resolution. To our knowledge, we are the first to visualize human bone tissue using Xe sourced FIB, and currently present the largest volume at the highest resolution tomogram of the osteocyte lacuna-canalicular network achieved by an SEM source.

PFIB tomography is an emerging technique that has not yet been thoroughly researched for biological applications, including the characterization of bone tissue. This thesis determined the optimal capping layer composition of the capping layer materials tested for mineralized and demineralized bone tissue to be Pt and C, respectively, as curtaining was qualitatively decreased with these layers. This work demonstrated the ability of the PFIB to visualize the osteocyte lacuna-canalicular network in 3D in demineralized bone tissue. In addition, this work has demonstrated the instrument's potential to image the collagen network in 3D, but this was not fully achieved in this work. The mineralized bone tissue was also not visualized in 3D, however it was made apparent that only larger-scale or micron-scale features could be resolved within the mineralized tissue. Due to these promising results, this thesis substantiates the notion that PFIB could be considered a sophisticated 3D imaging tool for better understanding not only healthy bone tissue, but perhaps diseased bone, and the bone-implant interface with many engineered devices.

7. Chapter 7: References

[1]   K. Grandfield, "Bone, implants, and their interfaces," *Phys. Today*, vol. 68, no. 4, pp. 40–45, 2015.

[2]   N. Reznikov, J. A. M. Steele, P. Fratzl, and M. M. Stevens, "A materials science vision of extracellular matrix mineralization," *Nat. Rev. Mater.*, vol. 1, no. 8, pp. 1–15, 2016.

[3]   P. Fratzl, H. S. Gupta, E. P. Paschalis, and P. Roschger, "Structure and mechanical quality of the collagen–mineral nano-composite in bone," *J. Mater. Chem.*, vol. 14, no. 14, pp. 2115–2123, 2004.

[4]   N. Reznikov, R. Shahar, and S. Weiner, "Bone hierarchical structure in three dimensions," *Acta Biomater.*, vol. 10, no. 9, pp. 3815–3826, 2014.

[5]   M. Georgiadis, R. Müller, and P. Schneider, "Techniques to assess bone ultrastructure organization: orientation and arrangement of mineralized collagen fibrils.," *J. R. Soc. Interface*, vol. 13, no. 119, 2016.

[6]   T. Ando, S. P. Bhamidimarri, and N. Brending, "The 2018 correlative microscopy techniques roadmap," *J. Phys. D. Appl. Phys.*, vol. 51, no. 443001, pp. 1–42, 2018.

[7]   R. F. Egerton, "Control of radiation damage in the TEM," *Ultramicroscopy*, vol. 127, pp. 100–108, 2013.

[8]   J. B. Hopkins and R. E. Thorne, "Quantifying radiation damage in biomolecular small-angle X-ray scattering," *J. Appl. Crystallogr.*, vol. 49, no. 3, pp. 880–890, 2016.

[9]   N. Reznikov, R. Shahar, and S. Weiner, "Three-dimensional structure of human lamellar

bone: The presence of two different materials and new insights into the hierarchical organization," *Bone*, vol. 59, pp. 93–104, 2014.

[10]   F. Peyrin, P. Dong, A. Pacureanu, and M. Langer, "Micro- and Nano-CT for the Study of Bone Ultrastructure," *Curr. Osteoporos. Rep.*, vol. 12, no. 4, pp. 465–474, 2014.

[11]   K. Grandfield, a. Palmquist, and H. Engqvist, "High-resolution three-dimensional probes of biomaterials and their interfaces," *Philos. Trans. R. Soc. A Math. Phys. Eng. Sci.*, vol. 370, pp. 1337–1351, 2012.

[12]   B. Clarke, "Normal bone anatomy and physiology.," *Clin. J. Am. Soc. Nephrol.*, vol. 3 Suppl 3, pp. 131–139, 2008.

[13]   L. I. Plotkin and T. Bellido, "Osteocytic signalling pathways as therapeutic targets for bone fragility," *Nat. Rev. Endocrinol.*, vol. 12, no. 10, pp. 593–605, 2016.

[14]   R. Florencio-Silva, G. R. da S. Sasso, E. Sasso-Cerri, M. J. Simões, and P. S. Cerri, "Biology of Bone Tissue: Structure, Function, and Factors That Influence Bone Cells.," *Biomed Res. Int.*, vol. 2015, p. 421746, 2015.

[15]   H. P. Schwarcz, "The ultrastructure of bone as revealed in electron microscopy of ion-milled sections," *Semin. Cell Dev. Biol.*, vol. 46, 2015.

[16]   R. Gottardi *et al.*, "Supramolecular Organization of Collagen Fibrils in Healthy and Osteoarthritic Human Knee and Hip Joint Cartilage," *PLoS One*, vol. 11, no. 10, p. e0163552, 2016.

[17]   M. Tzaphlidou, "The role of collagen in bone structure: An image processing approach," *Micron*, vol. 36, no. 7–8, pp. 593–601, 2005.

[18]   M. M. Giraud-Guille, "Twisted plywood architecture of collagen fibrils in human compact bone osteons," *Calcif. Tissue Int.*, vol. 42, no. 3, pp. 167–180, May 1988.

[19]   E. Hamed, I. Jasiuk, A. Yoo, Y. Lee, and T. Liszka, "Multi-scale modelling of elastic moduli of trabecular bone.," *J. R. Soc. Interface*, vol. 9, no. 72, pp. 1654–73, 2012.

[20]   W. Landis, et al., "Mineral and organic matrix interaction in normally calcifying tendon visualized in three dimensions by high-voltage electron microscopic tomography and

graphic image reconstruction," *J. Struct. Biol.*, vol. 110, no. 1, pp. 39–54, 1993.

[21] N. Reznikov, R. Almany-Magal, R. Shahar, and S. Weiner, "Three-dimensional imaging of collagen fibril organization in rat circumferential lamellar bone using a dual beam electron microscope reveals ordered and disordered sub-lamellar structures," *Bone*, vol. 52, no. 2, pp. 676–683, 2013.

[22] H. P. Schwarcz, E. A. McNally, and G. A. Botton, "Dark-field transmission electron microscopy of cortical bone reveals details of extrafibrillar crystals," *J. Struct. Biol.*, vol. 188, no. 3, pp. 240–248, 2014.

[23] K. S. Chan, C. K. Chan, and D. P. Nicolella, "Relating crack-tip deformation to mineralization and fracture resistance in human femur cortical bone.," *Bone*, vol. 45, no. 3, pp. 427–34, 2009.

[24] S. Weiner, T. Arad, I. Sabanay, and W. Traub, "Rotated plywood structure of primary lamellar bone in the rat: Orientations of the collagen fibril arrays," *Bone*, vol. 20, no. 6, pp. 509–514, 1997.

[25] S. Weiner, W. Traub, and H. D. Wagner, "Lamellar Bone: Structure–Function Relations," *J. Struct. Biol.*, vol. 126, no. 3, pp. 241–255, 1999.

[26] E. M. Spiesz, W. Kaminsky, and P. K. Zysset, "A quantitative collagen fibers orientation assessment using birefringence measurements: Calibration and application to human osteons," *J. Struct. Biol.*, vol. 176, no. 3, pp. 302–306, Dec. 2011.

[27] K. Grandfield, V. Vuong, and H. P. Schwarcz, "Ultrastructure of Bone: Hierarchical Features from Nanometer to Micrometer Scale Revealed in Focused Ion Beam Sections in the TEM," *Calcif. Tissue Int.*, vol. 103, no. 6, pp. 606–616, 2018.

[28] M. Granke *et al.*, "Microfibril Orientation Dominates the Microelastic Properties of Human Bone Tissue at the Lamellar Length Scale," *PLoS One*, vol. 8, no. 3, p. e58043, 2013.

[29] T. Bellido, "Osteocyte-driven bone remodeling.," *Calcif. Tissue Int.*, vol. 94, no. 1, pp. 25–34, 2014.

[30] Y. Imai *et al.*, "Nuclear Receptors in Bone Physiology and Diseases," *Physiol. Rev.*, vol. 93, no. 2, pp. 481–523, 2013.

[31] N. Reznikov, H. Chase, V. Brumfeld, R. Shahar, and S. Weiner, "The 3D structure of the collagen fibril network in human trabecular bone: Relation to trabecular organization," *Bone*, vol. 71, pp. 189–195, 2015.

[32] D. M. Binkley and K. Grandfield, "Advances in Multiscale Characterization Techniques of Bone and Biomaterials Interfaces," *ACS Biomater. Sci. Eng.*, p. acsbiomaterials.7b00420, 2017.

[33] X. Ni *et al.*, "YphC and YsxC GTPases assist the maturation of the central protuberance, GTPase associated region and functional core of the 50S ribosomal subunit.," *Nucleic Acids Res.*, vol. 44, no. 17, pp. 8442–55, 2016.

[34] M. Malatesta, "Transmission electron microscopy for nanomedicine: novel applications for long-established techniques.," *Eur. J. Histochem.*, vol. 60, no. 4, p. 2751, 2016.

[35] A. Razi, R. A. Britton, and J. Ortega, "The impact of recent improvements in cryo-electron microscopy technology on the understanding of bacterial ribosome assembly.," *Nucleic Acids Res.*, vol. 45, no. 3, pp. 1027–1040, 2017.

[36] E. McNally, H. Schwarcz, G. Botton, and A. Arsenault, "A model for the ultrastructure of bone based on electron microscopy of ion-milled sections," *PLoS One*, vol. 7, no. 1, 2012.

[37] N. Reznikov, M. Bilton, L. Lari, M. M. Stevens, and R. Kröger, "Fractal-like hierarchical organization of bone begins at the nanoscale.," *Science*, vol. 360, no. 6388, p. eaao2189, 2018.

[38] A. A. Sousa and R. D. Leapman, "Development and application of STEM for the biological sciences.," *Ultramicroscopy*, vol. 123, pp. 38–49, Dec. 2012.

[39] D. Williams and B. Carter, *Transmission electron microscopy*. New York: Plenum, pp. 161, 1996.

[40] H. Friedrich, P. E. de Jongh, A. J. Verkleij, and K. P. de Jong, "Electron Tomography

for Heterogeneous Catalysts and Related Nanostructured Materials," *Chem. Rev.*, vol. 109, no. 5, pp. 1613–1629, 2009.

[41]   R. F. Egerton, P. Li, and M. Malac, "Radiation damage in the TEM and SEM," *Micron*, vol. 35, no. 6, pp. 399–409, 2004.

[42]   M. R. Libera and R. F. Egerton, "Advances in the transmission electron microscopy of polymers," *Polym. Rev.*, vol. 50, no. 3, pp. 321–339, 2010.

[43]   A. Boyde and C. Wood, "Preparation of animal tissues for surface-scanning electron microscopy," *J. Microsc.*, vol. 90, no. 3, pp. 221–249, 1969.

[44]   V. Lešer, D. Drobne, Ž Pipan, M. Milani, and F. Tatti, "Comparison of different preparation methods of biological samples for FIB milling and SEM investigation," *J. Microsc.*, vol. 233, no. 2, pp. 309–319, 2009.

[45]   L. A. Giannuzzi and F. A. Stevie, "A review of focused ion beam milling techniques for TEM specimen preparation," *Micron*, vol. 30, pp. 197–204, 1999.

[46]   N. Bassim, K. Scott, and L. A. Giannuzzi, "Recent advances in focused ion beam technology and applications," *MRS Bull.*, vol. 39, no. 04, pp. 317–325, 2014.

[47]   B. Van Leer, R. Kelley, A. Genc, and A. Savenko, "Xe+ FIB milling and measurement of amorphous damange in diamond," *Microsc. Microanal.*, vol. 22, pp. 178–179, 2016.

[48]   L. Giannuzzi, "Reducing FIB Damage Using Low Energy Ions," *Microsc. Microanal.*, vol. 12, no. S02, pp. 1260–1261, 2006.

[49]   J. Tedesco *et al.*, "Osseointegration of a 3D Printed Stemmed Titanium Dental Implant: A Pilot Study," *Int. J. Dent.*, vol. 2017, pp. 1–11, 2017.

[50]   M. D. Uchic, L. Holzer, B. J. Inkson, E. L. Principe, and P. Munroe, "Three-Dimensional Microstructural Characterization Using Focused Ion Beam Tomography," *MRS Bull.*, vol. 32, no. 05, pp. 408–416, 2007.

[51]   P. Schneider, M. Meier, R. Wepf, and R. Müller, "Serial FIB/SEM imaging for quantitative 3D assessment of the osteocyte lacuno-canalicular network.," *Bone*, vol. 49, no. 2, pp. 304–311, 2011.

[52] A. P. Cocco *et al.*, "Three-dimensional microstructural imaging methods for energy materials," *Phys. Chem. Chem. Phys.*, vol. 15, no. 39, pp. 16377–16407, 2013.

[53] T. L. Burnett *et al.*, "Large volume serial section tomography by Xe Plasma FIB dual beam microscopy," *Ultramicroscopy*, vol. 161, pp. 119–129, 2016.

[54] N. S. Smith, J. A. Notte, and A. V. Steele, "Advances in source technology for focused ion beam instruments," *MRS Bull.*, vol. 39, no. 4, pp. 329–335, 2014.

[55] S. Rubanov and P. Munroe, "The application of FIB milling for specimen preparation from crystalline germanium," *Micron*, vol. 35, no. 7, pp. 549–556, 2004.

[56] T. Ishitani, K. Umemura, T. Ohnishi, T. Yaguchi, and T. Kamino, "Improvements in performance of focused ion beam cross-sectioning: Aspects of ion-sample interaction," *J. Electron Microsc. (Tokyo).*, vol. 53, no. 5, pp. 443–449, 2004.

[57] T. H. Loeber *et al.*, "Reducing curtaining effects in FIB/SEM applications by a goniometer stage and an image processing method," *J. Vac. Sci. Technol. B, Nanotechnol. Microelectron. Mater. Process. Meas. Phenom.*, vol. 35, no. 6, p. 06GK01, 2017.

[58] C. W. Schankula, C. K. Anand, and N. D. Bassim, "Multi-Angle Plasma Focused Ion Beam (FIB) Curtaining Artifact Correction Using a Fourier-Based Linear Optimization Model," *Microsc. Microanal.*, vol. 24, no. 6, pp. 657–666, 2018.

[59] S. Subramaniam, J. Huening, J. Richards, and K. Johnson, "A Comprehensive Approach Towards Optimizing the Xenon Plasma Focused Ion Beam Instrument for Semiconductor Failure Analysis Applications," *Microsc. Microanal.*, vol. 23, no. 04, pp. 769–781, 2017.

[60] P. A. Midgley and A. S. Eggeman, "Precession electron diffraction – a topical review," *IUCrJ*, vol. 2, no. 1, pp. 126–136, 2015.

[61] M. Reynolds *et al.*, "A micro-reactor environment for combined micro-X-ray micro-Raman studies of nanomaterials," *Tech. Proc. 2013 NSTI Nanotechnol. Conf. Expo, NSTI-Nanotech 2013*, vol. 1, pp. 16–19, 2013.

[62] A. Oryan, A. Kamali, A. Moshiri, H. Baharvand, and H. Daemi, "Chemical crosslinking of biopolymeric scaffolds: Current knowledge and future directions of crosslinked engineered bone scaffolds," *Int. J. Biol. Macromol.*, vol. 107, no. PartA, pp. 678–688, 2018.

[63] I. Utke, P. Hoffmann, and J. Melngailis, "Gas-assisted focused electron beam and ion beam processing and fabrication," *J. Vac. Sci. Technol. B Microelectron. Nanom. Struct.*, vol. 26, no. 4, p. 1197, 2008.

[64] K. Grandfield and H. Engqvist, "Focused Ion Beam in the Study of Biomaterials and Biological Matter," *Adv. Mater. Sci. Eng.*, vol. 2012, pp. 1–6, 2012.

[65] A. Gourrier *et al.*, "Nanoscale modifications in the early heating stages of bone are heterogeneous at the microstructural scale," *PLoS One*, vol. 12, no. 4, pp. 1–23, 2017.

[66] M. Georgiadis *et al.*, "3D scanning SAXS: A novel method for the assessment of bone ultrastructure orientation," *Bone*, vol. 71, pp. 42–52, 2015.

[67] V. Jantou, M. Turmaine, G. D. West, M. A. Horton, and D. W. McComb, "Focused ion beam milling and ultramicrotomy of mineralised ivory dentine for analytical transmission electron microscopy," *Micron*, vol. 40, no. 4, pp. 495–501, 2009.

[68] I. Žižak *et al.*, "Investigation of bone and cartilage by synchrotron scanning-SAS and -WAXD with micrometer spatial resolution," *J. Appl. Crystallogr.*, vol. 33, no. 3 I, pp. 820–823, 2000.

[69] C. Giannini *et al.*, "Correlative light and scanning X-ray scattering microscopy of healthy and pathologic human bone sections.," *Sci. Rep.*, vol. 2, p. 435, 2012.

[70] X. Wang, F. A. Shah, A. Palmquist, and K. Grandfield, "3D Characterization of Human Nano-osseointegration by On-Axis Electron Tomography without the Missing Wedge," *ACS Biomater. Sci. Eng.*, vol. 3, no. 1, pp. 49–55, 2017.

[71] M. Warkentin *et al.*, "Global radiation damage: temperature dependence, time dependence and how to outrun it," *J. Synchrotron Radiat.*, vol. 20, no. 1, pp. 7–13, 2013.

[72] S. Ma *et al.*, "Synchrotron Imaging Assessment of Bone Quality," *Clin. Rev. Bone

Miner. Metab., vol. 14, no. 3, pp. 150–160, 2016.

[73]   L. Costa *et al.*, "Combined small angle X-ray solution scattering with atomic force microscopy for characterizing radiation damage on biological macromolecules," *BMC Struct. Biol.*, vol. 16, no. 1, pp. 1–13, 2016.

[74]   L. G. A. Melo and A. P. Hitchcock, "Electron beam damage of perfluorosulfonic acid studied by soft X-ray spectromicroscopy," *Micron*, vol. 121, no. 2018, pp. 8–20, 2019.

[75]   N. D. Bassim *et al.*, "Minimizing damage during FIB sample preparation of soft materials," *J. Microsc.*, vol. 245, no. 3, pp. 288–301, 2012.

[76]   W. Benenson, *Handbook of Physics*. New York: Spinger, pp. 170 - 172, 2001.

[77]   G. V. Samsonov, *Handbok of the Physiochemical Properties of the Elements*. New York: Plenum Publishing Coperation, pp. 442, 1968.

[78]   J. Robertson, "Diamond-like amorphous carbon," *Mater. Sci. Eng. R Reports*, vol. 37, no. 4–6, pp. 129–281, 2002.

[79]   S. Isaza, "Characterization of the mechanical and morphological properties of cortical bones by nanoindentation and Atomic Force Microscopy," Université de Technologie de Compiègne, 2014.

[80]   P. K. Zysset, X. Edward Guo, C. Edward Hoffler, K. E. Moore, and S. A. Goldstein, "Elastic modulus and hardness of cortical and trabecular bone lamellae measured by nanoindentation in the human femur," *J. Biomech.*, vol. 32, no. 10, pp. 1005–1012, 1999.

[81]   F. Peyrin, A. Pacureanu, M. A. Zuluaga, P. Dong, and M. Langer, "3D X-ray CT imaging of the bone Lacuno-Canalicular Network," *Proc. - Int. Symp. Biomed. Imaging*, pp. 1788–1791, 2012.

[82]   M. A. Zuluaga, *et al.*, "Bone canalicular network segmentation in 3D nano-CT images through geodesic voting and image tessellation," *Phys. Med. Biol.*, vol. 59, no. 9, pp. 2155–2171, 2014.

[83]   C. B. Bozal, L. M. Sánchez, and A. M. Ubios, "The lacuno-canalicular system (LCS) and osteocyte network of alveolar bone by confocal laser scanning microscopy

(CLSM).," *Acta Odontol. Latinoam.*, vol. 25, no. 1, pp. 123–31, 2012.

[84]   G. A. Frank *et al.*, "Maturation of the HIV-1 core by a non-diffusional phase transition," *Nat. Commun.*, vol. 6, pp. 1–9, 2015.

[85]   F. Huang *et al.*, "Ultra-High Resolution 3D Imaging of Whole Cells.," *Cell*, vol. 166, no. 4, pp. 1028–1040, 2016.

[86]   T. G. Bromage, H. M. Goldman, S. C. McFarlin, J. Warshaw, A. Boyde, and C. M. Riggs, "Circularly polarized light standards for investigations of collagen fiber orientation in bone," *Anat. Rec. - Part B New Anat.*, vol. 274, no. 1, pp. 157–168, 2003.

[87]   A. Thorfve, A. Palmquist, and K. Grandfield, "Three-dimensional analytical techniques for evaluation of osseointegrated titanium implants," *Mater. Sci. Technol.*, vol. 31, no. 2, pp. 174–179, 2015.

[88]   A. . Glauert, "A survey of embedding media for electron microscopy," *J. R. Microsc. Soc.*, vol. 80, no. 4, pp. 269–277, 1962.

[89]   D. Athanasiadou *et al.*, "Nanostructure, osteopontin, and mechanical properties of calcitic avian eggshell," *Sci. Adv.*, vol. 4, no. 3, pp. 1–14, 2018.

8. Chapter 8: Appendix I

Here, the work titled "Advances in Multiscale Characterization Techniques of Bone and Biomaterials Interfaces" published in *ACS Biomaterials Science and Engineering* in 2017 is reprinted with kind permissions from the American Chemical Society [32]. This acts as a review of imaging techniques used for imaging bone and bone-implant devices that are not thoroughly discussed in this thesis.

Advances in Multiscale Characterization Techniques of Bone and Biomaterials Interfaces

Dakota M. Binkley[†] and Kathryn Grandfield*[,†,‡]

[†]Department of Materials Science and Engineering and [‡]School of Biomedical Engineering, McMaster University, Hamilton, Ontario L8S 4L8, Canada

ABSTRACT: The success of osseointegrated biomaterials often depends on the functional interface between the implant and mineralized bone tissue. Several parallels between natural and synthetic interfaces exist on various length scales from the microscale toward the cellular and the atomic scale structure. Interest lies in the development of more sophisticated methods to probe these hierarchical levels in tissues at both biomaterials interfaces and natural tissue interphases. This review will highlight new and emerging perspectives toward understanding mineralized tissues, particularly bone tissue, and interfaces between bone and engineered biomaterials at multilength scales and with multidimensionality. Emphasis will be placed on highlighting novel and correlative X-ray, ion, and electron beam imaging approaches, such as electron tomography, atom probe tomography, and in situ microscopies, as well as spectroscopic and mechanical characterizations. These less conventional approaches to imaging biomaterials are contributing to the evolution of the understanding of the structure and organization in bone and bone integrating materials.

KEYWORDS: *biomineralization, osseointegration, electron microscopy, atom probe tomography, bone, mineralized tissues*
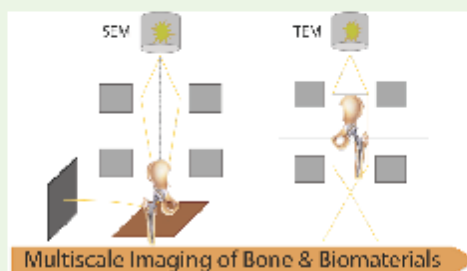
1. INTRODUCTION

Continued advances in biomaterials development and characterization stem from the need for biomedical devices to facilitate the functional repair of tissues. One such tissue that biomaterials technologies are still sought to repair is bone tissue. Specific interest lies in bone augmentation or regeneration, joint replacement, and dental restoration technologies, where maintenance of bone health and quality in these scenarios is integral to restoring daily functions such as, skeletal mobility, and mastication.[1] Bone, however, is a hierarchical material with heterogeneous structure and chemistry across multiple length scales.[2] This complexity has made the development and understanding of the attachment of bone to implant materials, or osseointegration, an ongoing challenge.[3]

Therefore, to further the investigation of biomaterials toward osteogenic applications, we require a complete understanding of the mechanisms at the bone interface, and also the natural interphases within the host bone tissue. An interface can be described as the abrupt connection between two differing materials, for example, with distinct differences in chemical or mechanical properties, such as bone and titanium. Quite similar to an interface, the term interphase has been used to describe the location where two materials conjoin, however, this junction is comprised of a gradual change between two materials composed of comparable chemical constituents or materials properties, a prime natural example of this are the interphases within teeth: the cementum-dentin-junction and

the dentin-enamel- junction.[4] Our group has contributed toward this field by the development of multidimensional and multilength scale characterizations of osseointegrated materials interfacing to bone tissue.[3,5,6]

In this review, we aim to provide insights into a wider array of novel approaches to investigate bone, its natural interphases, and the bone–implant interface. After a brief introduction on bone and osseointegrated implants, the review is organized by the length scale from the micron and cellular level, to the nano and atomic scale, to real-time processes for the investigation of mineralization. Special emphasis is placed on electron, X-ray, and ion-based imaging techniques that can be used to resolve bone structure and bone–implant interfaces along their many hierarchical levels; however, spectroscopic and mechanical characterizations are also briefly mentioned. This work aims to highlight less conventional techniques that are making their mark on the landscape of osseointegration and biomineralization research. The structure of the review, and breakdown of techniques covered, is further outlined in this brief table of contents:
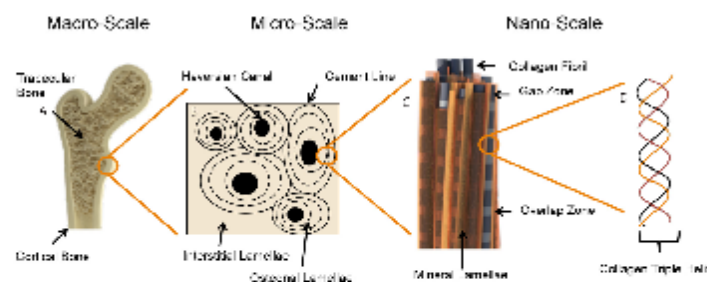
Figure 1. Hierarchical structure of bone from the macro- to nanoscale. (A) At the macroscale, bone is organized into the well-known structures of cortical or trabecular bone. Moving to successively smaller length scales, (B) osteons and trabeculae (not shown) comprise the basic microscale structural units of bone. Cortical bone is organized such that multiple Haversian canals run through each set of concentric osteonal lamellae. The cement line is a highly mineralized component of the osteon, which is the interphase between the osteon and the interstitial lamellae. (C) On the nanoscale, bone comprises mineralized collagen fibrils, where a predominant amount of bone mineral surrounds the apparent collagen banding pattern of gap and overlap zones, (D) formed by the staggered connection of Type I collagen molecules with their characteristic triple helix structure. Panel c adapted with permission from ref 141. Copyright 2014 Elsevier.
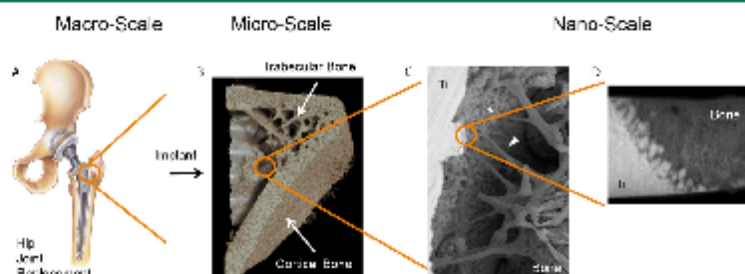
Figure 2. Hierarchical characterization of osseointegration from the macro- to nanoscale. Similar to bone, the connection at bone−implant interfaces spans several length scales. As an example, (A) a titanium hip joint or dental implant in connection with bone can be visualized by (B) microcomputed tomography, demonstrating the overall bone growth toward the implant material, as well as trabecular and cortical microscale structure. (C) Using SEM, the importance of cellular attachment to the implant material is clear, and (D) once further magnified by TEM, a clear nanoscale integration is visualized, where the bone and implant material seem to mix with one another. Adapted with permission from our works in refs 6, 34, and 49. Copyright 2017 American Chemical Society, 2015 Taylor & Francis, and 2015 American Chemical Society.

2. Mineralized Interfaces of Interest: topics include bone structure and organization, biomaterials for osseointegration

3. At the Micron and Cellular Level: techniques include scanning electron microscopy & quantitative back-scattered electron imaging, micro computed tomography, focused ion beam tomography, synchrotron-radiation tomography, small angle X-ray scattering

4. At the Nano and Atomic Scale: techniques include transmission electron microscopy, electron tomography, atom probe tomography, atomic force microscopy, nanoindentation

5. In Real Time: techniques include liquid cell TEM, computed tomography, magnetic resonance imaging

2. MINERALIZED INTERFACES OF INTEREST

Bone: Structure and Organization. Prior to understanding how biomaterials integrate with bone tissue, it is important to grasp the basics of the structural and chemical organization of bone. Bone comprises two main components: collagen, an ubiquitous protein found in many tissues, and bone mineral, specifically a calcium phosphate in the form of either hydroxyapatite (HA), carbonated-HA (cHA), or amorphous calcium phosphate (ACP).[7] By weight, bone consists of roughly 65% mineral and 35% collagen. This composite structure is responsible for the optimal materials properties displayed by bone, specifically, its inherent strength and toughness.[8,9] These core components of collagen and hydroxyapatite form the mineralized collagen fibrils that create the building blocks of higher order architectures that are intricately organized on multiple length scales, such as collagen fibers and osteonal lamellae.[8,10] Some of these hierarchical features are outlined in Figure 1. At even higher-level architectures, bone can be separated into two forms, trabecular (cancellous) spongy bone and cortical or compact bone. This hierarchical structure further provides bone with increased durability, making the skeleton less susceptible to skeletal fractures upon mild impacts.[9] In addition to mechanical integrity, bone hosts many biological functions such as storing bone marrow, which contains the adaptive immune response and governs blood cell production.[11] Furthermore, bone is a dynamic material, constantly remodeling throughout its lifetime to adapt to mechanical loads, and chemical signals.[12,13] More recent works that review bone hierarchical structure are widely available.[14]

B

Review

Table 1. Brief List of Imaging and Spectroscopic Techniques Used To Assess Bone Tissue and Bone−Implant Interfaces and Their Respective Benefits and Limitations

technique	benefits	limitations	references
		At the Micron and Cellular Level	
SEM	compositional information	2D imaging	27−29,38,40,49,50,56−58,107,109
	surface topology	potential electron damage	
	can be coupled with e.g. AFM and FIB	bone must be dehydrated	
	good depth of field	sample coating with a conductive layer is usually required	
Micro-CT	3D visualization at micron scale	X-ray attenuation artifacts if material density differs, e.g., bone and metal	30,33,35,50
	dry and wet conditions	limited resolution to several microns (unless using synchrotron source)	
FIB Tomography	3D visualization	destructive technique	10,37,39,42,44
	nanoscale resolution	potential for ion beam damage to biological materials	
		At the Nanometer Level	
SAXS	ability to determine structural information, mineral crystal size, orientation and thickness	low signal-to-noise ratio	53,54
		intensive postprocessing of data	
		synchrotron source required	
TEM	multiple imaging modes (e.g., BF, DF, HAADF, STEM)	intensive sample preparation	11,19−36
	couple with characterization tools (e.g., EDS, EELS)	small sample size	
	nanometer resolution	potential for electron beam damage	
		samples must be dehydrated	
electron tomography	3D visualization of mineral and collagen interplay	physical limitations based on rectangular sample geometry (missing wedge)	18,37,39,48,55,59,60,63−64,66−70,86,111,117,118
	high-resolution	potential for electron beam damage due to long acquisition times	
		intensive postprocessing of data	
		sample must be dehydrated	
liquid cell	real-time observation of mineralization	decreased image resolution due to electron scattering events in liquid	61,106,116,118,119,121−124,126,128
	samples maintain hydrated state (natural environment)	beam induced mineralization	
		confined liquid volume	
		At the Atomic Level	
APT	3D imaging and chemical information	data collection limited by sample fragility, low conductivity, heterogeneous crystal and organic structure	86−96
	high spatial resolution	intensive sample preparation	
	high chemical sensitivity	complex reconstruction and data processing	

Biomaterials for Osseointegration. Brånemark was the first to coin the term osseointegration as the functional connection between bone and implant devices in the 1950s.[15] Since then, biomaterials have been investigated for their potential to osseointegrate with bone. This connection is governed not by surgical methodologies, but by the ability of bone-forming cells, osteoblasts, to secrete mineral toward and on foreign objects, integrating them within the native bone to create an attachment to the implant surface that supports mechanical loading.

Several materials are used in osseointegrated implants, but titanium has garnered the most attention as an implantable material for correcting bone fracture, joint replacement, and tooth loss.[16,17] The success of this material relies on its biocompatibility, which has been attributed to the inherent oxide layer on the metal surface.[18] In addition, the suitable mechanical properties of titanium provide the necessary strength to allow the skeleton to maintain its structural integrity.[17] Of course a plethora of other natural and synthetic bone implant materials are regularly used, sometimes in conjunction with titanium implants, including bone grafts: either autografts, bone material from the host, or allografts from a donor.[19,20] These grafts, and other natural biomaterials such as proteins[21] and polymer matrices,[22] can either be directly placed in wound sites or around titanium bone implants, in hopes of increasing bone growth and ultimately minimizing device failure.[20]

Despite the potential titanium shows as an appropriate bone integrating biomaterial, complications arise due to the increased elastic modulus titanium has in comparison to bone. As titanium is much stiffer than bone, it can overcompensate for surrounding bone tissue, resulting in the resorption of host tissue; a process termed stress-shielding, further reviewed elsewhere.[23] However, it is believed that the formation of a gradual interphase and strong integration between bone and implant would allow transfer of loading and effectively decrease the effect of stress-shielding.

Similar to the tissue with which it bonds, the bone−implant interface is hierarchical in structure, Figure 2. Despite great advances in titanium bone−implant design and surgical implantation practices, failure rates among these materials remain sufficiently high, with implant loosening or osteolysis contributing to a large portion of failures,[3] and increased patient risk for secondary surgeries.[24] Although biomaterials are

C

being engineered daily to solve these problems of integration, assessment of these with suitable techniques is constantly developing with technological advances in software, hardware, and data handling methods. Approaches to some less conventional techniques to enable visualization of this bone–implant interface across hierarchical levels are presented here, with some examples outlined initially in Figure 2.

3. AT THE MICRON AND CELLULAR LEVEL

Electrons, X-rays, and Ions. Historically, interphases in bone tissue and bone–implant interfaces were investigated using traditional life-science microscopical approaches, such as light microscopy, and more specifically histology. These methods were used to evaluate bone health through the identification of relevant biological cells, such as osteoblasts and osteoclasts.[25,26] However, while biologically relevant, these approaches are limited by the resolution of the light microscope. The use of X-rays, electrons and ions as imaging sources has enabled an increase in resolving power and allowed more advanced imaging techniques that could be used in both clinical and research settings. Herein, we will discuss novel imaging approaches for understanding features of bone structure and biomineralization that have emerged at the micron scale and level of cellular structures in bone.

The micron scale, where bone units are represented by osteons and trabeculae, is of interest for the evaluation of both bone pathology and osseointegration. At this essential level, the most basic characterization approaches include scanning electron microscopy (SEM), and microcomputed tomography (micro-CT), with focused ion beam (FIB) microscopy bringing the newest perspectives to the field. A complete summary of all of the techniques presented at each length scale can be found in Table 1.

SEM uses a focused electron beam rastered across the surface of a specimen to produce several signals for imaging and elemental analysis. Secondary electrons that are generated within the sample are collected to form images with topological features, whereas backscattered electrons (BSE) that originate from the electron column and are rebounded from the first few layers of the specimen provide compositional contrast that provides insight into variations in bone structure and mineral content, where highly mineralized areas appear brighter. The composition can be further characterized by energy-dispersive X-ray spectroscopy (EDS), whereby the interaction of the electron beam within the sample releases characteristic X-rays that are detected and can be quantified.

A critical SEM-based technique, quantitative backscattered electron (q-BSE) imaging has become a hallmark for evaluating bone structure and bone–implant contact on the micron level, providing chemical information that can aid in robust estimates of bone quality. q-BSE relies on interactions of the primary electron beam with the sample. The quantity of BSE that escape the sample, and therefore the signal intensity, increases upon interaction of the primary electron beam with higher atomic number (Z) elements, resulting in images capturing Z-contrast.[27] If the SEM is calibrated to standards, the intensity of the peaks can be related to the concentration of each element that interacts with the beam.[27] More recently, the technique continues to prove valuable in the assessment of pathological conditions in bone, including investigations of osteoporosis,[28] and rheumatoid disorders.[29] Although SEM has several advantages including relatively high resolution (∼1 nm),

compositional contrast, and ability for elemental analysis, it is limited in dimensionality, that is, it is a 2D imaging approach.

Microcomputed tomography (micro-CT) is a nondestructive method of three-dimensional (3D) imaging that can be used to evaluate the overall bone growth around biomaterials, or bone itself. With a slightly lower resolution than SEM, micro-CT offers the primary advantage of 3D imaging. The sample is generally rotated around 360° or 180° and X-ray micrographs are recorded at each angle, such that mathematical algorithms can be applied to these images to produce an accurate 3D representation of the sample volume. Micro-CT is made possible by the attenuation of the X-rays changing as it passes through the sample, with beam intensity decreasing depending on the composition of the sample through which it interacts.[30] Advanced data processing and visualization pipelines allow for specific volume rendering and segmentation, which ultimately aids in the quantification of the materials of interest, for example, surface area and pore volume measurements. In addition to imaging, X-ray based approaches that probe structural or chemical information can be combined with tomography at synchrotron sources that are well-equipped for multiple experiments, such as small-angle X-ray scattering (SAXS), and X-ray fluorescence (XRF). However, it is important to note that these analyses may produce large data sets, which present challenges for storage and processing. These techniques will not be discussed here in detail, but other articles provide an introduction to the techniques and their applications in bone and biomaterials.[31,32] In the context of biomaterials, the features typically investigated by micro-CT are usually macro-scale porosity,[33] quantification of bone growth around and into ex vivo implants, or calculations of metrics to evaluate osseointegration, such as either the percent bone area or bone–implant contact.[34,35] Structural X-ray techniques are usually reserved for evaluating the mineral components of bone, such as orientation of osteons and collagen fibrils.[36]

Focused ion beam (FIB) tomography, sometimes referred to as FIB-SEM tomography, is a high-resolution destructive 3D imaging technique used to evaluate materials with the resolving power similar to SEM. A FIB microscope is a dual-beam microscope that combines the electron column of a SEM, with an ionized beam, such as gallium or xenon, that can be used for several functions, including the site-specific milling and deposition of material inside the microscope. FIB tomography relies on the use of a line-of-site process in which a sample is cut using a stream of ionized atoms, which act similar to a nanoscale sandblaster, to precisely mill away a block face. The milled surface is then sequentially imaged using the electron beam to create a number of serial images throughout the volume of the specimen, which are then reconstructed into the 3D volume of the material.[37]

Although used extensively in the microelectronics industry, the use of FIB in the biological domain is finally gaining acceptance, in part due to demonstration of the technique to limit beam-induced damage,[38] and several comprehensive reports which highlight its use in biological imaging.[39,40] The technique has been used in both biomineralization and biomaterials research, for example to probe the bone ingrowth into commercial dental implants,[41] and to track the osteocyte network in bone (featured in more detail in the following section).[42]

More recently, FIB tomography has received renewed interest for uncovering some of the microstructural features of lamellar bone. For example, Reznikov et al. have used the

D

Review
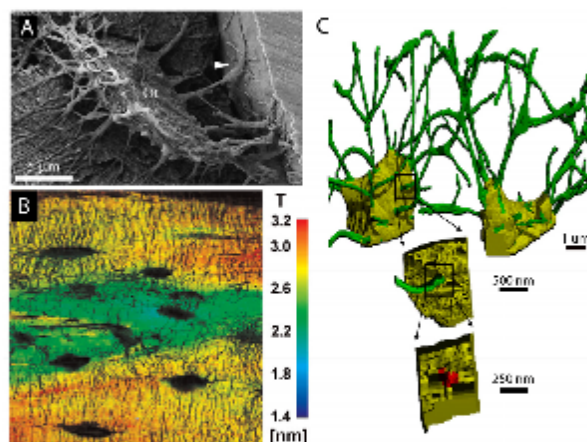
Figure 3. The osteocyte at the microscale. Various approaches are applied to visualize the lacuna-canalicular network (LCN). (A) Novel resin cast etching technique and SEM imaging of an isolated osteocyte (OT) with arrow pointing to canalicular attachment directly to an implant surface, suggests osteocytes contribute to successful osseointegration. (B) SAXS measurements of bone mineral particle thickness (T-parameter maps) overlaid on the osteocyte network demonstrate the variation in mineral thickness around osteocytes. (C) Using FIB tomography, a 3D rendering of the LCN highlights the spatial relationship between the osteocyte lacunae (yellow) and canaliculi (green) in a mouse femur. Reproduced with permission from refs 42, 50, and 54. Copyright 2011, 2016, and 2013 Elsevier.

approach widely to investigate the 3D volume of lamellar rat bone,[43] and human bone[10,44] in great detail. These studies, that encompass data sets of several microns cubed, with nanometer resolution, set the bar for FIB investigations of minerals and biomaterials by FIB tomography. It is important to note however that this work has been performed on demineralized specimens. Real interest exists in moving toward investigating less-manipulated bone models, i.e., materials that have not undergone chemical altering methods such as preservation, demineralization, dehydration, or freeze–thaw cycles that may damage architectures.

Visualizing the Osteocyte Network: A Complementary Approach. As with any intricate material, imaging hierarchical details cannot be achieved by a sole technique, thus requiring a complementary set of characterization approaches to be applied. When characterizing bone, the cellular components on the micron scale are clearly also of interest, in particular the osteocytes of bone which are responsible for maintaining its dynamic turn over process, bone quality, strength and integrity.[45] Once osteoblasts fulfill their role in laying down new bone matrix, they become embedded in the tissue and terminally differentiate into osteocytes.[46] Osteocytes are responsible for the mechanotransduction and signaling in bone to initiate remodeling in the case of microfractures and other defects in bone structure.[1,45,46] The orientation of apatite mineral in bone, which contributes to its overall strength and resilience, is also dependent on the orientation of osteocyte lacunae.[47] Therefore, osteocytes have been studied widely, and are good candidates to exemplify multiple micron-scale characterization approaches.

Osteocytes have also been postulated to play a significant role in osseointegration, as direct connections between osteocytes and implant surfaces have been documented both by transmission electron microscopy (TEM) and a novel resin cast etching SEM approach.[48–50] For instance, a lack of

osteocyte maturity within porous titanium implants relative to native bone was reported by Shah et al. using novel resin cast etching SEM, which suggests that nearing porous implant features bone is remodeling differently (Figure 3A).[50] Ultimately, clear visualization of these networks is integral to understanding bone remodeling at biomaterials surfaces.

The osteocyte network or lacuna-canalicular network (LCN) includes the sites that osteocytes occupy, lacunae, and their connections throughout bone, canaliculi. The LCN is a unique feature of bone that illustrates how a variety of microscale analyses that we discussed above can be employed to investigate its architecture, some of which are highlighted in Figure 3.

Prior to work presented by Schneider et al., Figure 3C, the LCN had never been characterized in 3D, arguably because of a lack of sophisticated sample preparation methods for high-resolution tomography such as FIB-SEM serial sectioning.[42] In this work, Schneider et al. imaged the LCN in 3D using FIB-SEM tomography, and after formidable data reconstructions final renderings yielded resolution in the order 30 nm providing authors with reconstructions that could aid in determining LCN morphometry, clearly identifying the connectivity between the osteocyte lacuna and the canaliculi.[42]

Pacureanu et al., have further demonstrated the value of imaging the LCN in 3D through work applying synchrotron radiation tomography, where a monochromatic X-ray beam is passed through the sample with much higher photonic flux than traditional micro-CT.[51] Resulting images have high levels of noise, making it challenging to image cell dendrites and therefore gain information regarding bone quality.[51] These authors have shown proof of concept that their tomography data has the ability to increase the signal-to-noise ratio of the LCN, and successfully image cell dendrites. An overview of relevant approaches to characterize the LCN by 3D methods is well-reviewed elsewhere.[52]

E

Moreover, additional synchrotron source X-ray analyses, such as microtomography and small-angle X-ray scattering (SAXS) present many advantages for the analysis of bone mineral, particularly the LCN by simultaneously providing images or 3D structure with elemental or crystallographic information, as seen in Figure 3B. Similarly to SEM, during SAXS acquisition of mineralized tissues, a focused X-ray beam is rastered over the material, but instead of collecting electron information, diffraction patterns are detected. Throughout this process the tissue is rotated by various angles, such that the entire sample can be analyzed.[53]

Studies with SAXS, such as one completed by Kerschnitzki et al., have shown that mineral platelets align perpendicular to osteocytes, and that mineral particle thickness varies in the vicinity of osteocytes, after intense postprocessing of the data is completed.[54] The authors demonstrated how bone architecture is related to bone quality, and successfully showed that more organized bone has smaller mineral particles nearing the osteocyte network (Figure 3B), meanwhile, less organized bone has larger, more disorganized particles nearing these features, not shown.[54] This work is further evidence of the importance of osteocyte networks in governing bone quality, and the use of correlative imaging methods to assess these cellular features in 3D.

4. AT THE NANO AND ATOMIC SCALE

Transmission Electron Microscopy. The mineralization and osseointegration landscape has been dominated by observations with light-based methods such as histology and histomorphometry, and lower resolution SEM imaging. However, to move toward an understanding of collagen-mineral interactions we need to move toward nanoscale and atomic characterizations, where TEM plays a key role. A plethora of observations that have laid foundations for understanding osseointegration of various biomaterials have been made using TEM in the 1990s.[55−58] The premise of TEM imaging relies on electrons passing through an electron transparent specimen. Once the beam is transmitted, both inelastic and elastic scattering events can be detected, and be used for imaging and elemental analysis. Traditional methods of TEM imaging include bright field (BF) and dark field (DF) imaging, relying on the collection of transmitted, and diffracted electrons, respectively. More recently, the use of scanning TEM (STEM) and high angle annular dark-field (HAADF) detectors has enabled better compositional contrast in bone imaging.[59] In this imaging mode, image intensity is roughly proportional to Z^2 (atomic number squared). This enables differentiation between mineral and organic components, and sufficient contrast of collagen fibrils without staining. The presence of nanocrystallinity in bone means that DF images can be used to identify mineral platelet orientation, and selected area electron diffraction patterns can also be used to gain information on texture. An added benefit of TEM is also its coupled spectral analyses: energy-dispersive X-ray spectroscopy (EDS) and electron energy loss spectroscopy (EELS) which detect characteristic X-rays or measure characteristic energy losses to determine chemical composition. An important consideration when moving toward higher resolution analyses, such as TEM, is the sample preparation of tissues and specimens. Historically, specimens have been prepared by slicing thin sections with a diamond blade, a process called ultramicrotomy.

The advantages of using another technique, called focused ion beam (FIB), as a method to maintain interfacial integrity

between bone components, and at bone−implant interfaces or in biological systems has been clearly demonstrated in recent years.[39,40] The site-specific approach allows for isolation of a region of interest several microns wide for bombardment with gallium ions, extraction by an in situ micromanipulator or ex situ method, and placement on a TEM grid for further work. These specimens are typically a maximum of 300 nm thick, allowing for electron transparency with minimal physical damage to the sample. The benefits of using this approach as compared to ultramicrotomy are widely demonstrated in ivory,[60] fluorapatite−gelatin composites,[61] tooth,[62] biomaterial−cell interfaces,[63,64] and bone−implant interfaces.[65] Schwarcz et al. have used ion milling to suggest their new model for the ultrastructure of bone, highlighting the importance that subsequent studies to support or refute this ultrastructure should be done using similar sample preparation methods.[66] FIB techniques are also advantageous for both organic and soft tissues, as the precise milling technique minimizes damage to soft tissues,[39] and can also be considered for cryogenic TEM lamellar preparation as shown for microorganisms,[67] as the interest in maintaining the native state of biological tissues remains a challenge during conventional TEM.

Utilizing ion milling or focused ion beam milling new observations supporting an increase an abundance of extrafibrillar mineral in bone have been made by Schwarcz and colleagues with TEM.[66,68] Their model of bone is presented in our hierarchical view of bone in Figure 1. Other studies have also suggested, although to a lesser extent, the presence of higher amounts of extrafibrillar mineral[69] than originally suggested by the first ultrastructural models of bone that place most of bone mineral within the gap zone of collagen fibrils.[70,71] Biomechanical simulations of bone strength, stiffness, and finite element modeling experiments,[72] have also indicated a higher likelihood that the majority of mineral is located exterior to the collagen fibrils, as in Schwarcz et al.'s model.[73]

Electron Tomography. Although many imaging techniques can be used to evaluate the bone−implant interface, an optimal approach may be using correlative imaging platforms to provide a holistic view of the mineralized tissue or bone−implant interface. Such advanced platforms include the use of multilength scale and multidimensional imaging techniques that can describe bone−implant contact on the multiple hierarchical levels that relate to bone structure.[3]

The use of TEM to resolve collagen−mineral interactions has been highlighted above, yet this yields two-dimensional images of distinctly three-dimensional objects. Electron tomography allows the visualization of samples in three dimensions, providing insight into the orientation and connectivity at biointerfaces. This involves taking multiple projection images at various tilt angles, followed by the alignment and reconstruction of the images to yield a 3D volume. The basics of electron tomography are covered in detail elsewhere,[74,75] including comprehensive reviews on electron tomography for applications in soft materials and biomaterials.[76,77] In general, electron tomography uses an approach that is quite similar to that employed in micro-CT. In both cases, projection images that are a monotonic function of the sample are acquired around the specimen, and then reconstructions are performed using mathematical algorithms. The resulting information is a 3D volume that can be sliced through in the Z-direction or visualized in 3D. Besides of course the obvious difference in source (electrons versus X-rays), the main difference between

the two techniques is final resolution, which is dependent on the source. Electron tomograms can be obtained down to even atomic-scale resolution,[78] whereas the resolution of X-ray tomography depends on the source, with synchrotron sources approaching a few nanometers, and lab-bench versions hovering around the microscale.

While electron tomography has had foundations in bone ultrastructural observations, the first pioneering works in this area utilized either bright-field or high voltage tomography.[79−81] Newer approaches to electron tomography, specifically a form that uses high-angle annular dark-field (HAADF) images to gain compositional contrast, have been demonstrated to support claims of new ultrastructural models of bone,[82] understand the orientation of bone adjacent to osteocyte lacunae,[49] and to understand the orientation of collagen fibrils and interfacial connections at biomaterial interfaces, such as hydroxyapatite−bone,[65] titanium−bone,[18,34,83] and dental cement−dentin interfaces.[84]

New developments in electron tomography are related to increasing the accuracy of reconstructions to allow more quantitative understanding of interfaces, for example, by reducing artifacts from the missing-wedge by moving to a 180° rotation tomography, called on-axis electron tomography. This approach was demonstrated by us to show clear morphological features of nanoroughened titanium oxide integrating with human bone.[6] Other emerging directions include simultaneous electron tomography and elemental analyses to offer information on chemical signals. One such approach is EDS tomography, the developments of which and remaining challenges are highlighted for nanoparticle systems.[85] This technique collects EDS maps at each imaging step during tomography acquisition, which can then be reconstructed similarly to images to gain a 3D compositional map. A similar approach using electron energy loss spectroscopy (EELS) tomography been demonstrated on bone−implant interfaces, where the chemical signatures assist in the differentiation of collagen and mineral phases,[86] where EELS detects the energy lost from inelastically scattered electrons that are characteristic to each element.

Atom Probe Tomography. Shifting to yet smaller length scales, atom probe tomography (APT) offers extensive capabilities for high-resolution imaging at the atomic scale with a spatial resolution of sub-0.3 nm, while simultaneously revealing chemical information achieving a sensitivity of 1 ppm.[87] The fundamentals of APT rely on successive field evaporation of atoms as ions from the specimen surface by an applied high voltage field or a pulsating laser. The use of electric field is primarily employed for samples of high electrical conductivity; meanwhile, the pulsating laser enables field evaporation of nonconductive materials. The evaporated ions are detected laterally (x,y) by a position-sensitive detector, and due to the nature of the pulsating laser, the exact atom evaporation and time-of-flight can be detected for each atom. The combination of these parameters yields the exact z-coordinate of each atom and respective mass-to-charge (m/z) ratio.[87]

While a technique initially thought to be reserved for conductive and nonbiological samples, a plethora of applications for APT are arising in biology and biological materials. For example, chemical mapping of mammalian HeLa cells by APT has been demonstrated,[88] as well three-dimensional reconstructions of ferritin,[89] chiton,[90] and a host of other biominerals including various apatites,[91] and enamel.[92−94]

Recently, we presented the first APT of human bone, which highlights the distribution of trace elements, such as sodium, within the organic regions of bone, and at organic−inorganic interfaces, not otherwise detectable with electron-based analytical approaches.[5] Featured in Figure 4A, our research demonstrated the potential APT has in advancing the scientific understand of bone structure and interphases within mineralized tissues, which could provide insight into natural biomineralization processes on the atomic scale.
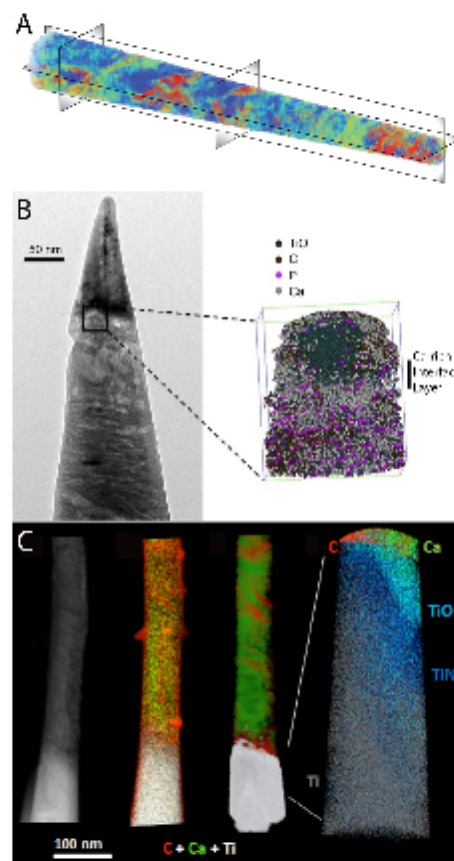
Figure 4. Atom probe tomography of mineralized tissues and osseointegrated interfaces. (A) 3D volume map shows the gradients of Ca distribution throughout human bone, where blue represents a lack of Ca and red represents high concentrations of Ca atoms. (B) Bright-field TEM micrograph and 3D APT atom map shows the likely presence of an inorganic interface between human bone and a retrieved dental implant. (C) Similar dental implant and human bone interface analyzed by a correlative combination of electron tomography, EELS tomography, and APT highlights the integration of Ca atoms into the surface oxide of laser-modified titanium implants. Reproduced with permission from refs 5, 86, and 96. Copyright 2017 Nature Publishing Group, 2015 Cambridge University Press, and 2017 Elsevier.
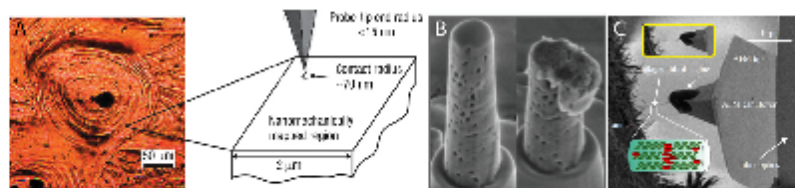
Figure 5. Imaging-based nanomechanical testing approaches for bonelike materials. (A) Optical microscopy image of an individual osteon and the AFM-based nanoindentation schematic used to infer energy dissipation through nanoscale structural heterogeneity, outlining the principal methods employed by Tai et al. (B) In another approach, nanopillars fabricated in FIB were placed under uniaxial compression to determine properties of distinct ordered/disordered zones within bone. (C) SEM image of the AFM configuration to evaluate the tensile properties of an individual antler collagen fiber with a combined AFM/SEM instrument. Reproduced with permission from refs 101, 107, and 109. Copyright 2007 Nature Publishing Group, 2016 Nature Publishing Group, and 2011 Royal Society of Chemistry.

APT has also been applied to osseointegrated materials and the interface between bone and biomaterials, for example mesoporous titania and rat bone[95] or human bone,[96] and laser-modified titanium and human bone.[86] Sundell et al. used APT to investigate human bone–implant interfaces, where the resolving power of the technique provided insight into the rich calcium layer found at the bone–implant interface.[96] Meanwhile, we have further demonstrated the value of complementary techniques, where we have evaluated a retrieved osseointegrated implant and characterized it using both on-axis electron tomography and APT, providing a holistic view on the functional connection between bone and titanium from both structural and chemical perspectives.[6] These two studies featured in Figure 4B, C, represent the first move toward a truly atomic scale chemical investigation of bone to implant interfaces.

Mechanical Testing at the Nanoscale. The mechanical properties of mineralized tissues and interfaces have often been attributed to their whole bone hierarchical architecture.[97–100] Recent technological advances in mechanical testing and modeling methods have resulted in a trend toward nanoscale investigations of bone mechanical properties, both experimentally with atomic force microscopy (AFM)-nanoindentation,[101,102] and by simulations with finite element modeling,[73] molecular dynamics, or full atomistic models.[103,104] Some of these experimental approaches that probe nano level architectures of bone mineral or collagen fibrils, and incorporate image-based methods, are shown in Figure 5.

First, experiments by Tai et al, exemplify the use of AFM for both imaging and nanomechanical strength determination of bone.[101] AFM, a high-resolution technique, uses a sharpened probe that either traces the surface at a defined height or mechanically interacts with the surface in contact mode. By probing the surface mechanically and measuring both the force exerted back onto the tip and the displacement, AFM-based nanoindentation can accurately determine nanomaterials properties.[105] Using this approach, the stiffness of bone has been reported ranging between 2 to 30 GPa. This variable range is notable, as bone has natural interphases that could be related to increased calcium mineral and therefore increased stiffness.[101] AFM-based nanoindentation is therefore useful for probing local nanoscale properties in heterogeneous tissues.

Moreover, micro or nanopillars ranging in diameter from 250 to 3000 nm can be extracted from regions in bone using FIB for site-specific nanocompression testing.[106] Tertuliano et al. showed that pillars from distinct regions of bone structure (ordered, and disordered) performed similarly under mechan-ical loading at both micro and nano length scales, which was possible through the use of a nanoindenter equipped with a flat plate. As noted in Figure 5B, experiments were completed until failure, and the fracture mechanism was then deduced to be brittle or shearing (not shown).[107] Interestingly, similar failure mechanisms and rates were observed among the various length scales investigated; however, the authors postulated that the overall porosity of the extracellular matrix was the key determining factor for mechanical strength.[107]

At even smaller length scales, at the level of individual collagen fibrils, the role of mineralization on mechanical strength has been evaluated and modeled in situ using a microelectromechanical device coupled to a confocal Raman microscope on synthetic collagen/apatite composites.[108] This work has shown the potential importance of degree of mineralization on strength of bone, where specimens with increased apatite composition showed higher elastic moduli, a mechanism suggested to be based on the molecular interlocking of collagen fibrils mediated by the mineral phase.[108]

Combined AFM and SEM imaging has also shed light on the effect of mineralization on mechanical properties of collagen fibrils in bone-like antler tissue, where similar mineral content had a homogeneous effect on initial tensile strength.[109] These experiments used a more sophisticated approach, combing SEM and AFM, by which one single collagen fibril could be attached to the AFM probe and slowly pulled until fracture, Figure 5C.[109] Merging these two methods allowed the authors to perform an accurate investigation of single collagen fibrils, emphasizing the importance of developing unique characterization methods to solve biomaterials problems. Furthermore, atomistic calculations are also broadening the scope of mechanical influences in bone structure toward the collagen fibril unit, where the role of mineral in strengthening bone has been further supported.[104]

5. IN REAL TIME

In Situ Mineralization. The characterization of established biominerals and interfaces is of interest, but increasingly, there is a scientific desire to visualize the formation of tissues, or their mineral components, in real-time, hydrated environments. Biomineral growth is well-known to be templated by proteins such as collagen, and noncollagenous proteins in various biomineral systems,[110] such as bone,[111] periodontal tissues,[112] and invertebrate systems.[113,114] Conventional observations of biomineralization processes have relied on halting mineralization at defined time points, either cryogenically or by chemical processes. Much progress has been made in understanding the
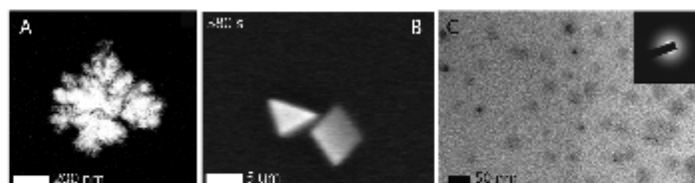
Figure 6. Real-time in situ biomineralization. (A) Liquid-phase scanning-TEM images show the formation of internal branching structures in CaCO$_3$ in the presence of AP7, a nacre C-RING protein. (B) Inverted atmospheric SEM allowed for observation of growth of CaCO$_3$ with triangular habit in the absence of any additives of under atmospheric conditions. (C) Amorphous Ca-PSS globules formed in liquid phase TEM with inset diffraction pattern confirming their amorphous structure. Reproduced with permission from ref 118, 119, and 127. Copyright 2013 Elsevier, 2015 Nature Publishing Group, and 2015 American Association for the Advancement of Science.

role of collagen, noncollagenous proteins, and polyaspartic acid in the mineralization of collagen, in this way, presented in detail in other reviews and recent works.[115–117]

However, the dynamic processes of crystal growth are of interest to further understand the mechanisms behind biomineralization. Considerable progress has been made toward understanding the in situ growth of model systems, such as calcium carbonate for example, by an approach called liquid phase or in situ transmission electron microscopy.[118–121] This approach relies on the use of a specialized TEM holder that encapsulates liquid between electron-transparent silicon nitride or graphene membranes, enabling liquid to be safely placed within the vacuum of a TEM.[122] Several approaches to liquid cell TEM for the investigation of biominerals are available, including the simple encapsulation of liquid in static conditions, to the flow of liquid via an inlet and outlet,[123] or even mixing of different fluids within the TEM field of view.[124] This approach allows the real-time observation of mineral nanoparticle growth, and the interaction of relevant liquid systems or molecules on their growth mechanism. Optimization of experimental approaches to improve resolution, as well as the elucidation and elimination of electron beam-liquid interactions, and the development of approaches for quickly acquiring and processing data remain key challenges.[125,126]

Investigation into the role of proteins and inorganic additives has been a central theme for real-time in situ observations of biomineralization, a variety of which are highlighted in Figure 6. In these examples, the role of proteins or organic molecules on minerlization delay and resulting mineral assembly were investigated. Using a liquid flow TEM cell, the nacre-like calcium carbonate system was investigated to show that the intracrystalline C-RING protein AP7 delays the onset of nucleation and changes the spatial assembly of mineralized particles.[127] Other organic molecules such as poly(acrylic acid) (PAA) and poly(styrenesulfonate-co-maleic acid) (PSS-MA) have been shown to similarly contribute to the formation of a transient mineral phase, and ultimately morphologial changes in mineral formation of CaCO$_3$ as observed under atmospheric conditions in a unique inverted SEM instrument.[118] Polystyrenesulfonate (PSS) has also been shown to inhibit the nucleation of a transition phase of amorphous calcium carbonate during in situ TEM observations.[119] These observations provide insight into the role of mediating proteins and molecules during biomineralization and were only enabled by the encapsultated liquid cells or novel SEM assembly.

Moving toward more bonelike minerals systems, we have demonstrated the precipitation of hydroxyapatite-like calcium phosphates in static liquid cell TEM conditions.[128] This may provide insights into the morphological and crystal transitions that bonelike hydroxyapatite minerals undergo during bone formation. Further work to investigate the mineral phase interacting with its counterpart collagen through the real-time mineralization of collagen fibrils in solution is of key interest to the understanding of bone mineralization in healthy and pathological states. In addition, elucidating and reducing the role of the electron beam on the formation of biomineralized structures is highly relevant, as bone mineral content has been shown to be easily altered by repeated or high energy exposure to electron beams.[129]

Of course the experiments carried out in liquid cell TEM systems represent simplified in vitro models for in vivo mineralization. The other approach to mimicking an in vivo environment and mineralization is with relevant cell culture systems, which will not be discussed here, but is well-covered in recent works and other reviews.[130–133]

Clinical Evaluation of Osseointegration. Visualization of the mechanisms of bone growth and attachment in real-time on the nanoscale level, as described above, are simply not possible in clinical or in vivo models. In these scenarios, approaches to quantifying or qualifying osseointegration in patients rely on measures of mechanical implant stability, for example using quantitative ultrasound techniques,[134] and lower resolution nondestructive imaging techniques, such a radiography,[135] computed tomography (CT),[136] and magnetic resonance imaging (MRI).[137] Similar to high-resolution lab-based imaging, clinical imaging has experienced a shift in emphasis from two-dimensional to three-dimensional imaging modalities, where technological advances in cone beam computed tomography (CBCT) are opening up a new realm of imaging possibilities for implant planning and evaluation due to lower beam dose compared to conventional CT. However, review studies report inconsistencies in radiation dose values,[138] and recommendations advise its sparing use, predominantly for surgical planning, and not as an evaluation tool.[139] Methods for assessing bone quality, independent of bone implants, are similarly varied between noninvasive imaging techniques and complementary ex vivo studies, which are well-detailed elsewhere.[140]

6. CONCLUSIONS

Technological advancements across the fields of ion, electron, X-ray, and atom probe microscopies are resulting in an increase in the use of multiscale and multidimensional analyses for the investigation of bone interphases and biomaterials interfaces. A clear interest in moving toward multidimensional techniques that capture not only three-dimensional but also relevant

| Review

chemical signatures is now emerging. Progress toward capturing real-time mineralization events using in situ liquid phase electron microscopy is another technological breakthrough, and paving the way for further mechanistic observations in vitro. With continuous developments in the imaging and characterization landscape, we expect our view of biomineralized tissues, such as bone, and the complexity of their interphases, including those to biomaterials, to continue to evolve.

■ AUTHOR INFORMATION

Corresponding Author
*E-mail: kgrandfield@mcmaster.ca.

ORCID
Kathryn Grandfield: 0000-0002-0188-9580

Notes
The authors declare no competing financial interest.

■ ACKNOWLEDGMENTS

■ REFERENCES

(1) Bonewald, L. F. Mechanosensation and Transduction in Osteocytes. *Bonekey Osteovision* 2006, 3 (10), 7–15.
(2) Weiner, S.; Traub, W. Bone structure: from angstroms to microns. *FASEB J.* 1992, 6 (3), 879–885.
(3) Grandfield, K. Bone, implants, and their interfaces. *Phys. Today* 2015, 68 (4), 40–45.
(4) Ho, S. P.; Balooch, M.; Marshall, S. J.; Marshall, G. W. Local properties of a functionally graded interphase between cementum and dentin. *J. Biomed. Mater. Res.* 2004, 70A (3), 480–489.
(5) Langelier, B.; Wang, X.; Grandfield, K. Atomic scale chemical tomography of human bone. *Sci. Rep.* 2017, 7, 39958.
(6) Wang, X.; Shah, F. A.; Palmquist, A.; Grandfield, K. 3D Characterization of Human Nano-osseointegration by On-Axis Electron Tomography without the Missing Wedge. *ACS Biomater. Sci. Eng.* 2017, 3 (1), 49–55.
(7) Brown, W. E.; Chow, L. C. Chemical Properties of Bone Mineral. *Annu. Rev. Mater. Sci.* 1976, 6 (1), 213–236.
(8) Wegst, U. G. K.; Bai, H.; Saiz, E.; Tomsia, A. P.; Ritchie, R. O. Bioinspired structural materials. *Nat. Mater.* 2014, 14 (1), 23–36.
(9) Ritchie, R. O.; Buehler, M. J.; Hansma, P. Plasticity and toughness in bone. *Phys. Today* 2009, 62, 41.
(10) Reznikov, N.; Shahar, R.; Weiner, S. Bone hierarchical structure in three dimensions. *Acta Biomater.* 2014, 10 (9), 3815–3826.
(11) Li, H.; Ghazanfari, R.; Zacharaki, D.; Lim, H. C.; Scheding, S. Isolation and characterization of primary bone marrow mesenchymal stromal cells. *Ann. N. Y. Acad. Sci.* 2016, 1370 (1), 109–118.
(12) Florencio-Silva, R.; Sasso, G. R. d. S.; Sasso-Cerri, E.; Simões, M. J.; Cerri, P. S. Biology of Bone Tissue: Structure, Function, and Factors That Influence Bone Cells. *BioMed Res. Int.* 2015, 2015, 1–17.
(13) Hadjidakis, D. J.; Androulakis, I. I. Bone remodeling. *Ann. N. Y. Acad. Sci.* 2006, 1092, 385–396.
(14) Reznikov, N.; Chase, H.; Brumfeld, V.; Shahar, R.; Weiner, S. The 3D structure of the collagen fibril network in human trabecular bone: Relation to trabecular organization. *Bone* 2015, 71, 189–195.
(15) Brånemark, P. I. Osseointegration and its experimental background. *J. Prosthet. Dent.* 1983, 50 (3), 399–410.

(16) Saini, M.; Singh, Y.; Arora, P.; Arora, V.; Jain, K. Implant biomaterials: A comprehensive review. *World J. Clin. Cases* 2015, 3 (1), 52–57.
(17) Long, M.; Rack, H. J. Titanium alloys in total joint replacement? a materials science perspective. *Biomaterials* 1998, 19 (18), 1621–1639.
(18) Palmquist, A.; Grandfield, K.; Norlindh, B. Bone-titanium oxide interface in humans revealed by transmission electron microscopy and electron tomography. *J. R. Soc., Interface* 2012, 9 (67), 396–400.
(19) Roberts, T. T.; Rosenbaum, A. J. Bone grafts, bone substitutes and orthobiologics: the bridge between basic science and clinical advancements in fracture healing. *Organogenesis* 2012, 8 (4), 114.
(20) Sterling, J. A.; Guelcher, S. A. Biomaterial scaffolds for treating osteoporotic bone. *Curr. Osteoporos. Rep.* 2014, 12 (1), 48–54.
(21) McKee, M. D.; Pedraza, C. E.; Kaartinen, M. T. Osteopontin and Wound Healing in Bone. *Cells Tissues Organs* 2011, 194 (2–4), 313.
(22) Teo, A. J. T.; Mishra, A.; Park, I.; Kim, Y.-J.; Park, W.-T.; Yoon, Y.-J. Polymeric Biomaterials for Medical Implants and Devices. *ACS Biomater. Sci. Eng.* 2016, 2 (4), 454–472.
(23) Niinomi, M.; Nakai, M. Titanium-Based Biomaterials for Preventing Stress Shielding between Implant Devices and Bone. *Int. J. Biomater.* 2011, 2011, 1–10.
(24) Lindahl, H. Epidemiology of periprosthetic femur fracture around a total hip arthroplasty. *Injury* 2007, 38 (6), 651–654.
(25) Bordier, P. J.; Chot, S. T. Quantitative histology of metabolic bone disease. *Clin. Endocrinol. Metab.* 1972, 1 (1), 197–215.
(26) Bobyn, J. D.; Pillar, R. M.; Cameron, H. U.; Weatherly, G. C. The Optimum Pore Size for the Fixation of Porous-Surfaced Metal Implants by the Ingrowth of Bone. *Clin. Orthop. Relat. Res.* 1980, 150, 263–270.
(27) Roschger, P.; Fratzl, P.; Eschberger, J.; Klaushofer, K. Validation of quantitative backscattered electron imaging for the measurement of mineral density distribution in human bone biopsies. *Bone* 1998, 23 (4), 319–326.
(28) Roschger, P.; Misof, B.; Paschalis, E.; Fratzl, P.; Klaushofer, K. Changes in the Degree of Mineralization with Osteoporosis and its Treatment. *Curr. Osteoporos. Rep.* 2014, 12 (3), 338–350.
(29) Harrington, J.; Holmyard, D.; Silverman, E.; Sochett, E.; Grynpas, M. Bone histomorphometric changes in children with rheumatic disorders on chronic glucocorticoids. *Pediatric Rheumatology Online J.* 2016, 14 (1), 50–58.
(30) Boerckel, J. D.; Mason, D. E.; McDermott, A. M.; Alsberg, E. Microcomputed tomography: approaches and applications in bioengineering. *Stem Cell Res. Ther.* 2014, 5 (6), 144.
(31) Georgiadis, M.; Müller, R.; Schneider, P. Techniques to assess bone ultrastructure organization: orientation and arrangement of mineralized collagen fibrils. *J. R. Soc., Interface* 2016, 13 (119), 20160088.
(32) Granke, M.; Gourrier, A.; Rupin, F.; Raum, K.; Peyrin, F.; Burghammer, M.; Saïed, A.; Laugier, P. Microfibril Orientation Dominates the Microelastic Properties of Human Bone Tissue at the Lamellar Length Scale. *PLoS One* 2013, 8 (3), e58043.
(33) Bertoldi, S.; Farè, S.; Tanzi, M. C. Assessment of scaffold porosity: the new route of micro-CT. *J. Appl. Biomater. Biomech.* 2011, 9 (3), 165–175.
(34) Thorfve, A.; Palmquist, A.; Grandfield, K. Three-dimensional analytical techniques for evaluation of osseointegrated titanium implants. *Mater. Sci. Technol.* 2015, 31 (2), 174–179.
(35) Otsuki, B.; Takemoto, M.; Fujibayashi, S.; Neo, M.; Kokubo, T.; Nakamura, T. Pore throat size and connectivity determine bone and tissue ingrowth into porous implants: Three-dimensional micro-CT based structural analyses of porous bioactive titanium implants. *Biomaterials* 2006, 27 (35), 5892–5900.
(36) Varga, P.; Pacureanu, A.; Langer, M.; Suhonen, H.; Hesse, B.; Grimal, Q.; Cloetens, P.; Raum, K.; Peyrin, P. Investigation of the three-dimensional orientation of mineralized collagen fibrils in human lamellar bone using synchrotron X-ray phase nano-tomography. *Acta Biomater.* 2013, 9 (9), 8118–8127.

ACS Biomaterials Science & Engineering

(37) Mobus, G.; Inkson, B. J. Nanoscale tomography in materials science. *Mater. Today* 2007, 10 (12), 18–25.
(38) Giannuzzi, L.; Geurts, R.; Ringnalda, J. 2 keV Ga+ FIB Milling for Reducing Amorphous Damage in Silicon. *Microsc. Microanal.* 2005, 11 (S02), 828–829.
(39) Narayan, K.; Subramaniam, S. Focused ion beams in biology. *Nat. Methods* 2015, 12 (11), 1021–1031.
(40) Grandfield, K.; Engqvist, H. Focused Ion Beam in the Study of Biomaterials and Biological Matter. *Adv. Mater. Sci. Eng.* 2012, 2012, 1–6.
(41) Giannuzzi, L.; Phifer, D.; Giannuzzi, N.; Capuano, M. Two-Dimensional and 3-Dimensional Analysis of Bone/Dental Implant Interfaces With the Use of Focused Ion Beam and Electron Microscopy. *J. Oral Maxillofac. Surg.* 2007, 65 (4), 737–747.
(42) Schneider, P.; Meier, M.; Wepf, R.; Müller, R. Serial FIB/SEM imaging for quantitative 3D assessment of the osteocyte lacuno-canalicular network. *Bone* 2011, 49 (2), 304–311.
(43) Reznikov, N.; Almany-Magal, R.; Shahar, R.; Weiner, S. Three-dimensional imaging of collagen fibril organization in rat circumferential lamellar bone using a dual beam electron microscope reveals ordered and disordered sub-lamellar structures. *Bone* 2013, 52 (2), 676–683.
(44) Reznikov, N.; Shahar, R.; Weiner, S. Three-dimensional structure of human lamellar bone: the presence of two different materials and new insights into the hierarchical organization. *Bone* 2014, 59, 93–104.
(45) Rucci, N. Molecular biology of bone remodelling. *Clin. Cases Miner. Bone Metab.* 2008, 5 (1), 49–56.
(46) Dallas, S. L.; Bonewald, L. F. Dynamics of the transition from osteoblast to osteocyte. *Ann. N. Y. Acad. Sci.* 2010, 1192, 437–443.
(47) Shah, F. A.; Zanghellini, E.; Matic, A.; Thomsen, P.; Palmquist, A. The Orientation of Nanoscale Apatite Platelets in Relation to Osteoblastic–Osteocyte Lacunae on Trabecular Bone Surface. *Calcif. Tissue Int.* 2016, 98 (2), 193–205.
(48) Steflik, D. E.; Sisk, A. L.; Parr, G. R.; Lake, F. T.; Hanes, P. J.; Berkery, D. J.; Brewer, P. Transmission electron and high-voltage electron microscopy of osetocyte cellular processes extending to the dental implant surface. *J. Biomed. Mater. Res.* 1994, 28 (9), 1095–1107.
(49) Shah, F. A.; Wang, X.; Thomsen, P.; Grandfield, K.; Palmquist, A. High-Resolution Visualization of the Osteocyte Lacuno-Canalicular Network Juxtaposed to the Surface of Nanotextured Titanium Implants in Human. *ACS Biomater. Sci. Eng.* 2015, 1 (5), 305–313.
(50) Shah, F. A.; Snis, A.; Matic, A.; Thomsen, P.; Palmquist, A. 3D printed Ti6Al4V implant surface promotes bone maturation and retains a higher density of less aged osteocytes at the bone–implant interface. *Acta Biomater.* 2016, 30, 357–367.
(51) Pacureanu, A.; Larrue, A.; Langer, M.; Olivier, C.; Muller, C.; Lafage-Proust, M. H.; Peyrin, F. Adaptive filtering for enhancement of the osteocyte cell network in 3D microtomography images. *IRBM* 2013, 34 (1), 48–52.
(52) Schneider, P.; Meier, M.; Wepf, R.; Müller, R. Towards quantitative 3D imaging of the osteocyte lacuno-canalicular network. *Bone* 2010, 47 (5), 848–858.
(53) Schaff, F.; Bech, M.; Zaslansky, P.; Jud, C.; Liebi, M.; Guizar-Sicairos, M.; Pfeiffer, F. Six-dimensional real and reciprocal space small-angle X-ray scattering tomography. *Nature* 2015, 527 (7578), 353–356.
(54) Kerschnitzki, M.; Kollmannsberger, P.; Burghammer, M.; Duda, G. N.; Weinkamer, R.; Wagermaier, W.; Fratzl, P. Architecture of the osteocyte network correlates with bone material quality. *J. Bone Miner. Res.* 2013, 28 (8), 1837–1845.
(55) Steflik, D. E.; Corpe, R. S.; Lake, F. T.; Young, T. R.; Sisk, A. L.; Parr, G. R.; Hanes, P. J.; Berkery, D. J. Ultrastructural analyses of the attachment (bonding) zone between bone and implanted biomaterials. *J. Biomed. Mater. Res.* 1998, 39 (4), 611–620.
(56) Neo, M.; Kotani, S.; Nakamura, T.; Yamamuro, T.; Ohtsuki, C.; Kokubo, T.; Bando, Y. A comparative study of ultrastructures of the interfaces between four kinds of surface-active ceramic and bone. *J. Biomed. Mater. Res.* 1992, 26 (11), 1419–1432.

(57) de Bruijn, J. D.; van Blitterswijk, C. A.; Davies, J. E. Initial bone matrix formation at the hydroxyapatite interface in vivo. *J. Biomed. Mater. Res.* 1995, 29 (1), 89–99.
(58) Hemmerlé, J.; Onçag, A.; Ertürk, S. Ultrastructural features of the bone response to a plasma-sprayed hydroxyapatite coating in sheep. *J. Biomed. Mater. Res.* 1997, 36 (3), 418–425.
(59) McNally, E.; Nan, F.; Botton, G. A.; Schwarcz, H. P. Scanning transmission electron microscopic tomography of cortical bone using Z-contrast imaging. *Micron* 2013, 49, 46–53.
(60) Jantou, V.; Turmaine, M.; West, G. D.; Horton, M. A.; McComb, D. W. Focused ion beam milling and ultramicrotomy of mineralised ivory dentine for analytical transmission electron microscopy. *Micron* 2009, 40 (4), 495–501.
(61) Volkert, C. A.; Busch, S.; Heiland, B.; Dehm, G. Transmission electron microscopy of fluorapatite-gelatine composite particles prepared using focused ion beam milling. *J. Microsc.* 2004, 214 (3), 208–212.
(62) Coutinho, E.; Jarmar, T.; Svahn, F.; Neves, A. A.; Verlinden, B.; van Meerbeek, B.; Engqvist, H. Ultrastructural characterization of tooth-biomaterial interfaces prepared with broad and focused ion beams. *Dent. Mater.* 2009, 25 (11), 1325–1337.
(63) Engqvist, H.; Svahn, F.; Jarmar, T.; Detsch, R.; Mayr, H.; Thomsen, P.; Ziegler, G. A novel method for producing electron transparent films of interfaces between cells and biomaterials. *J. Mater. Sci.: Mater. Med.* 2008, 19 (1), 467–470.
(64) Jarmar, T.; Palmquist, A.; Brånemark, R.; Hermansson, L.; Engqvist, H.; Thomsen, P. Technique for preparation and characterization in cross-section of oral titanium implant surfaces using focused ion beam and transmission electron microscopy. *J. Biomed. Mater. Res., Part A* 2008, 87A (4), 1003–1009.
(65) Grandfield, K.; McNally, E. A.; Palmquist, A.; Botton, G. A.; Thomsen, P.; Engqvist, H. Visualizing biointerfaces in three dimensions: electron tomography of the bone-hydroxyapatite interface. *J. R. Soc., Interface* 2010, 7 (51), 1497–1501.
(66) McNally, E. A.; Schwarcz, H. P.; Botton, G. A.; Arsenault, A. L. A model for the ultrastructure of bone based on electron microscopy of ion-milled sections. *PLoS One* 2012, 7 (1), e29258.
(67) Rubino, S.; Melin, P.; Spellward, P.; Leifer, K. Cryo-electron microscopy specimen preparation by means of a focused ion beam. *J. Visualized Exp.* 2014, No. 89, e51463–e51463.
(68) Schwarcz, H. P. The ultrastructure of bone as revealed in electron microscopy of ion-milled sections. *Semin. Cell Dev. Biol.* 2015, 46, 44–50.
(69) Alexander, B.; Daulton, T. L.; Genin, G. M.; Lipner, J.; Pasteris, J. D.; Wopenka, B.; Thomopoulos, S. The nanometre-scale physiology of bone: steric modelling and scanning transmission electron microscopy of collagen–mineral structure. *J. R. Soc., Interface* 2012, 9 (73), 1774.
(70) Weiner, S.; Traub, W. Organization of hydroxyapatite crystals within collagen fibrils. *FEBS Lett.* 1986, 206 (2), 262–266.
(71) Weiner, S.; Traub, W. Bone structure: from angstroms to microns. *FASEB J.* 1992, 6 (3), 879–885.
(72) Schwarcz, H. P.; Abueidda, D.; Jasiuk, I. The Ultrastructure of Bone and Its Relevance to Mechanical Properties. *Front. Phys.* 2017, DOI: 10.3389/fphy.2017.00039.
(73) Abueidda, D. W.; Sabet, F. A.; Jasiuk, I. M. Modeling of Stiffness and Strength of Bone at Nanoscale. *J. Biomech. Eng.* 2017, 139, 051006.
(74) Midgley, P. A.; Weyland, M. 3D electron microscopy in the physical sciences: the development of Z-contrast and EFTEM tomography. *Ultramicroscopy* 2003, 96 (3–4), 413–431.
(75) Midgley, P. A.; Dunin-Borkowski, R. E. Electron tomography and holography in materials science. *Nat. Mater.* 2009, 8 (4), 271–280.
(76) Ercius, P.; Alaidi, O.; Rames, M. J.; Ren, G. Electron Tomography: A Three-Dimensional Analytic Tool for Hard and Soft Materials Research. *Adv. Mater.* 2015, 27, 5638.

(77) Grandfield, K.; Palmquist, a.; Engqvist, H. High-resolution three-dimensional probes of biomaterials and their interfaces. *Philos. Trans. R. Soc., A* **2012**, *370*, 1337−1351.

(78) Miao, J.; Ercius, P.; Billinge, S. J. L. Atomic electron tomography: 3D structures without crystals. *Science* **2016**, *353* (6306), aaf2157.

(79) Landis, W. J.; Hodgens, K. J.; Arena, J.; Song, M. J.; McEwen, B. F. Structural relations between collagen and mineral in bone as determined by high voltage electron microscopic tomography. *Microsc. Res. Tech.* **1996**, *33* (2), 192−202.

(80) Landis, W. J.; Song, M. J.; Leith, A.; McEwen, L.; McEwen, B. F. Mineral and Organic Matrix Interaction in Normally Calcifying Tendon Visualized in Three Dimensions by High-Voltage Electron Microscopic Tomography and Graphic Image Reconstruction. *J. Struct. Biol.* **1993**, *110* (1), 39−54.

(81) Landis, W. J.; Hodgens, K. J.; Song, M. J.; Arena, J.; Kiyonaga, S.; Marko, M.; Owen, C.; McEwen, B. F. Mineralization of Collagen May Occur on Fibril Surfaces: Evidence from Conventional and High-Voltage Electron Microscopy and Three-Dimensional Imaging. *J. Struct. Biol.* **1996**, *117* (1), 24−35.

(82) McNally, E.; Nan, F.; Botton, G. a; Schwarcz, H. P. Scanning transmission electron microscopic tomography of cortical bone using Z-contrast imaging. *Micron* **2013**, *49*, 46−53.

(83) Grandfield, K.; Palmquist, A.; Engqvist, H. Three-dimensional structure of laser-modified Ti6Al4V and bone interface revealed with STEM tomography. *Ultramicroscopy* **2013**, *127*, 48−52.

(84) Grandfield, K.; Engqvist, H. Characterization of dental interfaces with electron tomography. *Biointerphases* **2014**, *9* (2), 029001.

(85) Bals, S.; Goris, B.; Liz-Marzán, L. M.; Van Tendeloo, G. Three-Dimensional Characterization of Noble-Metal Nanoparticles and their Assemblies by Electron Tomography. *Angew. Chem., Int. Ed.* **2014**, *53* (40), 10600−10610.

(86) Wang, X.; Langelier, B.; Palmquist, A.; Grandfield, K. Biomineralization at Interfaces Revealed with 4D Electron and Atom Probe Tomographies. *Microsc. Microanal.* **2015**, *21* (S3), 83.

(87) Kelly, T. F.; Miller, M. K. Atom probe tomography. *Rev. Sci. Instrum.* **2007**, *78* (3), 031101.

(88) Narayan, K.; Prosa, T. J.; Fu, J.; Kelly, T. F.; Subramaniam, S. Chemical mapping of mammalian cells by atom probe tomography. *J. Struct. Biol.* **2012**, *178* (2), 98−107.

(89) Perea, D. E.; Liu, J.; Bartrand, J.; Dicken, Q.; Thevuthasan, S. T.; Browning, N. D.; Evans, J. E. Atom Probe Tomographic Mapping Directly Reveals the Atomic Distribution of Phosphorus in Resin Embedded Ferritin. *Sci. Rep.* **2016**, *6* (1), 22321.

(90) Gordon, L. M.; Joester, D. Nanoscale chemical tomography of buried organic-inorganic interfaces in the chiton tooth. *Nature* **2011**, *469* (7329), 194−197.

(91) Gordon, L. M.; Tran, L.; Joester, D. Atom Probe Tomography of Apatites and Bone-Type Mineralized Tissues. *ACS Nano* **2012**, *6* (12), 10667−1067 S.

(92) La Fontaine, A.; Zavgorodniy, A.; Liu, H.; Zheng, R.; Swain, M.; Cairney, J. Atomic-scale compositional mapping reveals Mg-rich amorphous calcium phosphate in human dental enamel. *Sci. Adv.* **2016**, *2* (9), e1601145−e1601145.

(93) Gordon, L. M.; Cohen, M. J.; MacRenaris, K. W.; Pasteris, J. D.; Seda, T.; Joester, D. Dental materials. Amorphous intergranular phases control the properties of rodent tooth enamel. *Science (Washington, DC, U. S.)* **2015**, *347* (6223), 746−750.

(94) Gordon, L. M.; Joester, D. Mapping residual organics and carbonate at grain boundaries and the amorphous interphase in mouse incisor enamel. *Front. Physiol.* **2015**, *6*, 57.

(95) Karlsson, J.; Sundell, G.; Thuvander, M.; Andersson, M. Atomically resolved tissue integration. *Nano Lett* **2014**, *14* (8), 4220−4223.

(96) Sundell, G.; Dahlin, C.; Andersson, M.; Thuvander, M. The bone−implant interface of dental implants in humans on the atomic scale. *Acta Biomater.* **2017**, *48*, 445−450.

(97) Ritchie, R. O.; Buehler, M. J.; Hansma, P. Plasticity and toughness in bone. *Phys. Today* **2009**, *62* (6), 41−47.

(98) Zimmermann, E. A.; Ritchie, R. O. Bone as a Structural Material. *Adv. Healthcare Mater.* **2015**, *4* (9), 1287−1304.

(99) Zimmermann, E. A.; Busse, B.; Ritchie, R. O. The fracture mechanics of human bone: influence of disease and treatment. *BoneKEy Rep.* **2015**, *4*, 743.

(100) Zimmermann, E. A.; Barth, H. D.; Ritchie, R. O. The Multiscale Origins of Fracture Resistance in Human Bone and Its Biological Degradation. *JOM* **2012**, *64* (4), 486−493.

(101) Tai, K.; Dao, M.; Suresh, S.; Palazoglu, A.; Ortiz, C. Nanoscale heterogeneity promotes energy dissipation in bone. *Nat. Mater.* **2007**, *6* (6), 454−462.

(102) Rodriguez-Florez, N.; Oyen, M. L.; Shefelbine, S. J. Insight into differences in nanoindentation properties of bone. *J. Mech. Behav. Biomed. Mater.* **2013**, *18*, 90−99.

(103) Depalle, B.; Qin, Z.; Shefelbine, S. J.; Buehler, M. J. Large Deformation Mechanisms, Plasticity, and Failure of an Individual Collagen Fibril With Different Mineral Content. *J. Bone Miner. Res.* **2016**, *31* (2), 380−390.

(104) Nair, A. K.; Gautieri, A.; Chang, S.-W.; Buehler, M. J. Molecular mechanics of mineralized collagen fibrils in bone. *Nat. Commun.* **2013**, *4*, 1724.

(105) Jalili, N.; Laxminarayana, K. A review of atomic force microscopy imaging systems: application to molecular metrology and biological sciences. *Mechatronics* **2004**, *14* (8), 907−945.

(106) Schwiedrzik, J.; Raghavan, R.; Bürki, A.; LeNader, V.; Wolfram, U.; Michler, J.; Zysset, P. In situ micropillar compression reveals superior strength and ductility but an absence of damage in lamellar bone. *Nat. Mater.* **2014**, *13* (7), 740−747.

(107) Tertuliano, O. A.; Greer, J. R. The nanocomposite nature of bone drives its strength and damage resistance. *Nat. Mater.* **2016**, *15*, 1195−1202.

(108) Chatzipanagis, K.; Baumann, C. G.; Sandri, M.; Sprio, S.; Tampieri, A.; Kröger, R. In situ mechanical and molecular investigations of collagen/apatite biomimetic composites combining Raman spectroscopy and stress-strain analysis. *Acta Biomater.* **2016**, *46* (C), 278−285.

(109) Hang, F.; Barber, A. H. Nano-mechanical properties of individual mineralized collagen fibrils from bone tissue. *J. R. Soc., Interface* **2011**, *8* (57), 500−505.

(110) Addadi, L.; Gal, A.; Faivre, D.; Scheffel, A.; Weiner, S. Control of Biogenic Nanocrystal Formation in Biomineralization. *Isr. J. Chem.* **2016**, *56* (4), 227−241.

(111) Wang, Y.; Azaïs, T.; Robin, M.; Vallée, A.; Catania, C.; Legriel, P.; Pehau-Arnaudet, G.; Babonneau, F.; Giraud-Guille, M.-M.; Nassif, N. The predominant role of collagen in the nucleation, growth, structure and orientation of bone apatite. *Nat. Mater.* **2012**, *11* (8), 724−733.

(112) Lausch, A. J.; Quan, B. D.; Miklas, J. W.; Sone, E. D. Extracellular Matrix Control of Collagen Mineralization In Vitro. *Adv. Funct. Mater.* **2013**, *23* (39), 4906−4912.

(113) Evans, J. S. Tuning in" to Mollusk Shell Nacre- and Prismatic-Associated Protein Terminal Sequences. Implications for Biomineralization and the Construction of High Performance Inorganic−Organic Composites. *Chem. Rev.* **2008**, *108* (11), 4455−4462.

(114) Bahn, S. Y.; Jo, B. H.; Hwang, B. H.; Choi, Y. S.; Cha, H. J. Role of Pif97 in Nacre Biomineralization: In Vitro Characterization of Recombinant Pif97 as a Framework Protein for the Association of Organic−Inorganic Layers in Nacre. *Cryst. Growth Des.* **2015**, *15* (8), 3666−3673.

(115) Nudelman, F.; Lausch, A. J.; Sommerdijk, N. A. J. M.; Sone, E. D. In vitro models of collagen biomineralization. *J. Struct. Biol.* **2013**, *183* (2), 258−269.

(116) Jiao, K.; Niu, L. N.; Ma, C. F.; Huang, X. Q.; Pei, D. D.; Luo, T.; Huang, Q.; Chen, J. H.; Tay, F. R. Complementarity and Uncertainty in Intrafibrillar Mineralization of Collagen. *Adv. Funct. Mater.* **2016**, *26* (38), 6858−6875.

(117) Lausch, A. J.; Quan, B. D.; Miklas, J. W.; Sone, E. D. Extracellular Matrix Control of Collagen Mineralization In Vitro. *Adv. Funct. Mater.* **2013**, *23* (39), 4906−4912.

L

(118) Verch, A.; Morrison, I. E. G.; van de Locht, R.; Kröger, R. In situ electron microscopy studies of calcium carbonate precipitation from aqueous solution with and without organic additives. *J. Struct. Biol.* 2013, *183* (2), 270−277.

(119) Smeets, P. J. M.; Cho, K. R.; Kempen, R. G. E.; Sommerdijk, N. A. J. M.; De Yoreo, J. J. Calcium carbonate nucleation driven by ion binding in a biomimetic matrix revealed by in situ electron microscopy. *Nat. Mater.* 2015, *14* (4), 394−399.

(120) De Yoreo, J. J.; Gilbert, P. U. P. A.; Sommerdijk, N. A. J. M.; Penn, R. L.; Whitelam, S.; Joester, D.; Zhang, H.; Rimer, J. D.; Navrotsky, A.; Banfield, J. F.; et al. Crystallization by particle attachment in synthetic, biogenic, and geologic environments. *Science (Washington, DC, U. S.)* 2015, *349* (6247), aaa6760−aaa6760.

(121) Nielsen, M. H.; Aloni, S.; De Yoreo, J. J. In situ TEM imaging of CaCO₃ nucleation reveals coexistence of direct and indirect pathways. *Science (Washington, DC, U. S.)* 2014, *345* (6201), 1158−1162.

(122) *Liquid Cell Electron Microscopy*; Ross, F. M., Ed.; Cambridge University Press: Cambridge, U.K., 2017.

(123) Klein, K. L.; Anderson, I. M.; De Jonge, N. Transmission electron microscopy with a liquid flow cell. *J. Microsc.* 2011, *242* (2), 117−123.

(124) Nielsen, M. H.; Yoreo, J. J. De. Liquid Cell TEM for Studying Environmental and Biological Mineral Systems. In *Liquid Cell Electron Microscopy*; Ross, F. M., Ed.; Cambridge University Press: Cambridge, U.K., 2017; pp 316−333.

(125) Liao, H.-G.; Zheng, H. Liquid Cell Transmission Electron Microscopy. *Annu. Rev. Phys. Chem.* 2016, *67* (1), 719−747.

(126) Ross, P. M. Opportunities and challenges in liquid cell electron microscopy. *Science* 2015, *350* (6267), aaa9886.

(127) Perovic, I.; Verch, A.; Chang, E. P.; Rao, A.; Cölfen, H.; Kröger, R.; Evans, J. S. An oligomeric C-RING nacre protein influences prenucleation events and organizes mineral nanoparticles. *Biochemistry* 2014, *53* (46), 7259−7268.

(128) Wang, X.; Yang, J.; Andrei, C.; Soleymani, L.; Grandfield, K. Biomineralization of Hydroxyapatite Revealed by in situ Electron Microscopy. *Microsc. Microanal.* 2016, *22* (S3), 746−747.

(129) Bloebaum, R. D.; Holmes, J. L.; Skedros, J. G. Mineral content changes in bone associated with damage induced by the electron beam. *Scanning* 2005, *27* (5), 240−248.

(130) Boskey, A. L.; Roy, R. Cell culture systems for studies of bone and tooth mineralization. *Chem. Rev.* 2008, *108* (11), 4716−4733.

(131) Boskey, A. L.; Stiner, D.; Doty, S. B.; Binderman, I.; Leboy, P. Studies of mineralization in tissue culture: optimal conditions for cartilage calcification. *Bone Miner.* 1992, *16* (1), 11−36.

(132) Hoemann, C. D.; El-Gabalawy, H.; McKee, M. D. In vitro osteogenesis assays: influence of the primary cell source on alkaline phosphatase activity and mineralization. *Pathol. Biol.* 2009, *57* (4), 318−323.

(133) Pujari-Palmer, M.; Pujari-Palmer, S.; Lu, X.; Lind, T.; Melhus, H.; Engstrand, T.; Karlsson Ott, M.; Engqvist, H. Pyrophosphate Stimulates Differentiation, Matrix Gene Expression and Alkaline Phosphatase Activity in Osteoblasts. *PLoS One* 2016, *11* (10), e0163530−13.

(134) Mathieu, V.; Vayron, R.; Richard, G.; Lambert, G.; Naili, S.; Meningaud, J.-P.; Haiat, G. Biomechanical determinants of the stability of dental implants: Influence of the bone−implant interface properties. *J. Biomech.* 2014, *47*, 3−13.

(135) Monsour, P.; Dudhia, R. Implant radiography and radiology. *Aust. Dent. J.* 2008, *53* (1), 11−25.

(136) Gupta, S.; Patil, N.; Solanki, J.; Singh, R.; Laller, S. Oral Implant Imaging: A Review. *Malays. J. Med. Sci.* 2015, *22* (3), 7−17.

(137) Korn, P.; Elschner, C.; Schulz, M. C.; Range, U.; Mai, R.; Scheler, U. MRI and dental implantology: Two which do not exclude each other. *Biomaterials* 2015, *53*, 634−645.

(138) De Vos, W.; Casselman, J.; Swennen, G. R. J. Cone-beam computerized tomography (CBCT) imaging of the oral and maxillofacial region: A systematic review of the literature. *Int. J. Oral Maxillofac. Surg.* 2009, *38* (6), 609−625.

(139) Benavides, E.; Rios, H. F.; Ganz, S. D.; An, C.-H.; Resnik, R.; Reardon, G. T.; Feldman, S. J.; Mah, J. K.; Hatcher, D.; Kim, M.-J.; et al. Use of Cone Beam Computed Tomography in Implant Dentistry. *Implant Dent.* 2012, *21* (2), 78−86.

(140) Donnelly, E. Methods for assessing bone quality: a review. *Clin. Orthop. Relat. Res.* 2011, *469* (8), 2128−2138.

(141) Schwarcz, H. P.; McNally, E. A.; Botton, G. A. Dark-field transmission electron microscopy of cortical bone reveals details of extrafibrillar crystals. *J. Struct. Biol.* 2014, *188* (3), 240−248.

M

9. Chapter 9: Appendix II

9.1 Human tissue preparation

9.1.1 Mineralized tissue

The full 5 mm thick section of bone was used for the mineralized bone sample. It was placed through the same dehydration, embedding and polishing procedures outlined below for demineralized tissue.

9.1.2 Demineralization procedure

Prior to demineralization, the 2 mm thick section of bone tissue was hand polished with 400, 800, 1200, and 2400 grit emery paper, and a 50 nm diamond suspension on a polishing cloth (Buehler, Illinois, US) to a thickness of approximately 200 µm, to ensure successful demineralization. The bone tissue was immersed in a demineralization solution of 5% ethylenediaminetetraacetic acid (EDTA) (Sigma Aldrich, Missouri, US), 2% paraformaldehyde (PFA) (Sigma Aldrich, Missouri, US) in cacodylate buffer, pH 7, and placed on a rocking table, until the bone became transparent. The demineralized bone tissue was then washed using Milli-Q water for 4 hours in duplicate, followed by a 12-hour water rinse to remove the residual EDTA. Demineralization of bone tissue allows for the removal of Ca/P crystals, and thus preserves the cellular network and collagen fibrils as the only components of the tissue.

9.1.3 Alcian blue staining and OTOTO staining

The demineralized bone was immersed in a saturated aqueous Alcian blue solution in a vial. The solution within the vial was then heated to 40°C using a hot plate for 10 minutes. The temperature was measured using a temperature probe. The vial was then left to cool to room temperature. This heating and cooling cycle was repeated 10 times to ensure the stain diffused into the sample. After staining, the tissue became dark blue in colour due to the stain infiltration.

The demineralized bone was immersed in a 1% OsO_4 solution in Milli-Q water for 1 hour to provide Z-contrast during staining. The sample was subsequently washed with Milli-Q water for 2 minutes, 5 times successively to ensure any unbound OsO_4 was removed (the first 'O' step in OTOTO staining). A saturated solution of 0.5% thiocarbohydrazide was prepared in Milli-Q water and filtered with a 0.25µm-Millipore filter equipped with a syringe. The demineralized bone sample was then immersed in this solution for 15 minutes and then washed with Milli-Q water for 2 minutes, 5 times successively (the first 'T' step). The sample was then immersed in the 1% OsO_4 solution in Milli-Q water for 15 minutes and then washed with Milli-Q water for 2 minutes, 5 times successively (the second 'O' step). These last two steps, the second O and first T staining were completed in a similar progression. The sample was then rinsed in Milli-Q water again. The final samples were no longer transparent but remained dark blue in colour due to the stain infiltration.

9.2 Dehydration and embedding

The demineralized sample was slowly dehydrated in a graded series of ethanol from 70% to 100% mixtures for 15 minutes each, followed by a 30-minute dehydration in 100% ethanol. The samples were immersed in 100% propylene oxide (Sigma Aldrich, Missouri, US). Due to the larger size of the mineralized sample, it was dehydrated the same series of ethanol for 24 hours at each concertation. The samples were placed in a mixture of Embed 812 resin (Thermoscientific, Massachusetts) at a 4:1 volume ratio for 12 hours and placed in a rotary mixer. The volume ratio was then decreased by one part (3:1, 2:1, and 1:1) for each successive infiltration, until the sample was in 100% Embed 812 for 12 hours. The sample was then placed into a small plastic mold in 100% Embed 812 and placed under vacuum using a vacuum oven set to room temperature for 12 hours. Once all bubbles were removed from the sample the sample was cured at 60°C for 48 hours.

9.3 Polishing

Both the top face and adjacent side of the samples were hand polished so that the bone was exposed from the embedding resin and a 90° angle was maintained between the two surfaces. The surfaces were hand polished using 1200 and 2400 grit emery paper, and a 50 nm diamond suspension on a polishing cloth (Buehler, Illinois, US). Only the two smallest grit sized emery

papers were used to ensure the sample was not completely polished away, and polish quality was checked frequently using a stereomicroscope (Lecia Microsystems, Ontario, Canada). In addition, it is important that the ROI is at the edge of the sample during PFIB milling. A high magnification stereomicroscope (Lecia, Ontario, Canada) was used to ensure the bone sample was at the edge of the resin during preparation.